

A Thesis Submitted for the Degree of PhD at the University of Warwick

Permanent WRAP URL:

<http://wrap.warwick.ac.uk/158725>

Copyright and reuse:

This thesis is made available online and is protected by original copyright.

Please scroll down to view the document itself.

Please refer to the repository record for this item for information to help you to cite it.

Our policy information is available from the repository home page.

For more information, please contact the WRAP Team at: wrap@warwick.ac.uk

Design and Synthesis of Responsive Nanoparticles for Targeted Drug Delivery

Robert Andrew Ennis Richardson

A thesis submitted in partial fulfilment of the requirements for the degree of

Doctor of Philosophy of Chemistry

Department of Chemistry

University of Warwick

December 2020

Table of Contents

1	Synthesis of Polymeric Nanoparticles.....	9
1.1	Introduction.....	9
1.1.1	Nanoparticles.....	9
1.1.2	Therapeutic Nanoparticles.....	9
1.1.3	Polymeric Nanoparticles for Drug Delivery.....	12
1.1.4	Polymeric Nanoparticle Synthesis.....	13
1.1.5	Reversible Deactivation Radical Polymerisation.....	17
1.1.6	RAFT Controlled Polymerisation.....	19
1.1.7	Overall Aims.....	28
1.2	References.....	30
2	The Effect Heterogeneous Conditions in Emulsion Polymerisation have on RAFT Agent Performance.....	36
2.1	Overview.....	36
2.2	Introduction.....	36
2.2.1	Emulsion Polymerisation.....	36
2.2.2	RAFT in Emulsion.....	37
2.2.3	RAFT Control in Emulsion Polymerisation.....	40
2.2.4	Transfer Surfactants.....	41
2.2.5	Objectives.....	42
2.3	Experimental.....	43
2.3.1	Materials.....	43
2.3.2	Analytical Techniques.....	43
2.3.3	Chemistry Techniques.....	45

2.4	Results and Discussion.....	48
2.4.1	Investigation of CTA-Acid as a Potential Transurf.....	48
2.4.2	Investigation of PEG-CTA as a Potential Transurf.....	51
2.4.3	Improved RAFT Control of Methacrylate Monomers.....	58
2.4.4	Chain Extensions.....	64
2.5	Conclusion.....	66
2.6	References.....	67
3	Synthesis and Characterisation of pH Responsive Nanoparticles	69
3.1	Overview	69
3.2	Introduction.....	69
3.2.1	Stimuli Responsive Nanoparticles	69
3.2.2	pH responsive Nanoparticles	75
3.2.3	Objectives.....	76
3.3	Experimental.....	76
3.3.1	Materials	76
3.3.2	Analytical Techniques	77
3.3.3	Synthetic Procedures.....	79
3.4	Results and Discussion.....	80
3.4.1	Responsive Particle Synthesis	80
3.4.2	Copolymerisation of Two pH Responsive Monomers	88
3.4.3	Copolymerisation of DPAEMA with BMA	89
3.4.4	Copolymerisation of DPAEMA with MMA.....	89
3.4.5	Effect of Polymer Chain Length on Particle Responsivness	90
3.4.6	Effect of Temperature on Particle Responsiveness	92

3.4.7	Effect of Salt Concentration on Particle Responsiveness.....	93
3.5	Conclusion.....	93
3.6	References	94
4	<i>In Vivo</i> applications of pH Responsive Nanoparticles	97
4.1	Overview	97
4.2	Introduction	97
4.2.1	Polymeric Nanoparticles for Drug Delivery.....	97
4.2.2	pH Responsive Polymeric Nanoparticles for Drug Delivery.....	98
4.2.3	Objectives.....	103
4.3	Experimental	103
4.3.1	Materials	103
4.3.2	Animals.....	104
4.3.3	Analytical Techniques	104
4.3.4	Biological Techniques	106
4.3.5	Synthetic Procedures.....	108
4.4	Results and Discussion.....	109
4.4.1	Design and Synthesis of Nanoparticles.....	109
4.4.2	<i>In vitro</i> cell toxicity assay	111
4.4.3	Cell Uptake Study	113
4.4.4	Drug loading and Purification.....	114
4.4.5	In vivo Results	120
4.5	Conclusion.....	135
4.6	References	136
5	Conclusion and Outlook	138

Acknowledgements

First, I would like to thank my supervisor Prof Sébastien Perrier who guided me throughout both my MChem and PhD projects. I would also like to thank the Perrier team as a whole, both past and present, for being such a wonderful group. I would especially like to thank all those I worked closely with, Dr Pratik Gurnani, Dr Andy Lunn, Hannah Burnage, Zihe Zhang (Taki), Vito Kontrimas, and Manpreet Kaur. Furthermore I would like to thank all of the talented people I have collaborated with both within chemistry; Prof Per Zetterlund, Dr Graeme Moad, Prof Peter Sadler, Dr Thiago Guimarães, Dr Murtaza Khan, Dr Russel Needham and Dr Tim Smith, and biology; Prof Robert Dallmann, Prof Francis Lev and Dr Swati Kumar. I would also like to thank my companion Sean for his constant support and insight. Finally, I would like to thank the funding bodies who contributed towards my PhD; the Engineering Physical Sciences Research Council (EPSRC) and Lubrizol. As well as additional funding from the RSC, SCI, SEP and CRUK.

Declaration

This thesis is submitted to the University of Warwick in support of my application for the degree of Doctor of Philosophy. It has been composed by myself and has not been submitted in any previous application for any degree. The work presented (including data generated and data analysis) was carried out by the author except in the cases outlined below:

Chapter 4: Work pertaining to animal handling and operations was performed by Dr Swati Kumar

Chapter 4: ICP measurements of osmium concentration in mice organs was measured in part by Dr Russel Needham

Parts of this thesis have been published by the author as:

Low-Dispersity Polymers in *Ab Initio* Emulsion Polymerization: Improved MacroRAFT Agent Performance in Heterogeneous Media – R. A. E. Richardson, T. R. Guimares, M. Khan, G. Moad, P. Zetterlund, S. Perrier
Macromolecules 2020

Abstract

Cancer is the second leading cause of death globally. Although many small molecule anti-cancer drugs have been developed, they suffer from several shortcomings. Most visibly, the poor targeting of small molecule drugs can cause side effects such as hair and muscle loss, and damage to the stomach lining. Small molecule drugs are also exposed to metabolic and clearance pathways, reducing overall efficiencies and requiring an even larger dose of these effectively toxic drugs to be administered. Small molecule drugs must also be soluble in the aqueous environment of the body; precluding the use of very hydrophobic molecules.

A promising solution to these problems is to encapsulate small molecule drugs within a polymeric nanoparticle delivery vehicle. The polymer shell can help solubilise the drug, shield it from metabolic damage and enable transport to the tumour. However, it is vital to release the drug on demand from the particle and avoid any potentially toxic accumulation of the particles once delivery is complete.

This thesis aims to investigate the synthesis of responsive polymeric nanoparticles and their potential applications to drug delivery systems. These nanoparticles are comprised of low dispersity polymers, expected to have similar biological properties, prepared by Reversible Addition Fragmentation chain Transfer (RAFT) polymerisation. While RAFT and emulsion polymerisation have been successfully combined to produce nanoparticles in the past, it has proven difficult to produce both low dispersity polymers and particles. Herein the effect emulsion polymerisation setup has on RAFT controlled is extensively explored. It is shown that RAFT control over the polymerisation of acrylates and methacrylates is improved substantially by emulsion polymerisation. The origin of this control is investigated and shown to be a consequence of the in-built monomer feeding mechanism existent within emulsion polymerisation. The improvement in RAFT control is utilised to produce multiblock copolymer particles.

In order for the nanoparticles to disassemble selectively at the pH within cells, it is necessary to investigate what factors affect the pH of disassembly. To this end, a library of fifteen responsive nanoparticles are presented and their pH of disassembly extensively investigated. The effect a number of design parameters have are assessed including; the concentration and chemical composition of the responsive monomer used, the hydrophobicity of the comonomer and overall polymer length. The pH of disassembly is also shown to be relatively independent of solution temperature and salt concentrations; ideal for use in biological applications. Five of the nanoparticles are shown to disassemble at intracellular pH values and their *in vitro* properties are documented. A non-toxic nanoparticle is then taken forward as a potential drug delivery vector. Loading of a potent anti-cancer drug into this nanoparticle is optimised before the *in vivo* properties are explored. Encapsulation of the drug within a nanoparticle is shown to improve the selectivity of uptake into tumour sites over healthy liver tissue significantly, concurrent with a reduction in animal fatalities.

Overall, this thesis demonstrates the synthesis of tuneable pH responsive nanoparticles and their successful applications as drug delivery vehicles.

1 Synthesis of Polymeric Nanoparticles

1.1 Introduction

1.1.1 Nanoparticles

Nanoparticles are defined as any particle with at least one diameter less than 1 micron (1000 nanometres). Their small size confers a number of interesting properties not accessible in bulk such as; very high surface area to volume ratios¹, changes to electrical², thermal³ and optical properties⁴, as well as changes in their biological behaviour⁵. These changes to bulk properties have led experimentalist to produce nanoparticles from an extraordinarily diverse range of materials; broadly divided into inorganic and organic nanoparticles. Inorganic nanoparticles have been made from; precious metals (gold⁶, silver⁷ and platinum⁸), metal oxides (titania⁹, magnetite¹⁰ and cerium oxide¹¹) and metalloids (silica¹² and germanium¹³). Organic nanoparticles have been made from both biological materials such as, liposomes¹⁴ and virus-like particles (VLPs)¹⁵, as well synthetic materials such as polymers¹⁶. Polymeric nanoparticles are a diverse group of organic nanoparticles comprised of either natural or synthetic polymers. They can be broadly divided further into two classes; cross-linked and self-assembled. The linking within cross-linked nanoparticles can be random, such as in hyper-branched nanoparticles¹⁷ and nanogels¹⁸, or can be finely controlled such dendrimer nanoparticles¹⁹. Self-assembled nanoparticles, such a polymersomes²⁰, do not feature covalent cross-linking points and their structure is instead maintained by entanglement and hydrophobic forces between polymer chains.

1.1.2 Therapeutic Nanoparticles

1.1.2.1 Therapeutic Inorganic Nanoparticles

Nanoparticles have been studied for their therapeutic uses since Antiquity, with the Chinese first using colloidal gold nanoparticles for treatment of a

range of internal maladies²¹. Gold nanoparticles are still prominent within the field and are often used for therapeutic diagnostic applications²². These diagnostic applications take advantage of golds surface plasmon resonance²³. This phenomenon, caused by the interaction of light with surface electrons, results in gold nanoparticles being strongly coloured in solution. Importantly, the colour is strongly dependent on the nanoparticles overall size; ranging from red for 30 nm diameter through to blue/purple for 70 nm particles²³. This shift in colour is routinely exploited to indicate binding of biomolecules to ligand decorated gold nanoparticles. Gold is not the only inorganic nanoparticle; silver, silica and iron oxide are all also being researched. Iron oxide nanoparticles of the form Fe_3O_4 in particular are being utilized for their superparamagnetic properties in the upcoming field of magnetic particle imaging (MPI)²⁴. This quantitative technique uses distortions in an applied magnetic field not only to detect injected iron oxide nanoparticles, but also inform on their local environment. Whilst useful in diagnostic applications, the intrinsically solid nature of inorganic nanoparticles, can retard clearance from the body and lead to potentially hazardous accumulation, particularly in the liver, over time²⁵.

1.1.2.2 Therapeutic Organic Nanoparticles

Organic nanoparticles cover a wide range of compositions but are often formed from smaller self-assembled units. Of these self-assemblies is the liposome, are one of the most widely investigated²⁶. Mimics of cell membranes²⁷, liposomes are comprised of amphiphilic phospholipids. These phospholipids self-assemble into vesicle structures on the broad size range of 25 – 2500 nm²⁸. First described in the 1965 by Bangham *et al.*²⁹, liposomes quickly became popular as potential drug delivery vectors. Encapsulation of both lipo and hydrophilic drugs is achievable within the vesicle wall or cavity respectively³⁰. Additionally, liposomes are generally considered non-toxic and non-immunogenic due to the use of natural phospholipids in their synthesis³¹.

Whilst versatile, poor structural stability³² means that liposomes are easily ruptured during injection and circulation; limiting their potential applications.

A second class of self-assembled organic nanoparticles are virus-like particles (VLPs)³³. VLPs are formed from the assembled capsid proteins of natural or synthetically altered viruses. Crucially, VLPs lack the internal genetic material found within actual viruses and are therefore non-infectious³⁴. Whilst non-infectious and non-toxic, VLPs can still trigger an unfavourable immune response *in vivo*, especially if impurities have not been rigorously expunged³⁵; however, PEGylation has been shown to reduce this greatly³⁶. As with liposomes, VLPs, can be produced in a range of sizes from 20 – 800 nm; however, due to their complex structure, it is very difficult to tailor VLPs to specific sizes³⁷. However, VLPs do, have an advantage over liposomes in that they are structurally far more stable and resistant to rupturing³⁸, additionally non-spherical morphologies are also possible³⁹. Overall though, difficulties with size control and immunogenicity, limit the potential applications of VLPs.

A third type of organic nanoparticles are the polymersomes; related to liposomes these vesicle structures are produced from the self-assembly of amphiphilic di and triblock copolymers⁴⁰. Importantly, the use of higher molecular weight hydrophobic polymers gives rise to more structurally resilient vesicles than is possible for liposomes⁴¹. The thickness of the polymersomes wall can also be significantly higher than for liposomes⁴², allowing a larger volume for encapsulating lipophilic drugs without increasing particle size. An even larger encapsulation volume can be achieved by using amphiphilic diblock copolymers that assemble into micelle like structures rather than vesicles⁴³. These polymeric nanoparticles, termed core-shell, in particular are becoming the focus of drug delivery nanoparticles⁴⁴ and are discussed further in the next section.

1.1.3 Polymeric Nanoparticles for Drug Delivery

The synthesis of polymeric nanoparticles is extensively discussed in the thesis introduction (Section 1.1.4), in this section, the use of these nanoparticles as drug delivery vehicles will be reviewed. First, it is important to discuss why drug delivery vectors are desirable. Conventional small molecule drug delivery has several shortcomings, largest of which is the difficulties in designing drugs to specifically accumulate within the desired site of sickness⁴⁵. This lack of accumulation requires a larger dose of the drug to be administered in order to ensure enough reaches the desired site. Secondly, small molecule drugs are also exposed to the metabolic and clearance pathways of the body, reducing overall efficiencies and requiring an even larger dose size⁴⁶. These large dose sizes increase the risk of potential side effects. These problems of poor selectivity and large dose are exacerbated in cases of already toxic drug molecules such as chemotherapy agents⁴⁷. A final challenge facing small molecule drug delivery is poor solubility of the drug molecule in the aqueous environment of the body⁴⁸. It is therefore required that drug molecules be designed with high water solubility, sometimes to the detriment of their target binding ability⁴⁹. Encapsulation of hydrophobic drug molecules within a water-soluble polymeric nanoparticle is one attractive answer to this solubility problem⁵⁰. The benefits of encapsulation go even further than this, however; the polymer coating may act to shield sensitive drug molecules from early degradation within the body, for example⁵¹. Furthermore, polymeric nanoparticles decorated with specific ligands are gaining attention as a method for improving targeting to specific regions and cell types in the body (Table 1).

Ligand	Receptor	Nanoparticle	Outcome	References
RGD peptide	Integrin $\alpha_v\beta_3$	Polylysine-gelatine	1.18 fold increase in tumour accumulation	Gao ⁵²
Transferrin	Transferrin receptor	PEG-chitosan	6.7 times improved anti-cancer activity <i>in vitro</i>	Jain ⁵³
Hyaluronic acid	CD-44	PEG-HACE	Higher uptake and 30% increased anti-tumour growth	Kim ⁵⁴
Folic acid	Folate receptor	PEG-PLGA	26.7 times increased cell uptake	Mei ⁵⁵
Galactose	ASGPR	PEG-LPL	Increased cell uptake and anti-tumour activity	Cho ⁵⁶

Table 1: A table of literature examples of ligands used to decorated nanoparticles, their molecular targets and the study outcomes.

1.1.4 Polymeric Nanoparticle Synthesis

A range of synthesis routes to form polymeric nanoparticles have been designed. In this section, the four main techniques will be discussed beginning with the oldest, emulsion polymerisation (1909).

1.1.4.1 Emulsion Polymerisation

In emulsion polymerisation, a surfactant is used to stabilise droplets of hydrophobic monomer dispersed in an aqueous phase. Excess surfactant also

forms micelles in solution that swell with hydrophobic monomer. A water-soluble initiator is then added, which upon homolytic fission, reacts with the sparingly soluble amount of hydrophobic monomer present to give the beginnings of a growing polymer chain. At a specific length, the growing chains, termed Z-mers, become surface active and can enter into either the surfactant micelle or a monomer droplet. Whilst the size of a monomer droplet is typically far larger than a surfactant micelle, the total number of micelles far exceeds that of monomer droplets giving a larger overall surface area for entry to occur into, making this event statistically more likely. Upon entry, the monomer-swollen micelle provides a miniaturised reaction vessel for the chain propagation to continue. As the monomer in the micelle is consumed by the growing chain, more diffuses in from the aqueous phase. To replenish the loss of the monomer in the aqueous phase, monomer units from the large droplets diffuse out into the solution; effectively transferring monomer from the droplets to the micelles and keeping the concentration constant⁵⁷. In order for adequate diffusion of monomer, emulsion polymerisations is unsuitable for ultrahydrophobic monomers such as lauryl methacrylate under normal circumstances⁵⁸. Near high conversion, all the monomer in the droplet has been consumed and the concentration in the micelles finally begins to drop. At this point, the reaction begins to slow as the rate of termination outweighs that of propagation. After polymerisation, the final nanoparticle is kept stabilised in solution by two things; residual amounts of surfactant physisorbed onto the surface and the presence of charged polymer end groups coming from the initiator used. Over time, dilution and diffusion effects can strip the surfactant off the nanoparticle surface, leading to destabilisation and ultimately flocculation and aggregation.

1.1.4.2 Miniemulsion Polymerisation

Whilst emulsion polymerisation is limited to less hydrophobic monomers, miniemulsion polymerisation can be used to prepare nanoparticles containing

ultrahydrophobic monomers⁵⁹. In miniemulsion, a mixture of hydrophobic monomer and hydrophobic initiator are homogenised with a surfactant in water to form monomer droplets on the size range of 100 – 1000 nm⁶⁰. The reaction is then heated to begin initiator decomposition and start the polymerisation. Similarly to emulsion polymerisation, the compartmentalisation of radicals and high concentration of monomer within the droplet, allows for rapid chain growth⁶¹. Unlike emulsion polymerisation, however, there is no necessity for monomer to diffuse into the growing particle allowing for the use of ultrahydrophobic monomers such as lauryl methacrylate⁵⁹. As there is no replenishment of monomer in miniemulsion, the polymerisation kinetics should be viewed the same as a high concentration solution or bulk polymerisation⁶².

1.1.4.3 Dispersion

In dispersion polymerisation, a sparingly water-soluble monomer and initiator are used in aqueous conditions. Importantly it is required that while the starting monomer be soluble, the formed polymer be water-insoluble. As the monomer and initiator are present in the water from the start, the first phase of the polymerisation follows classical solution kinetics. However, once the growing polymer reaches a critical length, often denoted as j_{crit} , it becomes insoluble and precipitates from solution. These precipitated polymers aggregate together to form nanosized objects that then swell with more monomer. These swollen nanoobjects then act as compartmentalized reaction centres as was discussed for emulsion polymerisation (section 1.1.4.1) and the rate of polymerisation increases accordingly. As monomer is consumed within the growing particle, more diffuses in from the aqueous phase; resulting in a near constant concentration at the site of polymerisation and a linear evolution of conversion with time. At high conversion, when all the remaining monomer has been used, the rate of polymerisation decreases sharply and the polymerisation ends.

1.1.4.4 Nanoprecipitation

Polymeric nanoparticles do not have to be formed during polymerisation as seen in emulsion and miniemulsion polymerisation; an example of this is nanoprecipitation⁶³. Nanoprecipitation relies on the use of preformed, amphiphilic, diblock co-polymers. These diblocks are first solubilised in a water-miscible organic solvent such as, tetrahydrofuran, dioxane, dimethylformamide, or methanol⁶⁴. Once dissolved, the polymer solution is added to an excess of water; diluting the organic solvent used and triggering collapse of the polymer chains. Upon collapse, the hydrophobic sections of the diblock aggregate together, forming nanoparticles stabilised by the hydrophilic sections. The size and uniformity of the nanoparticles formed is strongly dependent on the aggregation step⁶⁵ and many parameters such as; polymer solution concentration, stirring speed, organic solvent used and temperature need to be optimised in order to produce uniform nanoparticles. A further disadvantage of nanoprecipitation is the inherent use of organic solvents, which require extensive purification, often by dialysis, to remove. Whilst challenging to optimise and purify, nanoprecipitation can, theoretically, use any two polymers in the diblock including the use of attractive natural polymers and their derivatives such as; polylactic acid⁶⁶, cellulose acetate⁶⁷ and pullulan acetate⁶⁸. The use of these naturally derived polymers is not typically possible with emulsion and miniemulsion polymerisations, which rely on free radical polymerisation.

1.1.4.5 Spray-drying

Spray-drying is a second example of nanoparticle formation after polymerisation⁶⁹. In spray-drying, the polymer of interest is dissolved in a volatile organic solvent, typically methanol⁷⁰. Next, this polymer solution is forced through an ultrafine nozzle, known as an atomizer, rapidly; producing micron-sized droplets of polymer solution in the gaseous phase. A flow of warm gas is passed over the polymer solution droplets triggering rapid

evaporation of the organic solvent and formation of the solid nanoparticle. The final size of the nanoparticle formed is controlled by a number of factors⁷¹, primarily the nature of the organic solvent used; requiring it to be both highly volatile and have a low density in order to produce nano-sized particles⁷⁰. Whilst size control can be challenging, the overall process is highly scalable and already routinely used within the pharmaceutical industry^{72, 73}.

1.1.5 Reversible Deactivation Radical Polymerisation

Reversible Deactivation Radical Polymerisations (RDRPs) are a group of free radical polymerisations in which an additive is added to improve control over the final polymer⁷⁴. The main advantages of RDRP over free radical polymerisation are that the final polymer dispersity is low ($\mathcal{D} \sim 1.1 - 1.2$)⁷⁵ and that the overall molecular weight can be easily predicted and tailored. Additionally, use of RDRP, allows for control and functionalisation of both chain ends⁷⁶. The control in RDRP is derived from an equilibrium between active growing chains and dormant ones. By reversibly deactivating the polymer chain ends, the overall number of radicals in the system at a given time is minimized. Decreasing the overall number of radicals affects both the rates of propagation and termination as described by the simplified equations below.

$$\text{Rate of Propagation} = k_p[\text{Mon}][R^*] \quad (1)$$

$$\text{Rate of Termination} = k_t[R^*]^2 \quad (2)$$

Where k_p and k_t are the rate constants of propagation and termination respectively and $[\text{Mon}]$ and $[R^*]$ are the concentrations of monomer and radicals within the system. Whilst reducing the radical concentration $[R^*]$, leads to an unfavourable linear decrease in the rate of propagation (1), it causes a polynomial decrease in the rate of termination (2). This therefore results in a slower polymerisation overall but one that is less prone to termination events.

The three most prominent examples of RDRP are Atom Transfer Radical Polymerisation (ATRP)⁷⁷, Nitroxide-Mediated Polymerisation (NMP)⁷⁸ and Reversible Addition-Fragmentation chain Transfer (RAFT)⁷⁹. In ATRP a transition metal catalyst, usually copper or iron, is used to reversibly abstract a halogen (chloride, bromide and iodide) or pseudo-halogen (thiol and isothiocyanate) from a polymer chain end; forming a propagating radical⁷⁹. By reversibly activating and deactivating this propagating radical, ATRP keeps the overall concentration of radicals low, reducing the rate of termination with respect to propagation. Along a similar vein, polymer control within NMP is the result of the reversible deactivation of growing polymer chains by reaction with so-called stable nitroxide radicals (Figure 1).

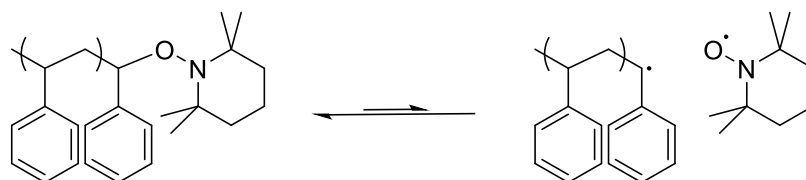


Figure 1: The reversible activation of growing polymer chains by NMP

Whilst the nitroxide radical formed is low energy, the propagating radical is not, disfavours the activation of chains. NMP can therefore only be successfully performed on more stable monomer classes such as styrenes and methacrylates⁷⁸.

In NMP and ATRP the growing polymer chains are reversibly deactivated by a separate radical mediator. In contrast to this, RAFT control depends on the reversible chain transfer of radicals from one chain to another, thus the number of growing polymer chains remains constant. As the RAFT end group remains attached to the polymer, it is more amenable to heterogeneous conditions, such as those used to prepare nanoparticles, and is discussed further in the next section.

1.1.6 RAFT Controlled Polymerisation

First reported in 1998 by Moad, Rizzardo, Thang and co-workers⁸⁰, RAFT allows for the formation of low dispersity polymers from a range of monomers⁸¹⁻⁸³, the synthesis of diblocks and multiblocks⁸⁴ and complex polymeric architectures; such as bottle brushes and stars^{85, 86}, and is compatible with a number of functional groups⁸⁷⁻⁸⁹. Control is achieved by reversible deactivation of growing chains Figure 2.

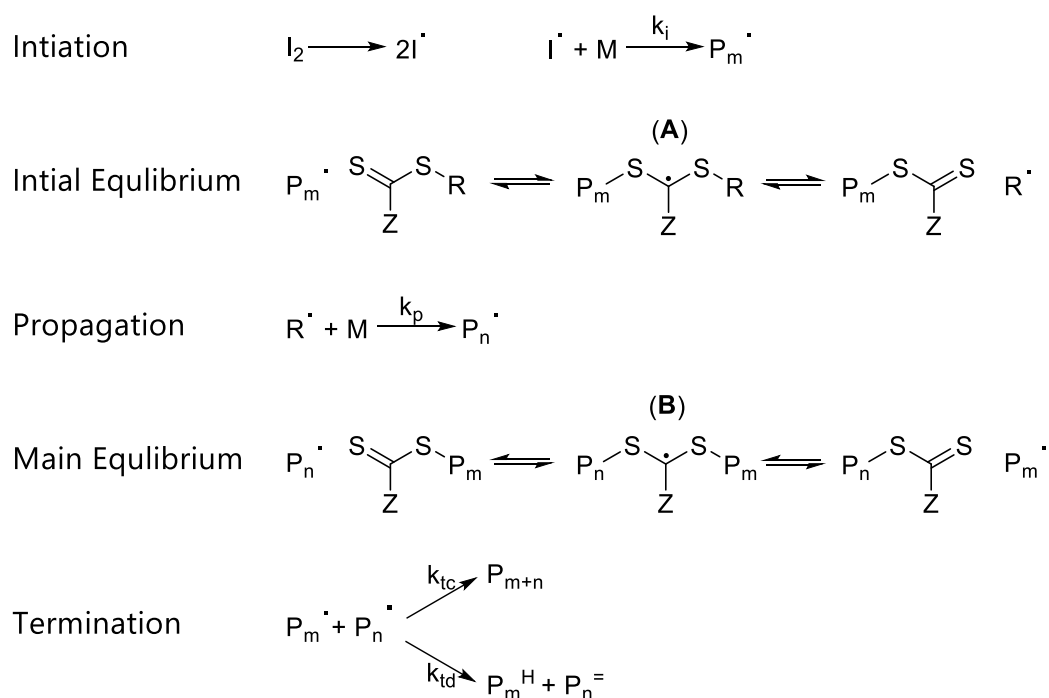


Figure 2: The chemical mechanism of RAFT mediated polymerisation.

The first stage of the RAFT mechanism is generation of an initiator radical, this is commonly done by addition of a thermolytic initiator; however, UV⁹⁰ and redox conditions⁹¹ can both also be used. The initiator radical then polymerises a number of monomer units to generate a propagating radical (P_m^\cdot). This propagating radical next adds to the π^* orbital of the C=S bond in the RAFT agent; weakening it and leading to the formation of the intermediate A shown. This intermediate can then fragment further to release a reinitiating radical (R^\cdot) and generate a new C=S bond. Both the addition of P_m^\cdot and the fragmentation of R^\cdot are equilibrium reactions. To drive the equilibrium forward, R^\cdot must be at

least as stable as $P_m\cdot$, if it is not then the equilibrium will continually favour the starting products; reducing RAFT incorporation and overall polymer control⁹².

Once generated, the reinitiating radical can react with more monomer to produce a second propagating radical ($P_n\cdot$). If $R\cdot$ is well-stabilised then intermediate A will rapidly fragment to form it, however, the rate of monomer addition to it to form $P_n\cdot$ will be retarded⁹³. The selection of an appropriate R-group is therefore pivotal to achieving good RAFT control; in practice, an R-group similar in structure to the monomer is often chosen⁹⁴. Once formed, $P_n\cdot$ can then react with another starting RAFT agent or with one already attached to a polymer chain end, the latter being termed the main equilibrium. The cycle continues of reversibly generating, propagating and deactivating propagating radicals until all the available monomer has been consumed. At all stages of the polymerisation, termination events will be occurring; however, their frequency is reduced by minimizing the overall radical concentration at any given time.

A plethora of RAFT agents exist with varying R and Z groups, whilst the importance of the R group has already been discussed, the Z-groups impact may be less apparent. RAFT agents have been synthesised with a range of Z-groups, the four most common being; trithiocarbonates ($Z = SR$)⁹⁵, dithiobenzoates ($Z = Ph$)⁹⁶, xanthates ($Z = OR$)⁹⁷ and dithiocarbamates ($Z = NR_2$)⁹⁸ (Figure 3).

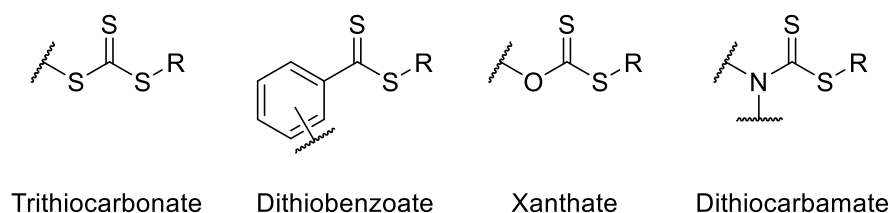


Figure 3: Chemical structures of trithiocarbonates, dithiobenzoates, xanthates and dithiocarbamates.

As well as these four classes of RAFT agents, many others have been produced with Z-groups as exotic as; cyano (CN)⁹⁹, fluoro (F)¹⁰⁰, phosphinoyl (R₂P=O)¹⁰¹ and aryl stanine (Ph₃Sn)¹⁰². The Z-group effects the stability of both the ground state RAFT agent and the radical intermediates A and B (Figure 2). A lone pair on the first atom of the Z-group can provide resonance stabilisation to the ground state of the RAFT agent (Figure 4).

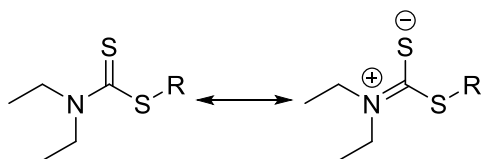


Figure 4: The resonance structure of a dithiocarbamate

This resonance stabilisation increases with the accessibility of the lone pair following the general order N>O>P>S, however, competing involvement in π -systems may alter this. The dithiocarbamates shown in Figure 5 exhibit markedly different RAFT properties due to changes in the nitrogen lone pair accessibility¹⁰³.

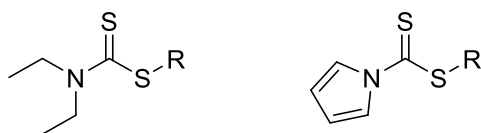


Figure 5: The structures of N-diethyl and pyrrole derived dithiocarbamate

Neighbouring π -systems in the Z-group, such as for dithiobenzoates, can also stabilise the RAFT ground state. This stabilisation is a result of conjugation between the π -systems and the C=S bond. The stabilisation provided, however, is less than for lone pairs discussed above; being +40 kJ/mol for an unsubstituted phenyl substituent compared to +60 kJ/mol for an aliphatic sulphur, relative to a hydrogen Z-group⁹³. Whilst adjacent lone pairs and π -systems stabilize the RAFT ground state, strong σ -withdrawing groups such as; cyano (CN), fluoro (F) and trifluoro (CF₃), destabilise it by polarising the C=S bond¹⁰⁰.

As well as the RAFT ground state, the Z-group has a large effect on the stability of the intermediate radicals formed (Figure 2). Adjacent lone pairs on the Z-group stabilise the intermediates by donating to the partly filled P-orbital in which the radical resides (Figure 6).

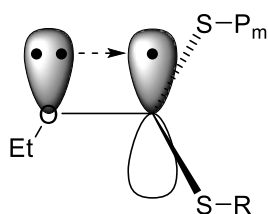


Figure 6: A graphic depicting donation of an oxygen lone pair to the radical centre of a xanthate intermediate.

Donation from the lone pair to the radical forms a new fully filled bonding orbital and a half filled antibonding orbital, reducing the overall energy of the intermediate but increasing the radicals energy state. As well as the Z-group, the radical intermediate is also stabilised by the lone pairs on both adjacent sulphurs; raising the radicals energy considerably. The increase in radical energy pushes it beyond the point where a third sulphur atom lone pair can donate. However, the higher energy lone pairs on oxygen and nitrogen are still able to donate and reduce the intermediates energy further. Lone pair stabilisation from the Z-group is therefore only possible for xanthates ($Z = O$) and dithiocarbamates ($Z = N$). As well as lone pairs, neighbouring π -systems in the Z-group, such as in dithiobenzoates, can reduce the intermediates energy considerably. This decrease is as a result of electron donation from the π -systems towards the radical and resonance delocalisation of it (Figure 7).

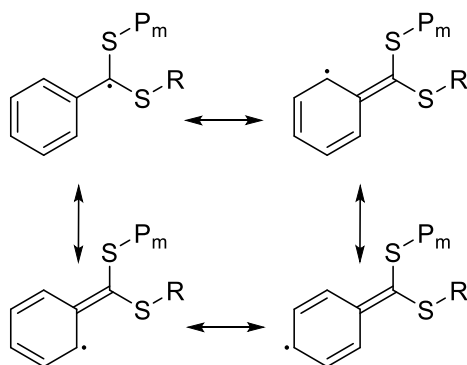


Figure 7: The resonance structures of intermediate radical delocalisation for dithiobenzoates

Strong intermediate stabilisation such as that seen in dithiobenzoates, reduces the rate at which the intermediates A and B fragment to release the reinitiating or propagating radical. This delay leads to a retardation in the rate of polymerisation and is also postulated to cause cross coupling side reactions between the phenyl substituents^{104, 105}. Whilst adjacent lone pairs and π -systems stabilize the intermediate radical via electron donation, strongly σ -withdrawing groups such as cyano, nitro and trifluoro as well as atoms such as fluorine and oxygen, destabilise it. However, these σ -withdrawing groups may also be stabilising the intermediate by other means, such as the π -system in the cyano group and the lone pair on neighbouring oxygen groups; reducing their overall effect. Combinations of the above effects, results in a mismatch between the order of ground state and intermediate energies for trithiocarbonates (TTC), xanthates (Xan), dithiobenzoates (DTB) and dithiocarbamates (DTC) (Figure 8).

stabilised (MAMs) and those in which it is less (LAMs). Examples of MAMs including styrenes, methacrylates, acrylates and acrylamides whilst examples of LAMs include vinyl ethers, vinyl acetates and dienes. The affect different energy levels have on RAFT control is best highlighted by xanthates and trithiocarbonates, for these two classes of monomers. The xanthate ground state energy is considerably lower than the trithiocarbonate (Figure 8). This low energy ground state reduces the reactivity of xanthates towards already stabilised propagating radicals such as those produced by MAMs and retards addition. Conversely, the higher energy ground state of trithiocarbonate allows it to add both MAM and LAM based propagating radicals efficiently. However, the higher energy ground state reduces the rate of fragmentation, especially for the less stable LAM based propagating radicals. This reduced rate of fragmentation, increases the intermediates presence; leading to side reactions such as those seen for dithiobenzoates¹⁰⁵. Conversely, return to the significantly lower ground state of xanthates, drives intermediate fragmentation forward, even for LAMs. Due to their varying rates of addition and fragmentation, trithiocarbonates are best coupled with MAMs whilst xanthates are suitable for LAMs¹⁰⁶.

Since its inception, RAFT has been used to produce polymeric nanoparticles by a number of different routes; the main three are described in the following subsections.

1.1.6.1 RAFT Diblock Nanoprecipitation

The reversible deactivation of polymers by the RAFT mechanism allows for the facile synthesis of diblock copolymers¹⁰⁷. As described, *vide supra* (Section 1.1.4.4), amphiphilic diblock copolymers can be precipitated into water to produce uniform nanoparticles. This method was utilised by Bernard *et al.*¹⁰⁸ to generate core-shell nanoparticles with an exterior of hydroxypropyl

methacrylamide (HPMAm) and an interior of *N*-dimethyl aminoethyl methacrylate (DMAEMA), structures below (Figure 9).

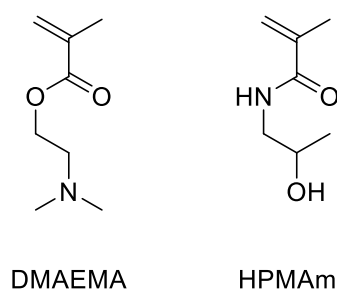


Figure 9: The chemical structures of DMAEMA and HPMAm

Diblock co-polymers of HPMA and DMAEMA prepared by RAFT solution polymerisation, were dissolved in acetone before being added dropwise to rapidly stirring water. The nanoparticles formed as the water insoluble DMAEMA block precipitated out of solution. Depending on the targeted application, the residual organic solvent needs to be removed, often by laborious extensive dialysis, as was the case for Bernard *et al.*¹⁰⁸ above.

1.1.6.2 Aqueous RAFT Dispersion

To remove the necessity of organic solvents, an alternative to RAFT diblock nanoprecipitation, is to perform a RAFT mediated dispersion polymerisation¹⁰⁹. In a typical synthesis, a hydrophilic monomer is first polymerised in water to form short stabilisers¹¹⁰. These stabilisers are then further chain extended with a second, sparingly water-soluble, monomer. Above a certain chain length, often denoted as J_{crit} , this second block becomes insoluble in water and precipitates to form nano-objects stabilised by the fully soluble first block. Once precipitated, the polymerisation takes on a similar mechanism to a standard emulsion polymerisation described in section 1.1.4.1. Unlike a typical emulsion polymerisation, however, the final products formed are not necessarily spherical. Different morphologies including; spheres, worms and vesicles, have been prepared and this tendency towards non-spherical objects

has given rise to the expansive field of Polymerisation Induced Self Assembly (PISA)¹¹¹; examples below.

Table 2: A table of PISA experiments taken from the literature highlighting the different morphologies possible.

Monomer		Morphology	Author <i>et al.</i>
Hydrophilic	Hydrophobic		
AA₁₅[*] / PEGA₁₅	BzMA ₉₀	Spheres + Worms	Charleux ¹¹²
GMA₄₇	HPMA ₁₁₃	Worm	Armes ¹¹³
PEG₁₁₃	HPMA ₄₀₀	Vesicle	O'Reily ¹¹⁴
MAA₇₉	(Sty- <i>a/t</i> -NMI) ₆₅₀	Lamella	Armes ¹¹⁵
P4VP₁₀₀^{**}	Sty ₁₀₀₀	Multiwall Vesicle	Pan ¹¹⁶

AA = acrylic acid, PEGA = polyethylene glycol acrylate, BzMA = bezyl methacrylate, GMA = glycerol methacrylate, HPMA = 2-hydroxypropyl methacrylate, PEG = polyethylene glycol, MAA = methacrylic acid, Sty = styrene, NMI = N-phenylmaleimide, P4VP, poly(4-vinyl pyridine). * Used under basic conditions (pH 10). ** Used under acid conditions (pH 4).

The morphology formed by PISA is dependent upon the diblock polymer concentration as well as the balance between the hydrophilic and hydrophobic portions. This balance is best expressed as a critical packing parameter (CPP) derived from the equation below where V and l_c are the volume and length of the hydrophobic block and a_0 is the surface area the hydrophilic portion.

$$CPP = \frac{V}{a_0 l_c} \quad (3)$$

A critical packing parameter of less than $1/3$ results in the formation of spherical nanoparticles. Increasing the CPP to between $1/3$ and $1/2$ leads to the formation of worm-like structures while increasing the CPP further up to near 1 results in vesicle structures. Lamella sheets can be formed when the packing parameter is close to 1. For a fixed length hydrophilic block, the value of CPP increases with hydrophobic block size; allowing for the formation of multiple morphologies from the same starting block. This was elegantly demonstrated by Armes, Hatton and co-workers who used *in situ* small angle x-ray scattering

(SAXS) to monitor the evolution of morphology with increasing conversion and concomitant hydrophobic block length extension¹¹⁷. As the nanoobjects in PISA are assembled *in situ*, high solids content of above 20% are achievable¹¹⁸; making RAFT dispersion an attractive method for scaling up nanoparticle synthesis. Despite its potential for scale-up though, the inherent requirement of the second monomer to be sparingly soluble in water, does limit the range of monomers available. As well as this, a lack of control during the precipitation stage of polymerisation makes it challenging to achieve uniformly sized nanoobjects; in the worst case, mixtures of different morphologies may even be obtained¹¹².

1.1.6.3 RAFT Emulsion

RAFT emulsion polymerisation follows a similar setup to free radical emulsion polymerisation described in section 1.1.4.1. Importantly, however, the normal molecular surfactant is replaced by a preformed amphiphilic diblock prepared by RAFT¹¹⁹. This diblock, commonly termed the macro-RAFT agent, acts to both stabilise the growing particles and control the constituent polymer growth¹²⁰. As the polymer chains are extended from the diblock, the stabiliser element remains covalently attached to the nanoparticle at the end of the reaction; removing the risk of surfactant desorption seen for ordinary emulsion polymerisation. Further, as the starting diblock was located at the growing particle interface, its hydrophilic portion remains on the outside of the particle; allowing the surface to be coated in specific moieties such as sugars¹²¹ or alkynes for further reactions¹²².

1.1.7 Overall Aims

This aims of this project are to synthesis polymeric nanoparticles for improved anticancer drug delivery. As these nanoparticles will be used in the body, it is important that the biological behaviour of their component polymers is predictable and well understood. To this end, Controlled Radical

Polymerisation (CRP) will be used to produce low dispersity polymers of a consistent molecular weight and similar properties *in vivo*. As discussed extensively in section 1.1.4, these polymers can be prepared prior or during nanoparticle formation. Methods for nanoparticle synthesis after polymerisation include nanoprecipitation (1.1.4.4) and spray-drying (1.1.4.5); however, both these methods necessitate the use of potentially toxic organic solvents. In contrast, polymerisation during formation by either emulsion (1.1.4.1) or dispersion (1.1.4.3) presents an aqueous only route to nanoparticles. As reviewed earlier, while dispersion polymerisation can form nanoparticles at attractively high weight concentrations, the morphology of these nanoparticles can be difficult to fully control. Emulsion polymerisation, by contrast, can be used to produce spherical nanoparticles with a narrow distribution of sizes. The heterogeneous conditions of emulsion polymerisation can prove challenging to CRP techniques in which the polymerisation is controlled by an entirely separate radical mediator such as ATRP and NMP. As discussed in section 1.1.6.3, RAFT polymerisation is well suited to emulsion and it will be used to prepare nanoparticles throughout this thesis. In the next chapter, various existing styles of RAFT emulsion are reviewed and compared before the effect of emulsion conditions have on RAFT control is more extensively explored.

1.2 References

1. R. M. Rioux, H. Song, J. D. Hoefelmeyer, P. Yang and G. A. Somorjai, *The Journal of Physical Chemistry B*, 2005, **109**, 2192-2202.
2. S. E. F. Kleijn, S. C. S. Lai, M. T. M. Koper and P. R. Unwin, *Angewandte Chemie International Edition*, 2014, **53**, 3558-3586.
3. H. Jiang, K.-s. Moon, H. Dong, F. Hua and C. P. Wong, *Chemical Physics Letters*, 2006, **429**, 492-496.
4. K. L. Kelly, E. Coronado, L. L. Zhao and G. C. Schatz, *The Journal of Physical Chemistry B*, 2003, **107**, 668-677.
5. C. Buzea, I. I. Pacheco and K. Robbie, *Biointerphases*, 2007, **2**, MR17-MR71.
6. P. Zhao, N. Li and D. Astruc, *Coordination Chemistry Reviews*, 2013, **257**, 638-665.
7. M. Ahamed, M. S. AlSalhi and M. K. J. Siddiqui, *Clinica Chimica Acta*, 2010, **411**, 1841-1848.
8. G. J. Leong, M. C. Schulze, M. B. Strand, D. Maloney, S. L. Frisco, H. N. Dinh, B. Pivovar and R. M. Richards, *Applied Organometallic Chemistry*, 2014, **28**, 1-17.
9. A. Weir, P. Westerhoff, L. Fabricius, K. Hristovski and N. von Goetz, *Environmental Science & Technology*, 2012, **46**, 2242-2250.
10. L. A. Harris, J. D. Goff, A. Y. Carmichael, J. S. Riffle, J. J. Harburn, T. G. St. Pierre and M. Saunders, *Chemistry of Materials*, 2003, **15**, 1367-1377.
11. F. Zhang, S.-W. Chan, J. E. Spanier, E. Apak, Q. Jin, R. D. Robinson and I. P. Herman, *Applied Physics Letters*, 2002, **80**, 127-129.
12. S.-H. Wu, C.-Y. Mou and H.-P. Lin, *Chemical Society Reviews*, 2013, **42**, 3862-3875.
13. L. Pizzagalli, G. Galli, J. E. Klepeis and F. Gygi, *Physical Review B*, 2001, **63**, 165324.
14. Y. P. Patil and S. Jadhav, *Chemistry and Physics of Lipids*, 2014, **177**, 8-18.
15. B. Chackerian, *Expert Review of Vaccines*, 2007, **6**, 381-390.
16. X. Wang, J. E. Hall, S. Warren, J. Krom, J. M. Magistrelli, M. Rackaitis and G. G. A. Bohm, *Macromolecules*, 2007, **40**, 499-508.
17. C. Aymonier, U. Schlotterbeck, L. Antonietti, P. Zacharias, R. Thomann, J. C. Tiller and S. Mecking, *Chemical Communications*, 2002, DOI: 10.1039/B208575E, 3018-3019.
18. S. Vinogradov, E. Batrakova and A. Kabanov, *Colloids and Surfaces B: Biointerfaces*, 1999, **16**, 291-304.
19. I. Gitsov and C. Lin, *Current Organic Chemistry*, 2005, **9**, 1025-1051.
20. D. E. Discher and F. Ahmed, *Annual Review of Biomedical Engineering*, 2006, **8**, 323-341.

21. S. Mahdihassan, *The American Journal of Chinese Medicine*, 1985, **13**, 93-108.
22. L. Yu and A. Andriola, *Talanta*, 2010, **82**, 869-875.
23. H. Aldewachi, T. Chalati, M. N. Woodroffe, N. Bricklebank, B. Sharrack and P. Gardiner, *Nanoscale*, 2018, **10**, 18-33.
24. E. Y. Yu, M. Bishop, B. Zheng, R. M. Ferguson, A. P. Khandhar, S. J. Kemp, K. M. Krishnan, P. W. Goodwill and S. M. Conolly, *Nano Letters*, 2017, **17**, 1648-1654.
25. J. K. Tee, F. Peng and H. K. Ho, *Biochemical Pharmacology*, 2019, **160**, 24-33.
26. G. Amoabediny, F. Haghirsadat, S. Naderinezhad, M. N. Helder, E. Akhoundi Kharanaghi, J. Mohammadnejad Arough and B. Zandieh-Doulabi, *International Journal of Polymeric Materials and Polymeric Biomaterials*, 2018, **67**, 383-400.
27. L. Rao, R. Tian and X. Chen, *ACS Nano*, 2020, **14**, 2569-2574.
28. A. Akbarzadeh, R. Rezaei-Sadabady, S. Davaran, S. W. Joo, N. Zarghami, Y. Hanifehpour, M. Samiei, M. Kouhi and K. Nejati-Koshki, *Nanoscale Res Lett*, 2013, **8**, 102-102.
29. A. D. Bangham, *BioEssays*, 1995, **17**, 1081-1088.
30. S. Joshi, M. T. Hussain, C. B. Roces, G. Anderluzzi, E. Kastner, S. Salmaso, D. J. Kirby and Y. Perrie, *International Journal of Pharmaceutics*, 2016, **514**, 160-168.
31. K. He and M. Tang, *Chemico-Biological Interactions*, 2018, **295**, 13-19.
32. O. Et-Thakafy, N. Delorme, C. Gaillard, C. Mériadec, F. Artzner, C. Lopez and F. Guyomarc'h, *Langmuir*, 2017, **33**, 5117-5126.
33. M. J. Rohovie, M. Nagasawa and J. R. Swartz, *Bioengineering & Translational Medicine*, 2017, **2**, 43-57.
34. I. Balke and A. Zeltins, *Advanced Drug Delivery Reviews*, 2019, **145**, 119-129.
35. J. Fuenmayor, F. Gòdia and L. Cervera, *New Biotechnology*, 2017, **39**, 174-180.
36. P. W. Lee, S. A. Isarov, J. D. Wallat, S. K. Molugu, S. Shukla, J. E. P. Sun, J. Zhang, Y. Zheng, M. Lucius Dougherty, D. Konkolewicz, P. L. Stewart, N. F. Steinmetz, M. J. A. Hore and J. K. Pokorski, *Journal of the American Chemical Society*, 2017, **139**, 3312-3315.
37. M. O. Mohsen, D. E. Speiser, A. Knuth and M. F. Bachmann, *WIREs Nanomedicine and Nanobiotechnology*, 2020, **12**, e1579.
38. M. Marchetti, G. J. L. Wuite and W. H. Roos, *Current Opinion in Virology*, 2016, **18**, 82-88.
39. R. Rachel, M. Bettstetter, B. P. Hedlund, M. Häring, A. Kessler, K. O. Stetter and D. Prangishvili, *Archives of Virology*, 2002, **147**, 2419-2429.
40. J. S. Lee and J. Feijen, *Journal of Controlled Release*, 2012, **161**, 473-483.

41. K. Jaskiewicz, M. Makowski, M. Kappl, K. Landfester and A. Kroeger, *Langmuir*, 2012, **28**, 12629-12636.
42. C. R. Heald, S. Stolnik, K. S. Kujawinski, C. De Matteis, M. C. Garnett, L. Illum, S. S. Davis, S. C. Purkiss, R. J. Barlow and P. R. Gellert, *Langmuir*, 2002, **18**, 3669-3675.
43. S. E. Webber, *The Journal of Physical Chemistry B*, 1998, **102**, 2618-2626.
44. Y. Y. Yang, Y. Wang, R. Powell and P. Chan, *Clin Exp Pharmacol Physiol*, 2006, **33**, 557-562.
45. V. P. Torchilin, *European Journal of Pharmaceutical Sciences*, 2000, **11**, S81-S91.
46. D. A. Smith, K. Beaumont, T. S. Maurer and L. Di, *Journal of Medicinal Chemistry*, 2019, **62**, 2245-2255.
47. R. Oun, Y. E. Moussa and N. J. Wheate, *Dalton Transactions*, 2018, **47**, 6645-6653.
48. C. A. Lipinski, *Journal of Pharmacological and Toxicological Methods*, 2000, **44**, 235-249.
49. F. M. Veronese and A. Mero, *BioDrugs*, 2008, **22**, 315-329.
50. B. Y. S. Kim, J. T. Rutka and W. C. W. Chan, *New England Journal of Medicine*, 2010, **363**, 2434-2443.
51. P. Fonte, F. Araújo, C. Silva, C. Pereira, S. Reis, H. A. Santos and B. Sarmiento, *Biotechnology Advances*, 2015, **33**, 1342-1354.
52. G. Hu, H. Zhang, L. Zhang, S. Ruan, Q. He and H. Gao, *Int J Pharm*, 2015, **496**, 1057-1068.
53. M. Nag, V. Gajbhiye, P. Kesharwani and N. K. Jain, *Colloids Surf B Biointerfaces*, 2016, **148**, 363-370.
54. H. J. Cho, I. S. Yoon, H. Y. Yoon, H. Koo, Y. J. Jin, S. H. Ko, J. S. Shim, K. Kim, I. C. Kwon and D. D. Kim, *Biomaterials*, 2012, **33**, 1190-1200.
55. W. Tao, J. Zhang, X. Zeng, D. Liu, G. Liu, X. Zhu, Y. Liu, Q. Yu, L. Huang and L. Mei, *Adv Healthc Mater*, 2015, **4**, 1203-1214.
56. J. Yang, H. Chen, I. R. Vlahov, J.-X. Cheng and P. S. Low, *Journal of Pharmacology and Experimental Therapeutics*, 2007, **321**, 462.
57. C. S. Chern, *Progress in Polymer Science*, 2006, **31**, 443-486.
58. A. Matsumoto, N. Murakami, H. Aota, J.-i. Ikeda and I. Capek, *Polymer*, 1999, **40**, 5687-5690.
59. U. Yildiz, K. Landfester and M. Antonietti, *Macromolecular Chemistry and Physics*, 2003, **204**, 1966-1970.
60. J. M. Asua, *Progress in Polymer Science*, 2002, **27**, 1283-1346.
61. N. Bechthold and K. Landfester, *Macromolecules*, 2000, **33**, 4682-4689.
62. C. Autran, J. C. de la Cal and J. M. Asua, *Macromolecules*, 2007, **40**, 6233-6238.
63. W. S. Saad and R. K. Prud'homme, *Nano Today*, 2016, **11**, 212-227.
64. O. Thioune, H. Fessi, J. P. Devissaguet and F. Puisieux, *International Journal of Pharmaceutics*, 1997, **146**, 233-238.

65. S. F. Chin, S. C. Pang and S. H. Tay, *Carbohydrate Polymers*, 2011, **86**, 1817-1819.
66. T. Govender, S. Stolnik, M. C. Garnett, L. Illum and S. S. Davis, *Journal of Controlled Release*, 1999, **57**, 171-185.
67. M. R. Kulterer, M. Reischl, V. E. Reichel, S. Hribernik, M. Wu, S. Köstler, R. Kargl and V. Ribitsch, *Colloids and Surfaces A: Physicochemical and Engineering Aspects*, 2011, **375**, 23-29.
68. H.-z. Zhang, X.-m. Li, F.-p. Gao, L.-r. Liu, Z.-m. Zhou and Q.-q. Zhang, *Drug Delivery*, 2010, **17**, 48-57.
69. X. Li, N. Anton, C. Arpagaus, F. Bellesteix and T. F. Vandamme, *Journal of Controlled Release*, 2010, **147**, 304-310.
70. R. Deshmukh, P. Wagh and J. Naik, *Drying Technology*, 2016, **34**, 1758-1772.
71. F. Iskandar, L. Gradon and K. Okuyama, *Journal of Colloid and Interface Science*, 2003, **265**, 296-303.
72. S. H. Lee, D. Heng, W. K. Ng, H.-K. Chan and R. B. H. Tan, *International Journal of Pharmaceutics*, 2011, **403**, 192-200.
73. J. Broadhead, S. K. Edmond Rouan and C. T. Rhodes, *Drug Development and Industrial Pharmacy*, 1992, **18**, 1169-1206.
74. D. A. Shipp, *Polymer Reviews*, 2011, **51**, 99-103.
75. R. Whitfield, A. Anastasaki, V. Nikolaou, G. R. Jones, N. G. Engelis, E. H. Discekici, C. Fleischmann, J. Willenbacher, C. J. Hawker and D. M. Haddleton, *Journal of the American Chemical Society*, 2017, **139**, 1003-1010.
76. D. Vinciguerra, J. Tran and J. Nicolas, *Chemical Communications*, 2018, **54**, 228-240.
77. K. Matyjaszewski and J. Xia, *Chemical Reviews*, 2001, **101**, 2921-2990.
78. J. Nicolas, Y. Guillaneuf, C. Lefay, D. Bertin, D. Gigmes and B. Charleux, *Progress in Polymer Science*, 2013, **38**, 63-235.
79. S. Perrier, *Macromolecules*, 2017, **50**, 7433-7447.
80. J. Chiefari, Y. K. Chong, F. Ercole, J. Krstina, J. Jeffery, T. P. T. Le, R. T. A. Mayadunne, G. F. Meijs, C. L. Moad, G. Moad, E. Rizzardo and S. H. Thang, *Macromolecules*, 1998, **31**, 5559-5562.
81. R. A. E. Richardson, T. R. Guimarães, M. Khan, G. Moad, P. B. Zetterlund and S. Perrier, *Macromolecules*, 2020, **53**, 7672-7683.
82. M. H. Stenzel, L. Cummins, G. E. Roberts, T. P. Davis, P. Vana and C. Barner-Kowollik, *Macromolecular Chemistry and Physics*, 2003, **204**, 1160-1168.
83. A. Goto, K. Sato, Y. Tsujii, T. Fukuda, G. Moad, E. Rizzardo and S. H. Thang, *Macromolecules*, 2001, **34**, 402-408.
84. G. Gody, T. Maschmeyer, P. B. Zetterlund and S. Perrier, *Macromolecules*, 2014, **47**, 3451-3460.

85. A. Kerr, M. Hartlieb, J. Sanchis, T. Smith and S. Perrier, *Chemical Communications*, 2017, **53**, 11901-11904.
86. C. Barner-Kowollik, T. P. Davis and M. H. Stenzel, *Australian Journal of Chemistry*, 2006, **59**, 719-727.
87. D. C. McLeod and N. V. Tsarevsky, *Journal of Polymer Science Part A: Polymer Chemistry*, 2016, **54**, 1132-1144.
88. A. W. Jackson, L. R. Chennamaneni and P. Thoniyot, *European Polymer Journal*, 2020, **122**, 109391.
89. M. Eberhardt and P. Théato, *Macromolecular Rapid Communications*, 2005, **26**, 1488-1493.
90. S. Muthukrishnan, E. H. Pan, M. H. Stenzel, C. Barner-Kowollik, T. P. Davis, D. Lewis and L. Barner, *Macromolecules*, 2007, **40**, 2978-2980.
91. A. Sanchez-Sanchez, I. Asenjo-Sanz, L. Buruaga and J. A. Pomposo, *Macromolecular Rapid Communications*, 2012, **33**, 1262-1267.
92. M. Destarac, *Polymer Reviews*, 2011, **51**, 163-187.
93. M. L. Coote, E. H. Krenske and E. I. Izgorodina, *Macromolecular Rapid Communications*, 2006, **27**, 473-497.
94. D. J. Keddie, *Chemical Society Reviews*, 2014, **43**, 496-505.
95. E. Rizzardo, M. Chen, B. Chong, G. Moad, M. Skidmore and S. H. Thang, *Macromolecular Symposia*, 2007, **248**, 104-116.
96. C. Barner-Kowollik, M. Buback, B. Charleux, M. L. Coote, M. Drache, T. Fukuda, A. Goto, B. Klumperman, A. B. Lowe, J. B. McLeary, G. Moad, M. J. Monteiro, R. D. Sanderson, M. P. Tonge and P. Vana, *Journal of Polymer Science Part A: Polymer Chemistry*, 2006, **44**, 5809-5831.
97. S. Perrier and P. Takolpuckdee, *Journal of Polymer Science Part A: Polymer Chemistry*, 2005, **43**, 5347-5393.
98. G. Moad, *Journal of Polymer Science Part A: Polymer Chemistry*, 2019, **57**, 216-227.
99. M. L. Coote and D. J. Henry, *Macromolecules*, 2005, **38**, 1415-1433.
100. A. Theis, M. H. Stenzel, T. P. Davis, M. L. Coote and C. Barner-Kowollik, *Australian Journal of Chemistry*, 2005, **58**, 437-441.
101. I. Kulai, Z. Voitenko, S. Mazières and M. Destarac, *Macromolecules*, 2019, **52**, 8323-8331.
102. I. Kulai, O. Brusylovets, Z. Voitenko, S. Harrisson, S. Mazières and M. Destarac, *ACS Macro Letters*, 2015, **4**, 809-813.
103. R. T. A. Mayadunne, E. Rizzardo, J. Chiefari, Y. K. Chong, G. Moad and S. H. Thang, *Macromolecules*, 1999, **32**, 6977-6980.
104. M. Buback and P. Vana, *Macromolecular Rapid Communications*, 2006, **27**, 1299-1305.
105. M. L. Coote and L. Radom, *Journal of the American Chemical Society*, 2003, **125**, 1490-1491.
106. D. J. Keddie, G. Moad, E. Rizzardo and S. H. Thang, *Macromolecules*, 2012, **45**, 5321-5342.

107. C. L. McCormick, B. S. Sumerlin, B. S. Lokitz and J. E. Stempka, *Soft Matter*, 2008, **4**, 1760-1773.
108. X. Yan, R. Ramos, E. Hoibian, C. Soulage, P. Alcouffe, F. Ganachaud and J. Bernard, *ACS Macro Letters*, 2017, **6**, 447-451.
109. W.-M. Wan and C.-Y. Pan, *Polymer Chemistry*, 2010, **1**, 1475-1484.
110. S. Parkinson, N. S. Hondow, J. S. Conteh, R. A. Bourne and N. J. Warren, *Reaction Chemistry & Engineering*, 2019, **4**, 852-861.
111. S. L. Canning, G. N. Smith and S. P. Armes, *Macromolecules*, 2016, **49**, 1985-2001.
112. X. Zhang, J. Rieger and B. Charleux, *Polymer Chemistry*, 2012, **3**, 1502-1509.
113. A. Blanz, J. Madsen, G. Battaglia, A. J. Ryan and S. P. Armes, *Journal of the American Chemical Society*, 2011, **133**, 16581-16587.
114. L. D. Blackman, S. Varlas, M. C. Arno, Z. H. Houston, N. L. Fletcher, K. J. Thurecht, M. Hasan, M. I. Gibson and R. K. O'Reilly, *ACS Central Science*, 2018, **4**, 718-723.
115. P. Yang, L. P. D. Ratcliffe and S. P. Armes, *Macromolecules*, 2013, **46**, 8545-8556.
116. W.-M. Wan and C.-Y. Pan, *Macromolecules*, 2010, **43**, 2672-2675.
117. E. E. Brotherton, F. L. Hatton, A. A. Cockram, M. J. Derry, A. Czajka, E. J. Cornel, P. D. Topham, O. O. Mykhaylyk and S. P. Armes, *Journal of the American Chemical Society*, 2019, **141**, 13664-13675.
118. N. J. Warren, O. O. Mykhaylyk, D. Mahmood, A. J. Ryan and S. P. Armes, *Journal of the American Chemical Society*, 2014, **136**, 1023-1033.
119. C. J. Ferguson, R. J. Hughes, D. Nguyen, B. T. T. Pham, R. G. Gilbert, A. K. Serelis, C. H. Such and B. S. Hawkett, *Macromolecules*, 2005, **38**, 2191-2204.
120. P. Gurnani, C. Sanchez-Cano, K. Abraham, H. Xandri-Monje, A. B. Cook, M. Hartlieb, F. Lévi, R. Dallmann and S. Perrier, *Macromolecular Bioscience*, 2018, **18**, 1800213.
121. P. Gurnani, A. M. Lunn and S. Perrier, *Polymer*, 2016, **106**, 229-237.
122. P. Gurnani, A. B. Cook, R. A. E. Richardson and S. Perrier, *Polymer Chemistry*, 2019, **10**, 1452-1459.

2 The Effect Heterogeneous Conditions in Emulsion Polymerisation have on RAFT Agent Performance

2.1 Overview

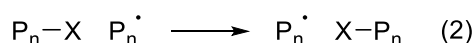
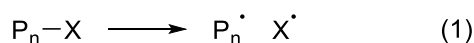
In this chapter, a modified version of conventional RAFT emulsion polymerisation is presented and used to produce both uniform nanoparticles and low dispersity polymers. The impact heterogeneous conditions have on RAFT control will also be explored.

2.2 Introduction

2.2.1 Emulsion Polymerisation

As described in chapter 1, emulsion polymerisation uses a hydrophobic monomer, a hydrophilic initiator and an amphiphilic surfactant to produce polymeric nanoparticles. Whilst these nanoparticles may be the desired product, they can also be collected and dissolved in organic solvent to yield their free polymers¹. These free polymers can also be produced by solution polymerisation; however, performing a polymerisation in emulsion confers several advantages to the synthesis. The principal advantage of emulsion polymerisation is a reduced time needed to reach full conversion². This increased rate stems from the artificially high concentration of monomer within the micelles and growing particles, acting to mimic bulk conditions. In this way, low k_p monomers, such as styrene, can be polymerised at considerably increased rates³. A second advantage of emulsion polymerisation is the use of water as the solvent. Whilst sometimes controversially described as a "green solvent"⁴, water does possess an undeniably high heat capacity⁵; helping to stabilise the systems temperature especially at a large scale⁶. Due to these advantages, emulsion polymerisation is viewed as a useful route to produce

polymers as well as nanoparticles. Whilst Free Radical Polymerisation (FRP) can be used to produce uniform nanoparticles⁷, it cannot produce low dispersity polymers; for this, a Reversible Deactivation Radical Polymerisation (RDRP) strategies are needed⁸. Described in Chapter 1 (Section 1.3), RDRP relies on the use of an additive to reduce the overall radical concentration present at a given time; increasing control over the polymerisation. Two main classes of RDRP exist; one in which the growing polymer chains are reversibly activated by a separate additive (1) and those in which it is reversibly activated by transfer of the additive to another growing chain (2).



Examples of scenario 1 include Nitroxide-Mediated Polymerisation (NMP)⁹ and Atom Transfer Radical Polymerisation (ATRP)¹⁰; whilst Reversible Addition-Fragmentation chain Transfer (RAFT)¹¹ is an example of scenario 2. NMP¹² and ATRP¹³ have both been used in emulsion polymerisation; however, to ensure reversible deactivation, care must be taken to ensure that X^{\bullet} remains within the same phase as the propagating radical. This requirement limits the applications of NMP and ATRP to emulsion polymerisation. Conversely, RAFT is more amenable to the heterogeneous conditions of emulsion polymerisation¹⁴ as the RAFT end group is always attached to a polymer chain; preventing loss by phase transfer. RAFT has therefore been widely used in emulsion polymerisation and is explored further in the next section.

2.2.2 RAFT in Emulsion

A wide variety of RAFT agents have been prepared¹⁵⁻¹⁸ and their chemical properties extensively explored in Chapter 1 (Section 1.4). For emulsion polymerisation, however, the physical properties of RAFT agents, such as solubility, are also highly important. RAFT agents ranging from fully

hydrophobic to fully hydrophilic have all been utilised for emulsion polymerisation; the effect of solubility is reviewed in the following subsections.

2.2.2.1 Hydrophobic RAFT Agents

Fully hydrophobic RAFT agents are among the earliest used for RAFT emulsion¹⁹. The hydrophobic nature of these RAFT agents, leads them to be largely insoluble in the aqueous phase of the emulsion. The RAFT agent instead dissolves in the monomer droplets present at the start of the polymerisation. As discussed in Chapter 1 (Section 1.2.1), emulsion polymerisation does not primarily take place within the monomer droplets and instead occurs within the surfactant micelles present. The RAFT agent must therefore be transported from the starting monomer droplets to the micelles in order to control the polymerisation taking place there. Fully hydrophobic RAFT agents have intrinsically low water solubility, retarding their transport through the aqueous phase, and leading to poor polymer control^{20, 21}. One solution to this problem was presented by Rizzardo, Gilbert and co-workers²², who utilized water-miscible organic solvents, in this case acetone, to improve RAFT agent solubility and transport; improving polymer control. As well as difficulties with polymer control, fully hydrophobic RAFT agents are also incapable of stabilising the formed nanoparticles, commonly leading to coagulation²⁰.

2.2.2.2 Hydrophilic RAFT Agents

Fully hydrophilic RAFT agents have also been used for emulsion polymerisation. The hydrophilic nature of these RAFT agents provide improved nanoparticle stabilisation compared with hydrophobic RAFT agents discussed above. An early example of a fully hydrophilic RAFT agent for emulsion polymerisation was provided by Uzulina²³ *et al.* (Figure 10).

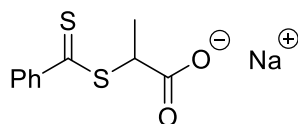


Figure 10: The chemical structure of the RAFT agent used by Uzulina²³ *et al.* for an emulsion polymerisation of styrene

This RAFT agent and its neutral equivalent was used in a solution and emulsion polymerisation of styrene. Whilst the solution polymerisation produced well-controlled polymers ($\bar{D} < 1.2$), the emulsion polymerisation did not ($\bar{D} > 1.4$). To explain the lack of RAFT control, it is necessary to highlight that emulsion polymerisations begins in the aqueous phase, where the monomer concentration is very low. The authors postulate that this very low monomer concentration, coupled with the increased presence of the water-soluble RAFT agent, led to very rapid chain transfer occurring during the initial stages of polymerisation. This rapid chain transfer would increase the time taken to produce polymer chains of sufficient length to enter into monomer micelles (z-mers). The authors state that this delay in z-mer formation and entry would be expected to decrease the homogeneity of particle nucleation; broadening polymer dispersity.

2.2.2.3 Amphiphilic RAFT Agents

Solely hydrophobic and hydrophilic RAFT agents suffer from low concentrations within the growing particles, leading to poor polymer control as described *vide supra*. A solution to this is to use an amphiphilic RAFT agent that can self-assemble into the starting micelles present at the beginning of the polymerisation. These starting micelles are where the polymerisation primarily takes place; forming them from RAFT agent therefore ensures that it is continually present. This method was exploited by Gurnani *et al.*²⁴ who prepared an amphiphilic diblock copolymer p(PEGA₈-*b*-BA₈) ($\bar{D} = 1.13$) in solution, which was then used as the surfactant for an emulsion polymerisation of butyl acrylate (BA). Whilst uniform nanoparticles were produced, the final

polymer dispersity were broad ($\bar{D} = 1.39$ for $DP = 100$ and $\bar{D} = 1.60$ for $DP = 150$). To explain this unexpected result, it is necessary to review the effects emulsion polymerisation may be having on RAFT polymerisation.

2.2.3 RAFT Control in Emulsion Polymerisation

An important parameter when considering RAFT polymerisation is the probability of chain transfer (ρ_{tr}). This value is an effective measure of RAFT agent efficiency and is given by the rate of chain transfer divided by the total rate of all addition reactions (Equation 1)²⁵.

$$\rho_{tr} = \frac{k_{tr} [RAFT]}{k_{tr} [RAFT] + k_p [M]} \quad (1)$$

Where k_{tr} and k_p are the rate constants of chain transfer and propagation respectively and $[RAFT]$ and $[M]$ are the concentration of RAFT agent and monomer. The chain transfer constant (C_T) is defined as the rate constant of chain transfer divided by the rate constant of propagation (Equation 2).

$$C_T = \frac{k_{tr}}{k_p} \quad (2)$$

Rearranged, this equation gives the rate constant of transfer as being equal to the rate constant of propagation multiplied by the chain transfer constant. This new expression can then be substituted into Equation 1 to give the following.

$$\rho_{tr} = \frac{k_p C_T [RAFT]}{k_p C_T [RAFT] + k_p [M]} \quad (3)$$

Equation 3 can then be simplified by cancelling out all k_p terms and then dividing by $[RAFT]$ to give equation 4.

$$\rho_{tr} = \frac{C_T}{C_T + \frac{[M]}{[RAFT]}} \quad (4)$$

This final equation shows that for fixed values of C_T , the probability of a chain transfer event occurring, and hence the efficiency of a RAFT agent, increases

as the monomer concentration drops relative to that of the RAFT agent. As a low monomer to RAFT agent ratio would produce very low molecular weight chains²⁶, it would not seem at first to be a useful way of increasing RAFT agent control. However, by keeping the monomer concentration artificially low and slowly feeding more in, higher molecular weight polymers can be obtained along with this increase in RAFT agent efficiency. Whilst this feeding can be done manually²⁷, in emulsion polymerisation slow monomer diffusion from the monomer droplets to the growing particles, provides this mechanism intrinsically. This in-built feeding mechanism would therefore be expected to increase RAFT control during emulsion polymerisation. However, as described *vide supra*, poor RAFT control in emulsion polymerisation was observed in all cases, even when the RAFT agent was present at the locus of polymerisation (Section 2.2.2.3). One possible explanation for the poor overall polymer control observed by Gurnani *et al.*²⁴ is that there is no movement of radicals between growing particles as the amphiphilic reinitiating group is effectively locked into its starting particle. This lack of radical movement would lead to inhomogeneity in particle nucleation, broadening polymer dispersity.

2.2.4 Transfer Surfactants

To provide good control over the polymerisation in emulsion, the RAFT agent should be amphiphilic, ensuring a high concentration of it within growing particles (Section 2.2.2.3). However, the reinitiating group should also be hydrophilic in order to allow movement of radicals between growing particles and homogenous nucleation. An idealised RAFT agent could therefore be envisioned in which the Z-group and R-group are fully hydrophobic and hydrophilic respectively (Figure 11).

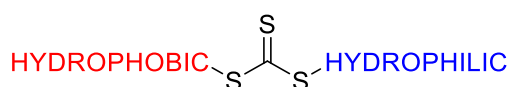


Figure 11: The generalised structure of a transurf, showing a fully hydrophobic Z-group (red) and fully hydrophilic R-group (blue)

To distinguish this group of RAFT agents from the amphiphilic diblocks described in Section 2.2.2.3, they will be termed Transfer Surfactants (Transurfs); using the nomenclature begun by Goyet *et al.*²⁸. This group of RAFT agents would be expected to provide improved polymerisation control under emulsion conditions as described *vide supra* (Section 2.2.3).

2.2.5 Objectives

The objective of this chapter is to investigate whether transurf style RAFT agents can be used in conjunction with emulsion polymerisation to improve overall RAFT control. To do this, the control of two RAFT agents bearing fully hydrophobic Z-groups and fully hydrophilic R-groups in emulsion will be investigated and compared to solution polymerisation.

2.3 Experimental

2.3.1 Materials

Monomers; butyl acrylate (BA), butyl methacrylate (BMA), methyl methacrylate (MMA), hexyl methacrylate (HMA), decyl methacrylate (DMA) and lauryl methacrylate (LMA) were purchased from Sigma Aldrich and passed through a short aluminium oxide column to remove inhibitor prior to use. The initiator 2,2'-azobis[N-(2-carboxyethyl)-2-methylpropionamide]tetrahydrate (VA-057) and dimethyl 2,2'-azobis(2-methylpropionate) (V-601) were purchased from Wako chemicals and used as provided. The starting RAFT agent, CTA-acid, was provided by Lubrizol and recrystallized thrice from hot hexane before use. The distilled water was prepared on site.

2.3.2 Analytical Techniques

2.3.2.1 Size Exclusion Chromatography

SEC was performed on an Agilent Infinity II MDS instrument equipped with differential refractive index (DRI) and multiple wavelength UV detectors, one of which is set to 309 nm. The column used for separation is a PLgel Mixed C columns (300 x 7.5 mm) and a PLgel 5 μm guard column. The eluent is THF with 2 % triethylamine (TEA) and 0.01 % butylated hydroxytoluene (BHT) additives. Samples were run at 1ml/min at 30 °C. Poly(methyl methacrylate) (pMMA) (2000 – 1,500,000 g mol⁻¹) and polystyrene standards (Agilent EasyVials) were used for calibration, analysis was carried out compared to the pMMA standards. Analyte samples were filtered through a GVHP membrane with 0.22 μm pore size before injection. Experimental molar mass (M_n , SEC) and dispersity (\bar{D}) values of synthesized polymers were determined by conventional calibration using Agilent GPC/SEC software.

2.3.2.2 Dynamic Light Scattering

Samples were prepared by diluting nanoparticle latexes 1000-fold with DI water to a final concentration of 0.2 mg/mL. DLS measurements were

performed on a MALVERN Zetasizer Nano ZS operating at 25 °C with a 4 mW He-Ne 633 nm laser module. Measurements were made in back scattering mode at an angle of 173°. Measurements were performed in triplicate with automatic attenuation selection and measurement position. The results were analysed using Malvern DTS 6.20 software.

2.3.2.3 Nuclear Magnetic Resonance

^1H NMR spectra were recorded on a Bruker Avance 300 spectrometer (300 MHz) at 21 °C in deuterated acetone. For ^1H NMR spectroscopy, the delay time (d_1) was 2 s. Chemical shift values (δ) are reported in ppm downfield of a tetramethylsilane (TMS) standard. Mestrenova software was used to analyse the results.

2.3.2.4 Conversion Calculations

Monomer conversion was calculated directly from ^1H NMR spectra. Briefly, the integral corresponding to the vinyl proton shown below ($\delta \sim 6.5$) was compared to the integrals of the polymer sidechain protons ($\delta \sim 1.66$ and 1.47). This proton was chosen, as it did not overlap with the broad peak corresponding to water. For clarity, two example conversion calculations from the NMR are provided below (Figure 12).

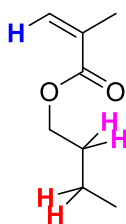
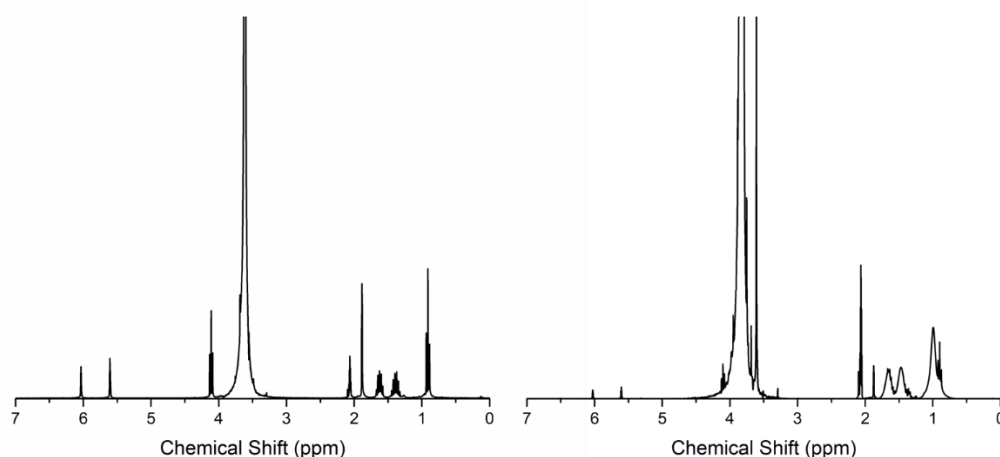


Figure 12: Above - The protons used in calculating monomer conversion by NMR; vinyl proton (blue) and sidechain protons (pink and red). Below – example NMRs from a kinetic following the formation of pBMA₁₀₀, taken at 20 (left) and 60 (right) minutes.



To calculate monomer conversion, the Integral value of the sidechain protons between 1.4 – 1.6 ppm was calculated and set as 4 as a standard. The vinyl proton of the monomer at ~6.1 ppm was calculated for both spectra as 0.849 for 20 minutes and 0.147 for 60 minutes. By assuming that this vinyl proton has an integral of 1 at 0% conversion and 0 at 100% conversion, the measured integral values can be converted to monomer conversions of 15.1% (20 minutes) and 85.3% (60 minutes).

2.3.3 Chemistry Techniques

2.3.3.1 PEG-CTA Synthesis

CTA-acid (1.37 g, 3 equiv, 3.76 mmol) was dissolved in 2.813 mL of an oxalyl chloride DCM solution (2 M) (4.5 equiv, 5.64 mmol) to yield a bright yellow solution. Three drops of anhydrous DMF were added to this solution, resulting in rapid gas generation and a change in colour to orange. After effervescence had stopped, the solution was sealed and gently stirred at room temperature for 1 h. Separately, 2.5 g of 2k MeO-PEG-OH (1 equiv, 1.25 mmol) was dissolved in 10 mL of DCM; this was then added to the reaction and left stirring overnight to yield a dark yellow solution. The product was then obtained by precipitating this solution into an 80:20 mix of hexane and diethyl ether, followed by drying overnight at 40 °C under vacuum to afford a pale yellow

powder (yield = 2.63 g 89%). ^1H NMR (CHCl_3 , 300 MHz) δ 4.27 2H $\text{COOCH}_2\text{CH}_2\text{O}$ t 6 Hz, 3.89 2H $\text{COOCH}_2\text{CH}_2\text{O}$ t 6 Hz, 3.66 176H $(\text{OCH}_2\text{CH}_2)_{44}$ m, 3.40 3H $\text{OCH}_2\text{CH}_2\text{OCH}_3$ s, 3.28 2H $\text{SCSSCH}_2\text{CH}_2$ t 5 Hz, 1.71 6H $\text{S}(\text{CH}_3)_2\text{CCOOCH}_2$ s J, 1.65 2H $\text{SCSSCH}_2\text{CH}_2$ tt 5.2 Hz, 1.27 18H $\text{SCSSCH}_2\text{CH}_2(\text{CH}_2)_9\text{CH}_3$ m, 0.90 3H $\text{CH}_2\text{CH}_2\text{CH}_3$ t 9 Hz. MS $[\text{M} + \text{Na}^+]$ calculated as 2369.2 found as 2368.9.

2.3.3.2 Critical Micellar Concentration Determination

A 0.1 mg mL^{-1} solution of Nile red (30 μL) in THF was transferred to ten 2 mL glass vials and dried in an oven at 40°C for 48 h. Separately, PEG-CTA solutions in water were prepared at the following concentrations: 50, 25, 10, 1, 0.1, 1×10^{-2} , 1×10^{-3} , 1×10^{-4} , 1×10^{-5} , and $1 \times 10^{-6} \text{ mg mL}^{-1}$. Each PEG-CTA solution (2 mL) was then added separately to the Nile red-containing vials. The vials were then sealed and placed on a roller at room temperature for a further 48 h. The fluorescence intensity of Nile red was then measured on a BioTek cytation three-plate reader using an excitation wavelength of 560 nm and an emission wavelength of 600 nm.

2.3.3.3 Emulsion Polymerisation

In a typical emulsion polymerization, 102.2 mg of PEG-CTA (1 eq, 0.046 mmol) was dissolved in 5 mL of deionized water in a 20 mL glass vial; 0.727 mL of BMA (0.649 g, 100 eq, 0.457 mmol) and 0.253 mL of a VA-057 stock solution ($0.01 \text{ g mL}^{-1} \text{ H}_2\text{O}$) (2.53 mg 0.125 eq, 0.00610 mmol) were then added to the reaction. The vial was then sealed and briefly vortexed before purging with nitrogen gas for 15 min. The reaction was then heated to 70°C in a monitored oil bath and stirred at 500 rpm for 90 min to form a white latex. Samples for kinetic measurements were withdrawn periodically with a nitrogen-purged syringe. For all other polymerizations targeting a degree of polymerization (DP) of 100, the amounts of PEG-CTA, water, and VA-057 stock solution were constant and the amount of monomer was varied to give the same molar

ratios. When targeting polymers of various DPs, the ratio of PEG-CTA to VA-057 was kept constant and the amount of monomer varied with respect to the CTA.

2.3.3.4 Diblock and Multiblock Synthesis

Polymer chain extensions were performed *in situ*, without purification of the intermediate polymer. In a typical diblock synthesis, the first block was formed as described in Section 2.3.3.3 above. The first block polymerisation mixture was removed from the oil but not exposed to air. 0.727 mL of BMA (0.649 g, 100 eq, 0.457 mmol) was then injected using a nitrogen purged syringe followed by 0.14 mL of a VA-057 stock solution (0.01 g mL⁻¹ H₂O) (2.53 mg 0.125 eq, 0.00610 mmol). The amount of VA-057 added was calculated to be equal to that consumed during the formation of the first block, giving a fixed CTA:I ratio for all blocks. After injection of monomer and initiator, the reaction was again heated to 70 °C for 90 min whilst the second block polymerised. This chain extension protocol was repeated for the synthesis of multiblocks.

2.3.3.5 Solution Polymerisation

In a typical solution polymerisation, 102.2 mg of PEG-CTA (1 eq, 0.046 mmol) was dissolved in 5 mL of dioxane in a 20 mL glass vial; 0.727 mL of BMA (0.649 g, 100 eq, 0.457 mmol) and 0.373 mL of a V-601 stock solution (0.01 g mL⁻¹ dioxane) (3.73 mg, 2.83 eq, 0.01624 mmol) were then added to the reaction. The starting V-601 concentration was adjusted to provide the same overall number of radicals as for VA-057 used in the emulsion experiments. The vial was then sealed and briefly vortexed before purging with nitrogen gas for 15 min. The reaction was then heated to 70 °C in a monitored oil bath and stirred at 500 rpm until full conversion had been reached, typically 4 hrs for acrylates and 16 hrs for methacrylates. Samples for kinetic measurements were withdrawn periodically with a nitrogen-purged syringe.

2.4 Results and Discussion

2.4.1 Investigation of CTA-Acid as a Potential Transurf

The first transurf investigated in this work was 2-(((dodecylthio)-carbonothioyl)thio)-2-methylpropanoic acid herein referred to as CTA-acid, structure below (Figure 13).

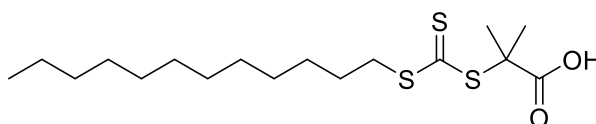


Figure 13: The chemical structure of CTA-acid (2-(Dodecylthiocarbonothioylthio)-2-methylpropionic acid)

The Z-group of CTA-acid is a hydrophobic dodecane thiol group, whilst the R-group features an ionisable carboxylic acid. Whilst insoluble in water when protonated, CTA-acid readily dissolves under basic conditions. Once in solution, the amphiphilic nature of CTA-acid should lead to self-assembly into micelles. Dynamic light scattering (DLS) reveals micelles of approximately 10 nm, demonstrating that deprotonated CTA-acid can assemble in water and act as a surfactant. Once it had been established that CTA-acid could self-assemble, it was used as the sole surfactant for an emulsion polymerisation of butyl acrylate (BA). VA-057 was chosen as the initiator as it is water-soluble across a range of pH values and does not require the use of any additional base to aid dissolution, such as is necessary with ACVA for example. The DLS spectra of the nanoparticles along with the SEC chromatogram of the polymer formed are provided below (Figure 14).

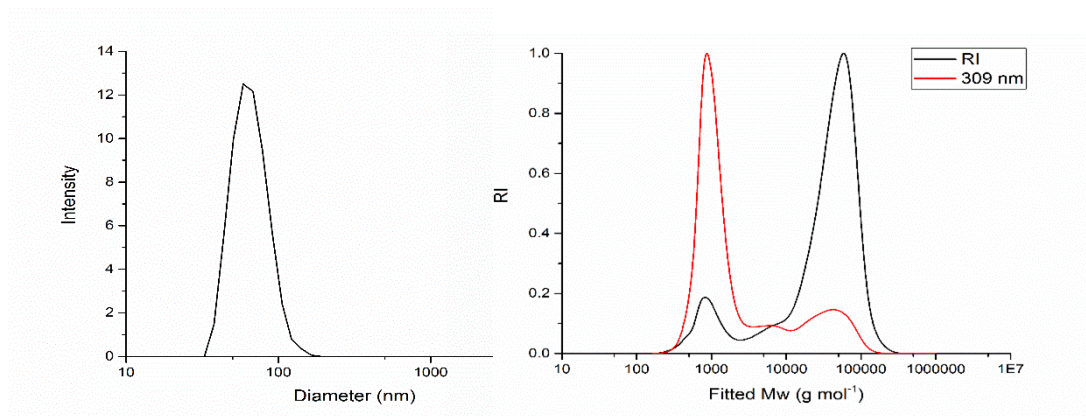


Figure 14: DLS distribution of pBA₁₀₀ nanoparticles (left) and the correspondent GPC traces (right) using both RI (black) and UV (red) detectors

The resulting nanoparticles had a narrow particle size distribution (PDI = 0.077) and a Z-average diameter of 65 nm. This suggests that deprotonated CTA-acid can indeed be used as the starting surfactant for emulsion polymerisations. The SEC chromatogram, however, is distinctly bimodal, showing one low molecular weight peak corresponding to the starting CTA-acid and a second broader peak for the polymer. SEC using UV detection at 309 nm (Figure 14 – right, red) was used to detect the presence of trithiocarbonate groups; showing poor incorporation of the RAFT agent into the polymer chains and a large quantity of unconsumed CTA-acid. Coupled with the broad dispersity and bimodal nature, this lack of RAFT agent incorporating strongly suggests that CTA-acid has not acted to control the polymerisation. To try to investigate this surprising result, a control experiment was set up whereby BA was polymerised in solution (dioxane) in the presence of CTA-acid. The SEC chromatogram of this polymerisation (Figure 15) shows a now monomodal narrow peak ($\bar{M}_w = 1.18$) and showed clear UV absorption; suggesting that the CTA-acid has now worked as an effective chain transfer agent.

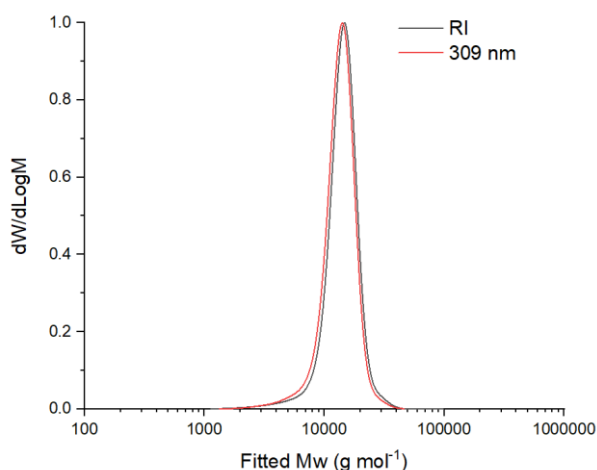


Figure 15: A SEC chromatogram for pBA₁₀₀ produced using CTA-acid in solution ($M_n = 13,500 \text{ g mol}^{-1}$), ($\bar{D} = 1.18$) using both RI (black) and UV (red) detectors.

To try to reconcile the differing results between emulsion and solution the chemical difference between the two systems were examined. The key difference is that in emulsion the CTA-acid is in its deprotonated form, whereas it is protonated in the solution polymerisation. This deprotonation would be expected to destabilise the radical formed on the reinitiating group by reducing the availability, and stabilising effect, of the carboxylic acid π -system, as discussed in Section 1.4 of Chapter 1. This destabilised R-group would retard the RAFT agents overall chain transfer ability, reducing overall polymer control. To investigate this theory, an experiment was conducted whereby the polymerisation would take place in solution but the CTA-acid would also be deprotonated. To achieve this, a water-soluble acrylate monomer, 2-hydroxy ethyl acrylate (HEA), was polymerised in the presence of CTA-acid, under basic conditions. The SEC chromatogram of this polymer was then recorded and is shown below (Figure 16).

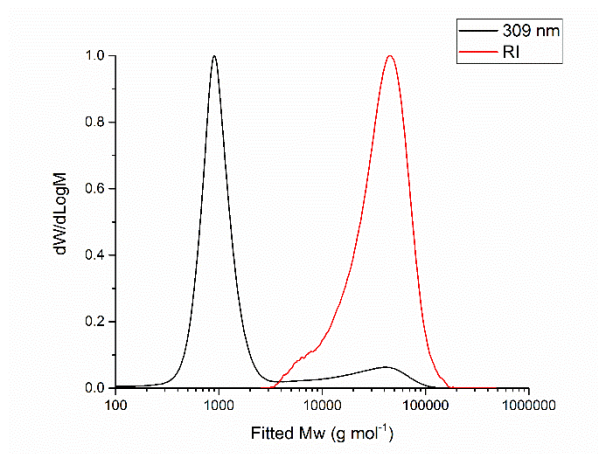


Figure 16: SEC chromatogram of pHEA₁₀₀ synthesised under basic conditions ($M_n = 26,300 \text{ g mol}^{-1}$), ($\mathcal{D} = 1.74$) using both RI (red) and UV (black) detectors.

The SEC chromatogram shows a broad polymer peak ($\mathcal{D} < 1.7$). This broad dispersity confirms that deprotonated CTA-acid has not function as an effective chain transfer agent. As CTA-acid can only act as a surfactant in its deprotonated state, it cannot be used further as a Transurf.

2.4.2 Investigation of PEG-CTA as a Potential Transurf

As CTA-acid could not be used as a Transurf, a second amphiphilic RAFT agent was designed. This second RAFT agent, structure below, features the same dodecane thiol Z-group as CTA-acid and a PEG modified R-group (Figure 17).

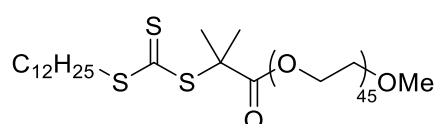


Figure 17: The chemical structure of PEG-CTA

This new transurf was synthesised by first converting CTA-acid to the acid chloride equivalent and then immediate further reaction with PEG-OH without purification (Figure 18).

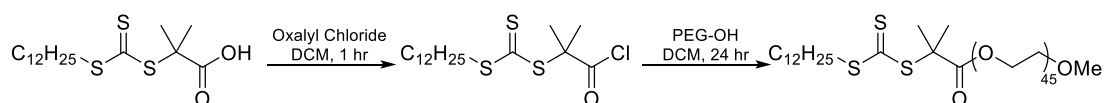


Figure 18: A chemical scheme for the synthesis of PEG-CTA from CTA-acid

The final PEG-CTA was then purified by precipitating in hexane:diethyl ether (80/20), before drying overnight in a vacuum oven. An NMR spectrum was also recorded and is provided below (Figure 19).

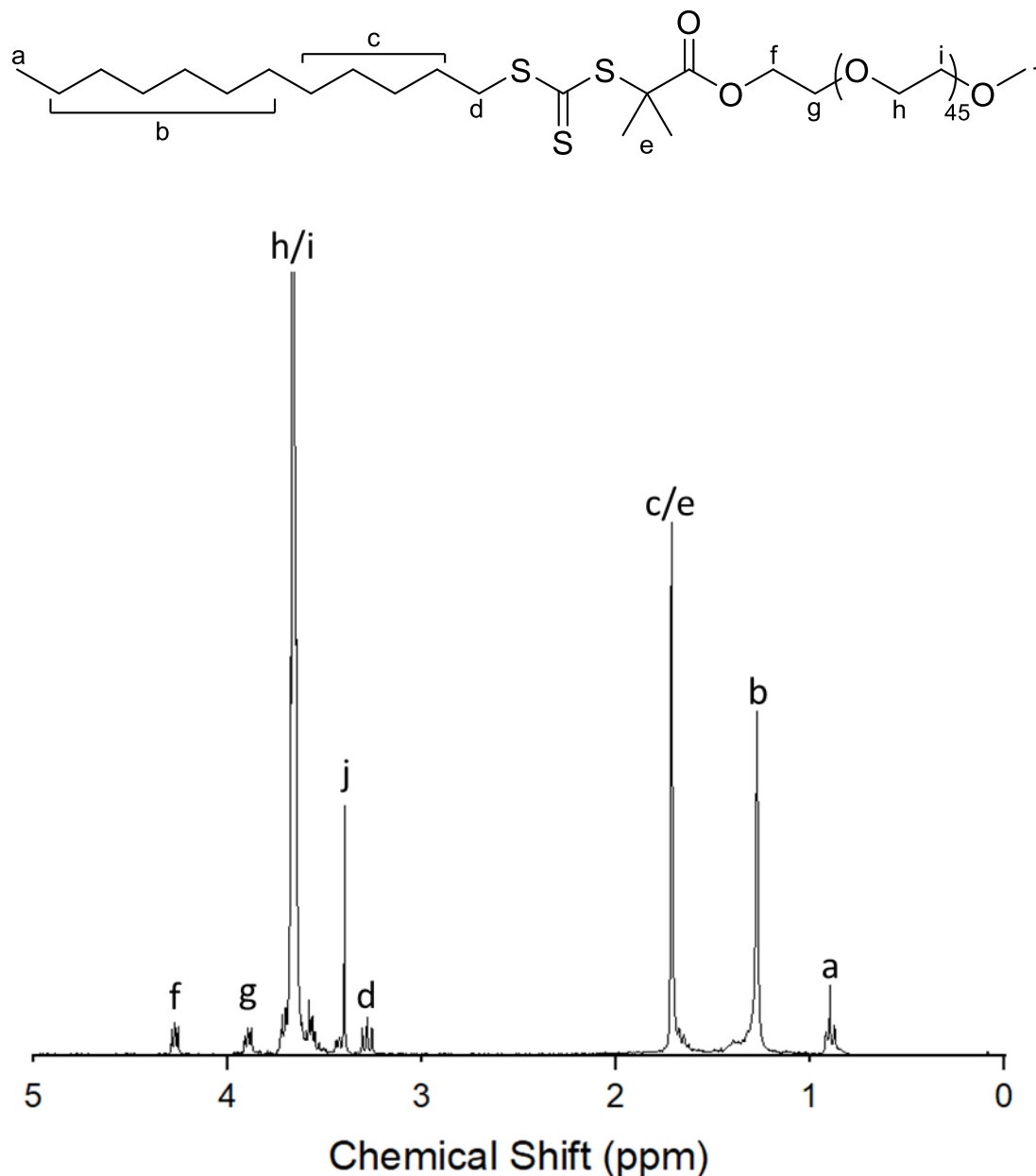


Figure 19: The ^1H NMR spectrum and assigned structure of PEG-CTA recorded at 300 MHz in CDCl_3 , integration values relative to proton a are as follows; a = 3.0, b = 11.96, c/e = 14.07, d = 2.07, f = 1.97, g = 1.98, h/i = 86.90, j = 2.96

A large number of the protons have overlapping shifts; however, two distinctive peaks can be highlighted at 4.27 and 3.28 ppm. These two peaks correspond to the two protons on the PEG chain adjacent to the ester and to

two protons adjacent to the trithiocarbonate respectively. As well as confirming the formation of an ester and the retention of the trithiocarbonate, the integrals of these two peaks (1.97 and 2.07) match, strongly suggesting the complete consumption of PEG and removal of excess CTA-acid.

As with CTA-acid, a DLS of the PEG-CTA was taken and shows micelles of approximately 21 nm in diameter (Figure 20), this size increase relative to CTA-acid can be accounted by the PEG corona of the larger surfactant and the reduction in stabilisation concurrent with moving from electrostatic to steric stabilisation.

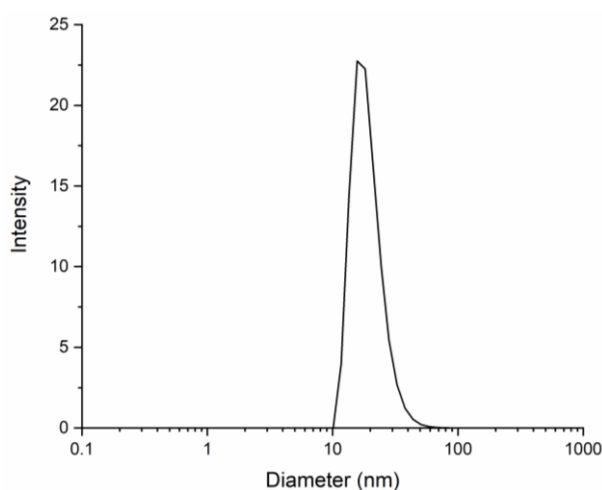


Figure 20: DLS distribution of PEG-CTA in water (0.1 mg/mL) showing micelles 21 nm in diameter

The critical micelle concentration (CMC) for PEG-CTA was also calculated using a Nile red assay²⁹ (Figure 21). This relies on the dramatic increase in fluorescence of Nile red dye when in a hydrophobic environment. This assay gave a CMC value of 0.061 mg/mL (6.98×10^{-5} M) at 298 K, in line with other polymeric surfactant values^{30, 31}.

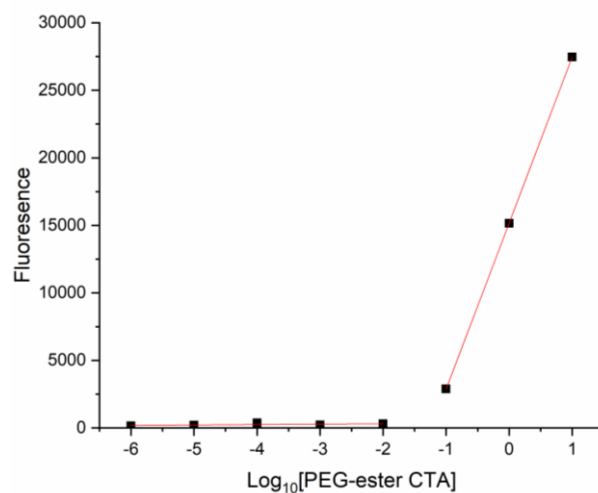


Figure 21: Plot of total fluorescence (arbitrary units) of Nile red dye in the presence of different concentrations of PEG-CTA (mg/mL)

PEG-CTA was then used as the surfactant of a BA emulsion polymerisation. It should be noted that this experiment was done under matching conditions as the CTA-acid experiment to make the two comparable. As with CTA-acid, the reaction proceeded to give a white latex indicating that polymeric nanoparticles had been formed. DLS and SEC was again used to characterise the nanoparticles and polymers (Figure 22).

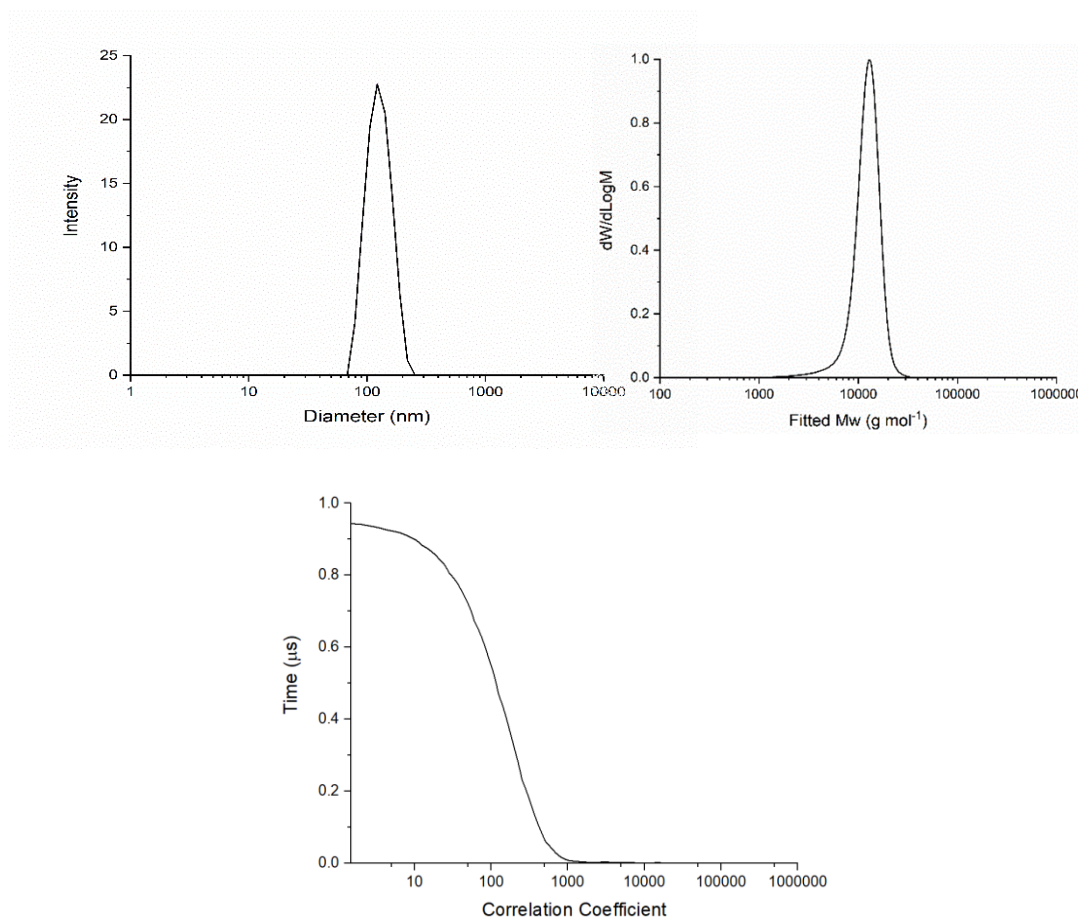


Figure 22: The DLS distribution (left) of pBA₁₀₀ nanoparticles prepared with PEG-CTA and the correspondent SEC chromatogram (right) ($M_n = 14,500 \text{ g mol}^{-1}$), ($\bar{D} = 1.13$).

DLS analysis revealed uniform nanoparticles with a Z-average diameter 120 nm and a PDI of 0.015. This was a substantial increase in particle diameter compared with particles synthesised with CTA-acid and cannot be wholly accounted for by the presence of the PEG corona. This change is instead likely a consequence of switching from an anionic to a neutral surfactant. Without the charge to stabilise the growing particles, more surfactant molecules are needed to cluster together to provide the same level of stabilisation, leading to larger particles. In stark contrast to the earlier attempts with CTA-acid, the SEC chromatogram now shows one narrow dispersity peak ($M_n = 14,500 \text{ g mol}^{-1}$, $\bar{D} = 1.13$). This distinct improvement in polymer control can be attributed to improved reinitiating group radical stabilisation.

As laid out in Section 2.2.3, RAFT polymerisation under emulsion would also be expected to yield lower dispersity polymers than for solution polymerisation. To confirm this theory, BA was polymerised with PEG-CTA in solution (dioxane) under the same conditions as for the emulsion experiment; note that a longer polymerisation time of 4 hrs was needed to reach full conversion. The SEC chromatograms of the polymer produced in solution as well as emulsion are provided below (Figure 23).

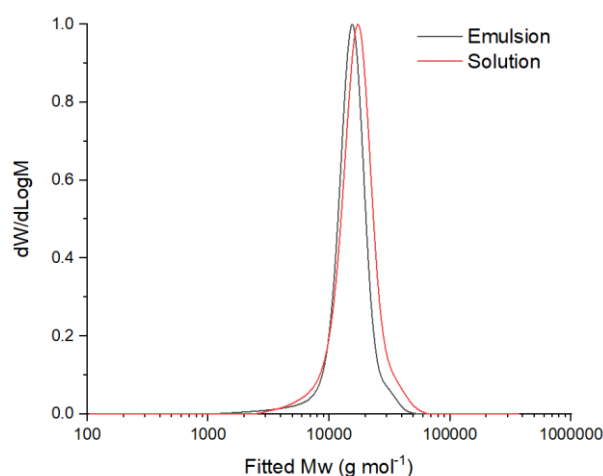


Figure 23: An overlay of the SEC chromatograms of pBA₁₀₀ produced in emulsion (black) ($M_n = 14,500 \text{ g mol}^{-1}$), ($\bar{D} = 1.13$) and solution (red) ($M_n = 14,900 \text{ g mol}^{-1}$), ($\bar{D} = 1.19$)

The SEC shows that the polymer produced by both emulsion and solution was well controlled, with $\bar{D} < 1.2$ in both cases. However, the dispersity value of the polymer produced by emulsion (1.13) is lower than that for solution (1.19); confirming that emulsion polymerisation has improved RAFT control. Muller *et al.*³² derived an equation for the relationship between the polymer dispersity (\bar{D}) and the RAFT chain transfer constant (C_T) (Equation 5).

$$\bar{D} = 1 + \frac{1}{DP} + \frac{2-x}{x} \frac{1}{C_T} \quad 5$$

Where DP is the targeted degree of polymerisation and x is fractional conversion. Assuming full conversion, equation 5 can then be rearranged to allow the calculation of C_T from experimentally determine dispersity values (Equation 6).

$$C_T = \frac{1}{D - 1 - \frac{1}{DP}} \quad 6$$

Equation 6 was then used to calculate the chain transfer constant (C_T) for BA with PEG-CTA under emulsion and solution conditions, giving values of 8.33 and 5.56 respectively. By using Equation 4, these chain transfer constants can in turn be converted to probability of chain transfer (p_{tr}); 7.69% and 5.24% for emulsion and solution conditions respectively. Emulsion polymerisation can therefore be used to improve RAFT control; however, as discussed earlier (Section 2.2.2.3), this is not always the case. As described *vide supra*, the poor control sometimes observed for RAFT emulsion may be the result of heterogeneous nucleation due to the absence of radical movement between growing particles. To investigate this theory further, a third starting RAFT agent was produced where the R-group featured both BA and PEG blocks (Figure 24). Importantly the amphiphilic nature of the R-group would be expected to inhibit its transport between growing particles

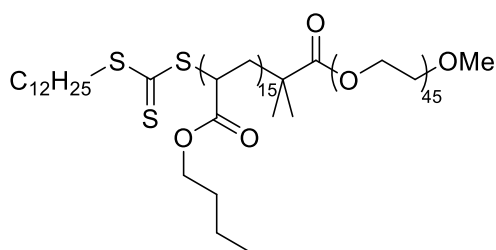


Figure 24: The chemical structure of PEG-BA-CTA

This new RAFT agent was then used for the emulsion polymerisation of BA under matching conditions to those used with PEG-CTA. The polymers comprising of the nanoparticles formed, were then analysed by SEC (Figure 25).

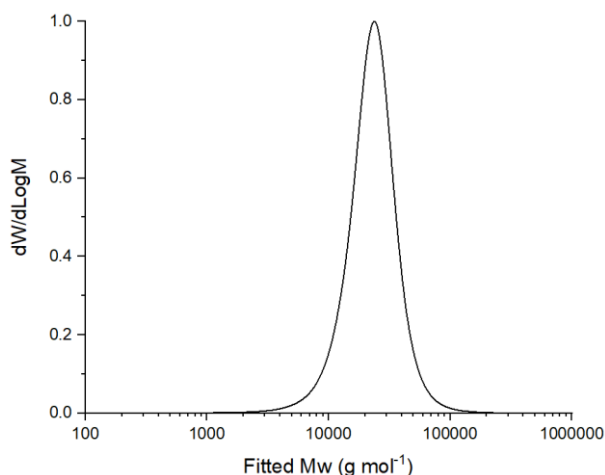


Figure 25: The SEC chromatogram pBA₁₀₀-b-BA₁₅-PEG-CTA ($M_n = 11,600 \text{ g mol}^{-1}$), ($\bar{D} = 1.41$)

The SEC chromatogram is broad, with a dispersity value of 1.41, indicating poor polymerisation control. This lack of control supports the hypothesis that radical movement between growing particles is vital for the production of low dispersity polymers. RAFT agents for use in emulsion should therefore feature solely hydrophilic R-groups as can be seen for Transurfs.

2.4.3 Improved RAFT Control of Methacrylate Monomers

Once established that emulsion conditions could improve the efficiency of a RAFT agent with acrylates, a further study was conducted on methacrylates. In this experiment, butyl methacrylate (BMA) was polymerised with PEG-CTA under emulsion conditions. The DLS spectra of the formed nanoparticles and the SEC chromatogram of their composite polymers are provided (Figure 26).

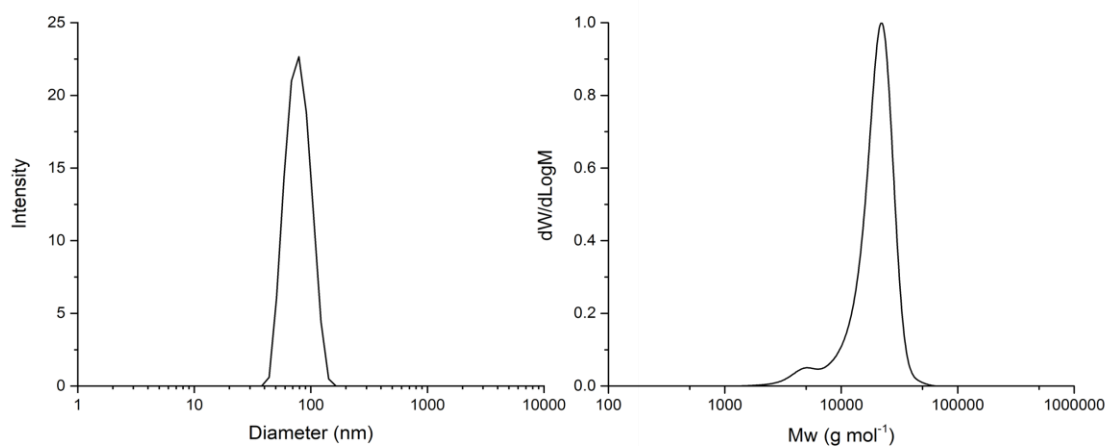


Figure 26: The DLS distribution (left) of pBMA₁₀₀ nanoparticles prepared with PEG-CTA and the correspondent SEC chromatogram (right) ($M_n = 18,900 \text{ g mol}^{-1}$), ($\bar{D} = 1.14$)

The DLS spectra shows uniform nanoparticles with a PDI of 0.05 and a Z-average of 75 nm. The SEC chromatogram displays one narrow dispersity peak ($M_w = 18,900$, $\bar{D} = 1.14$) with a slight lower molecular weight shoulder. The lower molecular weight shoulder aligns with the SEC for the starting PEG-CTA, suggesting a small fraction of unconsumed RAFT agent is present. The low dispersity value is somewhat surprising; as the R-group of PEG-CTA would not ordinarily be considered appropriate for the polymerisation of methacrylates, see Chapter 1 Section 1.4 for more details. To investigate this further, a solution polymerisation (dioxane) of BMA with PEG-CTA was conducted under identical conditions to the emulsion and the SEC recorded (Figure 27).

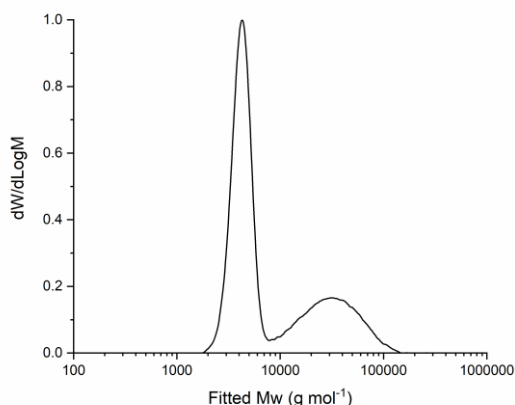


Figure 27: The SEC chromatogram of pBMA₁₀₀ produced with PEG-CTA in solution.

The SEC chromatogram for the solution polymerisation is bimodal, showing a very broad polymer peak with $\bar{D} > 2$. The lower molecular weight peak corresponds to the starting PEG-CTA, which appears to have been largely unconsumed during the polymerisation. The lack of RAFT agent incorporation, coupled with the broad molecular weight distribution strongly suggest that the PEG-CTA has not acted to control the polymerisation of BMA in solution. The improvement of RAFT efficiency gained in emulsion conditions is therefore essential to polymer control. To investigate this further, a kinetic study of both the emulsion and solution polymerisation of BMA was conducted. First, the molecular weight evolution with time was assessed by SEC (Figure 28).

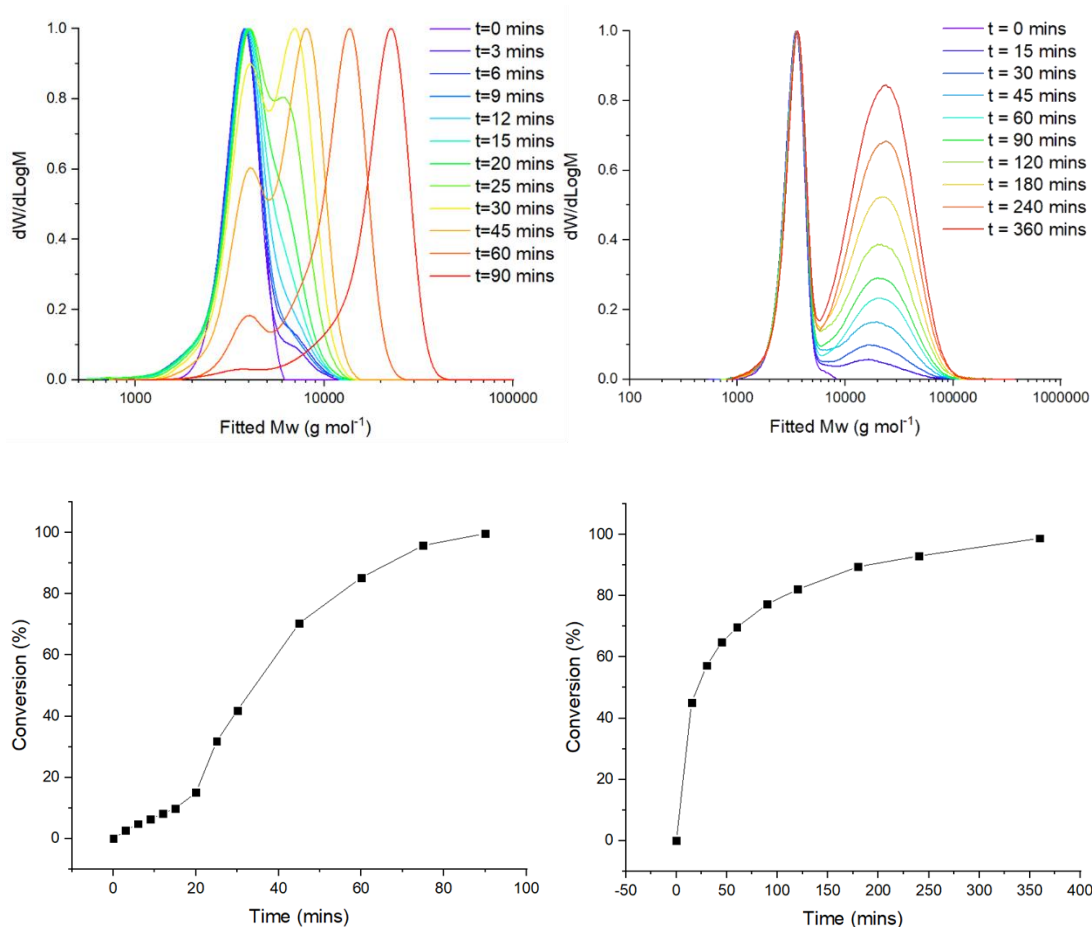


Figure 28: A kinetic overlay for the SEC traces (upper left) and conversion vs time data (lower left) for pBMA₁₀₀ prepared by emulsion polymerisation. A kinetic overlay for the SEC traces (upper right) and conversion vs time data (lower right) for pBMA₁₀₀ prepared by solution polymerisation. Note that different x-axis scales have been used for clarity

For the emulsion polymerisation, the SEC chromatograms show a rapid decrease in the peak intensity corresponding to the starting PEG-CTA and a gradual increase in polymer molecular weight with time. Both of these results

are consistent with rapid incorporation of PEG-CTA into the growing polymer chains and good RAFT control throughout. In comparison, the SEC chromatograms for the solution polymerisation show that the starting PEG-CTA is largely unconsumed. As well as this, the molecular weight of the polymer remains unchanged throughout the polymerisation, which, coupled with the broad dispersity, suggests free radical polymerisation has occurred. The consumption of PEG-CTA was quantified by deconvolution of the two SEC peaks as detected using a UV detector (309 nm) and plotted against monomer conversion (Figure 29).

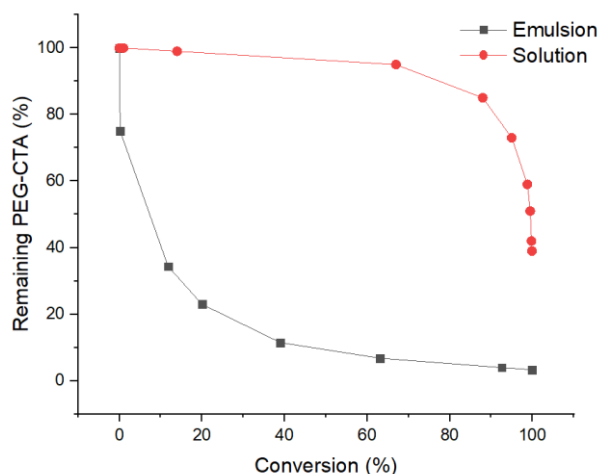


Figure 29: The percentage of remaining PEG-CTA vs monomer conversion for the emulsion (black) and solution (red) polymerisation of pBMA₁₀₀

Under emulsion conditions PEG-CTA is rapidly consumed even at low conversions (<2%). Rapid incorporation of PEG-CTA at such low conversions suggests that the system has a high chain transfer constant (C_T); consistent with the low dispersity of the final polymer. In contrast to this, in solution PEG-CTA is not consumed in any great amount until high conversions are reached (>90%). At high conversion, the monomer concentration drops relative to that of the RAFT agent; increasing the probability of chain transfer in accordance with Equation 4 *vide supra*. The lack of PEG-CTA incorporation in solution suggests a very low value for C_T under solution conditions. The number average molecular weight (M_n) polymers prepared in emulsion and solution

were also calculated by SEC and plotted against monomer conversion (Figure 30).

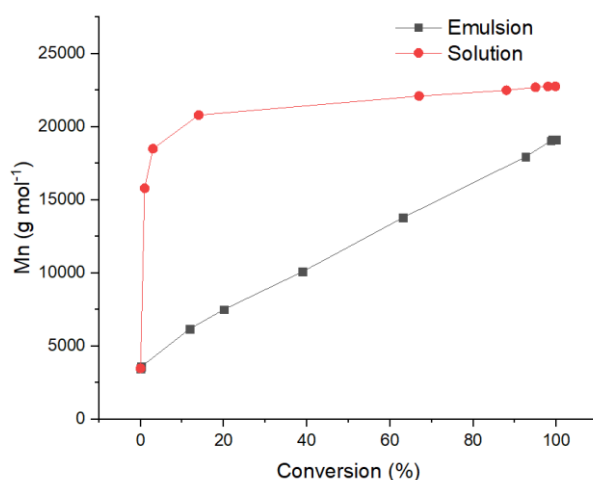


Figure 30: The number average molecular weight (M_n) of pBMA₁₀₀ prepared in emulsion (black) and solution (red) versus monomer conversion

Under emulsion conditions, the molecular weight increases linearly with conversion, a characteristic of controlled radical polymerisation, consistent with RAFT control. Under solution conditions however, the molecular weight increases very rapidly at low conversion before plateauing at a final value. The rapid increase in M_n occurs whilst monomer concentration is still high, indicative of a free radical polymerisation and again showing poor RAFT control. These results confirm that the improvement in RAFT control gained in emulsion conditions is crucial to controlling methacrylate polymerisation with PEG-CTA.

Once it had been established that the polymerisation of butyl methacrylate could be controlled by PEG-CTA, other methacrylate monomers of different hydrophobicities were next investigated. The emulsion polymerisation were carried out under the same conditions as for BMA. SEC was again used to characterise the polymer formed.

Table 3: A table showing the theoretical and experimentally determined, number average molecular weights (M_n) and dispersity values (\bar{D}) for a range of methacrylate monomers.

Monomer	DP	M_n SEC (Da)¹	M_n theo (Da)³	Diameter⁴
		/ \bar{D}²		(nm) / PDI⁵
Methyl methacrylate	100	9,000 / 1.10	12,312	56 / 0.03
Butyl methacrylate	100	19,000 / 1.14	16,520	75 / 0.05
Hexyl methacrylate	100	32,000 / 1.13	19,325	81 / 0.05
Decyl methacrylate	100	n/a	24,930	n/a
Lauryl methacrylate	100	n/a	27,741	n/a

1: Experimental number-average molar mass of the polymers determined by SEC-THF using a PMMA calibration system. 2: Dispersity of the polymer (M_w/M_n) as determined by SEC-THF. 3: M_n values calculated from the target DP assuming 100% conversion. 4: Intensity weighted average diameter as measured by dynamic light scattering. 5: Particle dispersity index calculated from dynamic light scattering.

The dispersity values calculated by SEC are very low, remaining below 1.15 for all polymers. There is also a good agreement between the theoretical number average molecular weight and the actual weight calculated by SEC for both MMA and BMA. However, the M_n value for HMA is considerably higher than expected; this is likely caused by a poor size comparison between the molecular size of pHMA verses the pMMA standards used for size determination. The low dispersity values coupled with the agreement between experimental and theoretical M_n values, show that the PEG-CTA has controlled the polymerisation well. Emulsion polymerisations of more hydrophobic monomers including decyl and lauryl methacrylate were attempted; however, very limited conversion (<2%) was observed in both cases. This lack of conversion is a consequence of the monomer solubility being effectively zero in water; preventing interaction with the water-soluble initiator at the beginning of the polymerisation. These experiments highlight a key

disadvantage of emulsion polymerisation in that it is unsuitable for ultra-hydrophobic monomers.

2.4.4 Chain Extensions

A widely utilised feature of RAFT is the ability to chain extend already formed polymers further to give di, tri and multiblock copolymers. To investigate if this was still achievable under emulsion conditions, pBMA₁₀₀ and pMMA₁₀₀ were chain extended *in situ* with MMA and BMA (DP = 100) respectively. The SEC chromatograms of the starting and final diblocks are shown below (Figure 31).

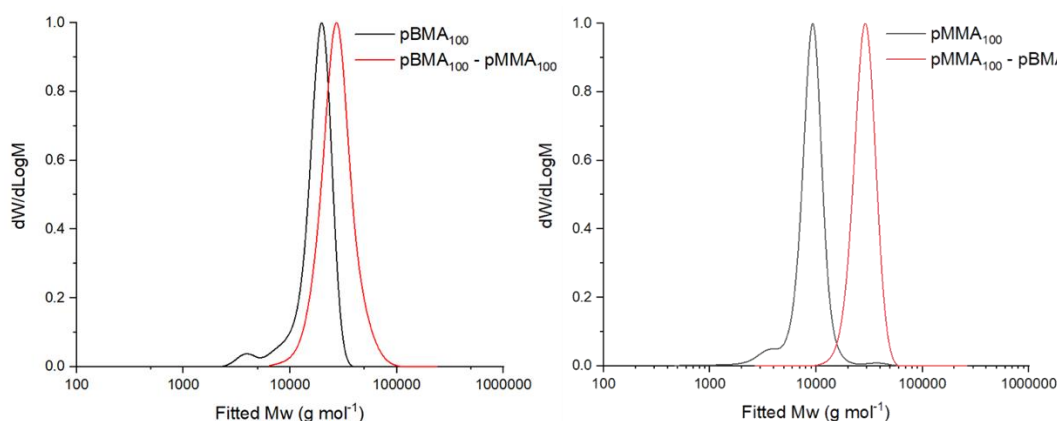


Figure 31: The SEC chromatogram for pBMA₁₀₀ (left, black) (M_n 18,900 g mol⁻¹, Đ = 1.14) chain extended with DP100 MMA (left, red) (M_n 28,500 g mol⁻¹, Đ = 1.15) and the SEC chromatogram for pMMA₁₀₀ (right, black) (M_n 9,500 g mol⁻¹, Đ = 1.11) chain extended with DP100 BMA (right, red) (M_n 28,500 g mol⁻¹, Đ = 1.15)

The final M_n (28,500 g mol⁻¹) for both diblocks matches each other as would be expected. The chromatograms also show that both the starting and final blocks have narrow dispersity (Đ < 1.15) indicating that the chain extensions have been well controlled. Furthermore, as can be clearly seen for pMMA₁₀₀ extended with BMA, there is no peak present corresponding to the first block in the second blocks chromatogram, suggesting quantitative chain extension. Following the successful synthesis of diblocks, multiblock copolymers were next attempted. The target multiblock, PBMA₁₀₀-*b*-(PBMA₂₀-*b*-(PHMA₂₀))₃, features a large first block to ensure maximal consumption of the initial PEG-CTA, followed by several smaller blocks. Each block was simply produced by

the addition of extra monomer and initiator without intermittent polymer purification. The SEC chromatogram for all blocks is provided below along with the tabulated data (Figure 32).

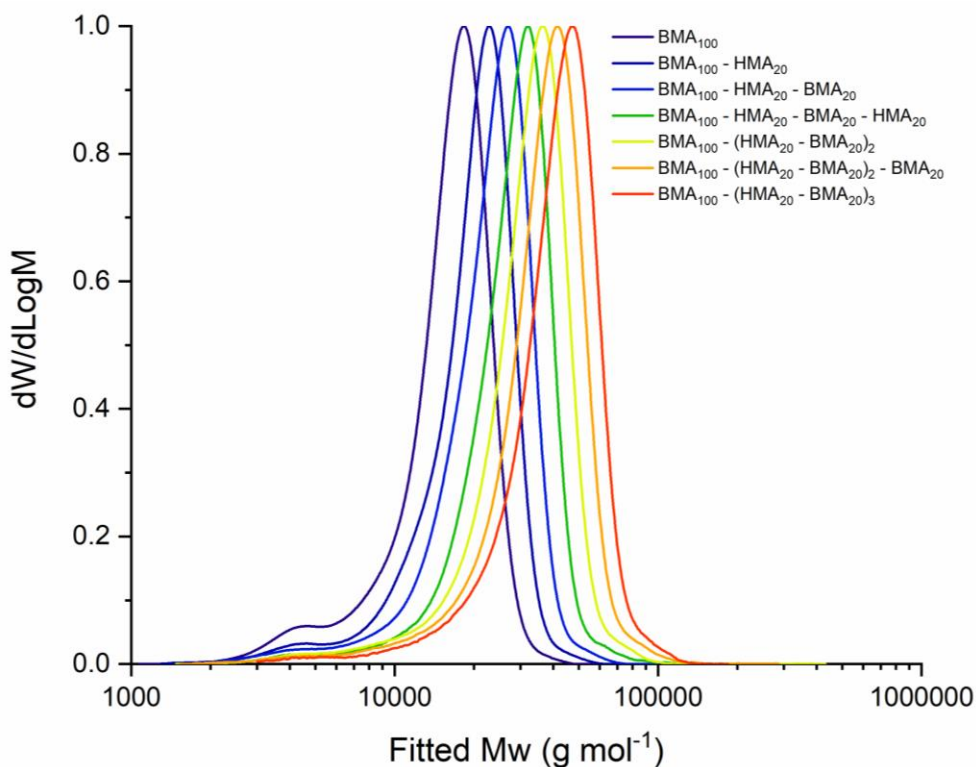


Figure 32: The SEC chromatograms for each block of an alternating BMA-HMA multiblock

Table 4: A table showing the theoretical and experimentally determined, number average molecular weights (M_n) and dispersity values (\mathfrak{D}) for an alternating BMA-HMA multiblock.

Monomer	DP	M_n SEC (Da) ¹ / \mathfrak{D}^2	M_n theo (Da) ³	Diameter ⁴ (nm) / PDI^5
Butyl methacrylate	100	16,500 / 1.07	16,520	77 / 0.05
Hexyl methacrylate	20	19,500 / 1.07	19,360	91 / 0.05
Butyl methacrylate	20	22,000 / 1.09	22,760	102 / 0.05
Hexyl methacrylate	20	25,000 / 1.13	25,600	115 / 0.06
Butyl methacrylate	20	28,000 / 1.14	29,080	129 / 0.07
Hexyl methacrylate	20	30,500 / 1.17	31,840	163 / 0.08
Butyl methacrylate	20	34,000 / 1.18	35,240	197 / 0.09

1: Experimental number-average molar mass of the polymers determined by SEC-THF using a PMMA calibration system. 2: Dispersity of the polymer (M_w/M_n) as determined by SEC-THF. 3: M_n values calculated from the target DP assuming 100% conversion. 4: Intensity weighted average diameter as measured by dynamic light scattering. 5: Particle dispersity index calculated from dynamic light scattering.

The SEC chromatograms show clear shifts in M_n with each successive block indicating successful chain extension. The dispersity values for all blocks remains low ($\bar{D} < 1.2$), however, it does increase with each chain extension performed. This increase in dispersity is likely due to the presence of polymer chains from earlier blocks that have terminate and hence not been extended. These so-called dead chains can be seen in the SEC chromatograms as a lower molecular weight tail. Despite this tailing, the overall low dispersity values indicate successful RAFT control throughout. The synthesis of this multiblock demonstrates the impressive extent to which RAFT control can be improved by use of emulsion conditions.

2.5 Conclusion

In this chapter, the theoretical effect of emulsion polymerisation on RAFT was explored and experimentally validated. It was shown that the in-built feeding mechanism of emulsion increased the control afforded over the polymerisation of both acrylates and methacrylates. In the case of methacrylates, this improvement in control was shown to be so significant that a RAFT agent offering no control in solution could produce low dispersity polymers in emulsion. Furthermore, these low dispersity polymers could be repeatedly chain extended with additional methacrylate monomer to form diblocks and multiblocks. This fine control over the polymer structure leads to the possibility of synthesising copolymer nanoparticles, allowing for potential tailoring of their physical properties.

2.6 References

1. M. Nomura, H. Kojima, M. Harada, W. Eguchi and S. Nagata, *Journal of Applied Polymer Science*, 1971, **15**, 675-691.
2. W. V. Smith and R. H. Ewart, *The Journal of Chemical Physics*, 1948, **16**, 592-599.
3. M. Harada, M. Nomura, H. Kojima, W. Eguchi and S. Nagata, *Journal of Applied Polymer Science*, 1972, **16**, 811-833.
4. C. Capello, U. Fischer and K. Hungerbühler, *Green Chemistry*, 2007, **9**, 927-934.
5. C. A. Angell, W. J. Sichina and M. Oguni, *The Journal of Physical Chemistry*, 1982, **86**, 998-1002.
6. S. Fan, S. P. Gretton-Watson, J. H. G. Steinke and E. Alpay, *Chemical Engineering Science*, 2003, **58**, 2479-2490.
7. S. Sajjadi and F. Jahanzad, *Chemical Engineering Science*, 2006, **61**, 3001-3008.
8. D. A. Shipp, *Polymer Reviews*, 2011, **51**, 99-103.
9. R. B. Grubbs, *Polymer Reviews*, 2011, **51**, 104-137.
10. K. Matyjaszewski and J. Xia, *Chemical Reviews*, 2001, **101**, 2921-2990.
11. S. Perrier, *Macromolecules*, 2017, **50**, 7433-7447.
12. E. Groison, S. Brusseau, F. D'Agosto, S. Magnet, R. Inoubli, L. Couvreur and B. Charleux, *ACS Macro Letters*, 2012, **1**, 47-51.
13. J. Qiu, S. G. Gaynor and K. Matyjaszewski, *Macromolecules*, 1999, **32**, 2872-2875.
14. C. J. Ferguson, R. J. Hughes, D. Nguyen, B. T. T. Pham, R. G. Gilbert, A. K. Serelis, C. H. Such and B. S. Hawckett, *Macromolecules*, 2005, **38**, 2191-2204.
15. R. T. A. Mayadunne, E. Rizzardo, J. Chiefari, J. Krstina, G. Moad, A. Postma and S. H. Thang, *Macromolecules*, 2000, **33**, 243-245.
16. R. T. A. Mayadunne, E. Rizzardo, J. Chiefari, Y. K. Chong, G. Moad and S. H. Thang, *Macromolecules*, 1999, **32**, 6977-6980.
17. C. Barner-Kowollik, M. Buback, B. Charleux, M. L. Coote, M. Drache, T. Fukuda, A. Goto, B. Klumperman, A. B. Lowe, J. B. McLeary, G. Moad, M. J. Monteiro, R. D. Sanderson, M. P. Tonge and P. Vana, *Journal of Polymer Science Part A: Polymer Chemistry*, 2006, **44**, 5809-5831.
18. M. H. Stenzel, L. Cummins, G. E. Roberts, T. P. Davis, P. Vana and C. Barner-Kowollik, *Macromolecular Chemistry and Physics*, 2003, **204**, 1160-1168.
19. D. Charmot, P. Corpart, H. Adam, S. Z. Zard, T. Biadatti and G. Bouhadir, *Macromolecular Symposia*, 2000, **150**, 23-32.
20. M. J. Monteiro and J. de Barbeyrac, *Macromolecules*, 2001, **34**, 4416-4423.

21. M. J. Monteiro, M. Hodgson and H. De Brouwer, *Journal of Polymer Science Part A: Polymer Chemistry*, 2000, **38**, 3864-3874.
22. S. W. Prescott, M. J. Ballard, E. Rizzardo and R. G. Gilbert, *Macromolecules*, 2002, **35**, 5417-5425.
23. I. Uzulina, S. Kanagasabapathy and J. Claverie, *Macromolecular Symposia*, 2000, **150**, 33-38.
24. P. Gurnani, A. M. Lunn and S. Perrier, *Polymer*, 2016, **106**, 229-237.
25. G. Moad, J. Chiefari, Y. K. Chong, J. Krstina, R. T. A. Mayadunne, A. Postma, E. Rizzardo and S. H. Thang, *Polymer International*, 2000, **49**, 993-1001.
26. E. V. Chernikova and E. V. Sivtsov, *Polymer Science, Series B*, 2017, **59**, 117-146.
27. X. Sun, Y. Luo, R. Wang, B.-G. Li and S. Zhu, *AIChE Journal*, 2008, **54**, 1073-1087.
28. F. Vidal, J. Guillot and A. Guyot, *Colloid and Polymer Science*, 1995, **273**, 999-1007.
29. M. C. A. Stuart, J. C. van de Pas and J. B. F. N. Engberts, *Journal of Physical Organic Chemistry*, 2005, **18**, 929-934.
30. S. Garnier and A. Laschewsky, *Langmuir*, 2006, **22**, 4044-4053.
31. S. Creutz, J. van Stam, F. C. De Schryver and R. Jérôme, *Macromolecules*, 1998, **31**, 681-689.
32. A. H. E. Mueller, D. Yan, G. Litvinenko, R. Zhuang and H. Dong, *Macromolecules*, 1995, **28**, 7335-7338.

3 Synthesis and Characterisation of pH Responsive Nanoparticles

3.1 Overview

Polymeric nanoparticles can be prepared in water *via* emulsion polymerisation as previously discussed (Chapter 1 Section 1.4.2). In this chapter, emulsion polymerisation is used to prepare a range of pH responsive nanoparticles.

3.2 Introduction

3.2.1 Stimuli Responsive Nanoparticles

Responsive nanoparticles are ones that can undergo physical transformation under specific conditions. These transformations can be mild such as swelling or shrinking, or they can be more significant such as changes in shape or even complete disassembly¹. Stimuli responsive nanoparticles are an important subset of these in which the morphological change can be purposefully triggered via one or more external stimuli² including; temperature, light, redox agents and pH as discussed in the following sections³.

3.2.1.1 Temperature Responsive Polymers

A number of polymers have been reported to exhibit unusual insolubility in water at elevated temperatures. The best known example of such a polymer is poly(N-isopropyl acrylamide) or p(NIPAM)⁴⁻⁶. Whilst soluble in water at room temperature, p(NIPAM) precipitates from solution at temperatures above 32 °C⁷; a point termed its Lower Critical Solution Temperature (LCST). Incorporation of monomers with an LCST into a polymer, allows for the formation of nanoparticles that can rapidly respond to temperature⁸. As the temperature change is causing the polymers to desolvate, this group of responsive nanoparticles typically undergo size or shape transitions with temperature. A temperature responsive system capable of shape transition was

developed by Armes *et al.* in 2012⁹. Upon a decrease in temperature from 21 °C to 4 °C these particles reversibly transition from cylindrical worm-like structures to smaller discrete spheres. The particles comprised of a diblock copolymer of glycerol methacrylate (GMA) (DP = 54) and 2-hydroxypropyl methacrylate (HPMA) (DP = 140), prepared by RAFT dispersion polymerisation (Section 1.1.4.3 for more details).

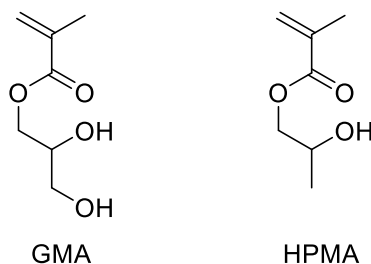


Figure 33: The chemical structures of glycerol methacrylate (GMA) and 2-hydroxypropyl methacrylate (HPMA).

The authors probed the molecular origin of this transition *via* variable temperature NMR in D₂O. The NMR peaks corresponding to HPMA increase in intensity as temperature is decreased suggesting a greater degree of core solvation. The authors propose that this increased solvation gives rise to greater chain flexibility allowing for a transition to spheres. As well as NMR spectra of the polymers, the size of the particles themselves was also monitored by DLS. The results of these measurements show that the transition from worms to spheres does not occur sharply at one specific temperature but is instead occurring slowly from 15 °C downwards.

3.2.1.2 UV Responsive Polymers

UV responsive polymers are gaining growing interest due to the ease with which their stimulus (UV light) can be controlled and localised, allowing for so-called "remote-controlled polymers"¹⁰. A popular moiety for UV-responsive polymers is the *o*-nitrobenzyl ether group¹¹, its structure and UV-response are shown below (Figure 34)¹².

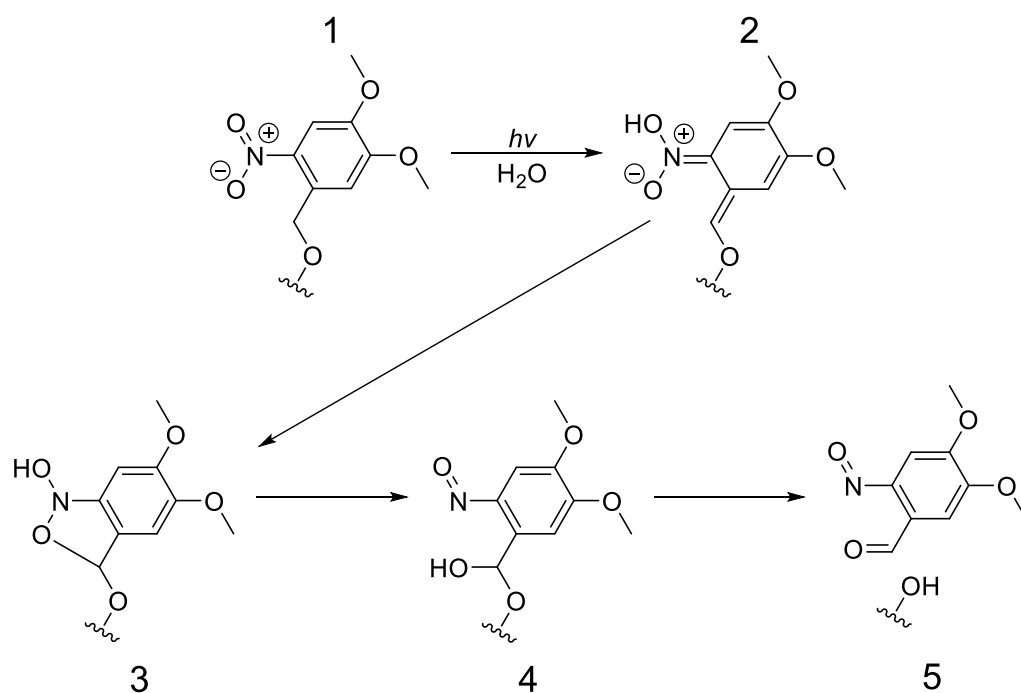


Figure 34: The structure and UV response of *o*-nitrobenzyl ether group adapted from Wirz *et al.*¹²

Upon exposure to UV-light (350 – 280 nm), the *o*-nitrobenzyl ether undergoes first an electronic rearrangement followed by cyclisation to intermediate 3. This intermediate then further rearranges to the acetal species 4. Finally, the acetal species collapses, cleaving the ether bond and its attached substituent.

The *o*-nitrobenzyl ether was utilised by Almutairi *et al.* as the trigger for their self-immolating polymers¹³. In their work, monomers containing *o*-nitrobenzyl ether pendent groups were used to trigger a cascade of reactions, degrading first the polymer side, and then main, chains (Figure 35).

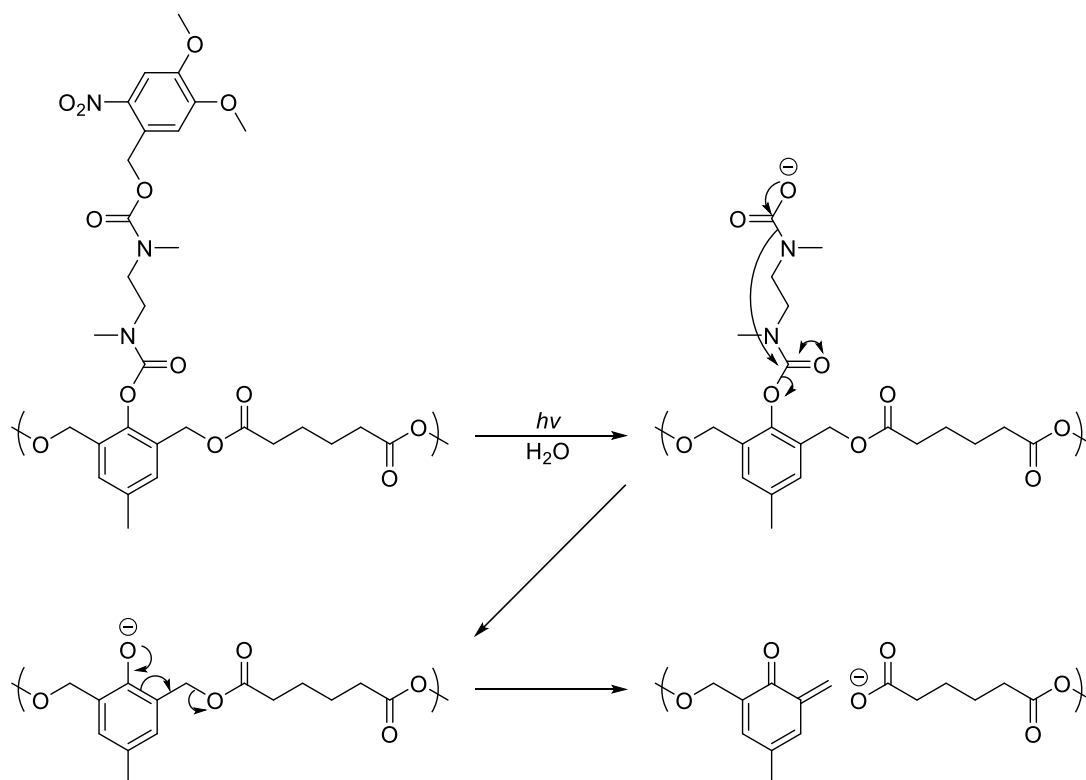


Figure 35: The self-immolation mechanism of polymers triggered by the UV cleavage of *o*-nitrobenzyl ether groups, adapted from a manuscript by Almutairi *et al.*¹³

The authors then went further and used nanoprecipitation to prepare nanoparticles from their UV-responsive polymers. Nile red release studies performed on these particles showed that they were capable of rapid disintegration into their component parts upon exposure to UV light for less than one minute. An important consideration when using such systems is the nature of all components formed; the aromatic aldehyde obtained from the *o*-[nitrobenzyl ether cleavage in particular has been shown to be cytotoxic¹⁴ and is a suspected mutagen¹⁵.

3.2.1.3 Redox Responsive Polymers

Redox responsive polymers are ones which can not only be oxidized or reduced, but in some way change their structure because of it. Many polymers are formally redox responsive in the broad sense that they can be degraded by intense oxidative cleavage of the side chains and backbone¹⁶. Generally, though the term is limited to polymers that can be easily and practically

oxidized or reduced. As well as full degradation, redox responsive nanoparticles, such as those designed by Hubbell *et al.*, have been shown to be capable of morphological transformations; in this case vesicle to worm to micelle, upon oxidation¹⁷. In their paper, an ABA triblock of poly(ethylene glycol)₁₆ (A) and poly(propylene sulphide)₅₀ (B) was prepared via the anionic ring opening polymerisation of methyl thiirane using a PEG macro-initiator and end capping agent. This triblock was then shown to self-assemble into stable vesicle structures with diameters ranging from 200 – 500 nm. Upon exposure to oxidizers, in this case 0.03 v% H₂O₂, the sulphide groups within the vesicle are oxidized; first to a sulfoxides and then ultimately sulfones (Figure 36). The oxidation of the p(propylene sulfide) increases the hydrophilicity of the vesicles central block resulting in a morphological change to lower packing order structures; first worms then micelles. In comparison to the other stimuli responsive systems discussed in this section, the rate at which redox responsive nanoparticles undergo their transitions can be very slow. Hubbell *et al.* go further in their paper and show that the rate of transition is proportionate to the concentration of oxidant (H₂O₂) used, allowing for temporal control of the transition over a vast 100 hour range.

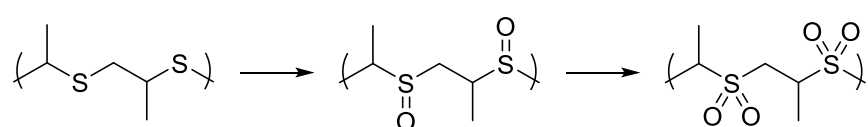


Figure 36: A scheme showing the oxidation of p(propylene sulphide) adapted from a manuscript by Hubbell *et al.*¹⁷

3.2.1.4 pH Responsive Polymers

pH responsive polymers are ones featuring acidic or basic groups, the charge state of which can be varied with pH¹⁸. This change in charge can lead to a wide variety of responses in nanoparticles including changes to size and shape such as those described below.

Janus nanoparticles featuring hydrophobic polystyrene and pH responsive poly(acrylic acid) portions were prepared by Lee *et al.* via a seeded emulsion polymerisation¹⁹. The carboxylic acid moieties of acrylic acid can be fully deprotonated at high pH (pH > 11); conversely at low pH values (pH < 2) they are almost fully protonated. This change in protonation state radically alters the hydrophilicity of the poly(acrylic acid) portion of the Janus nanoparticles at different pH values. Decreasing the solution pH, results in a contraction of the increasingly hydrophobic poly(acrylic acid) portion of the nanoparticles; ultimately resulting in the formation of asymmetric shrunken particles (Figure 37). Conversely, at high pH, TEM imaging shows that the poly(acrylic acid) portion of the nanoparticle swells significantly giving, what the authors describe as, a dumbbell shape.

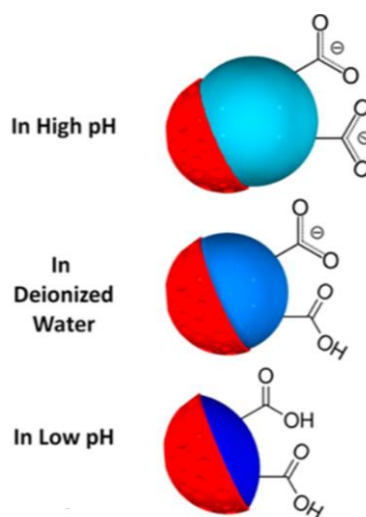


Figure 37: A figure from Lee *et al.*¹⁹ graphically depicting the changes in morphology with pH of Janus nanoparticles featuring a pH responsive poly(acrylic acid) block.

It is noted in the paper that the morphological transformation under basic conditions is far greater than under acid conditions. Increased swelling at high pH is reasoned as being a consequence of electrostatic repulsions between the anionic carboxylate groups of poly(acrylic acid). This observation highlights that when designing pH responsive polymer systems, both charge and changes to polymer hydrophilicity need to be carefully considered.

Of the different forms of responsive polymers discussed, pH responsiveness nanoparticles are perhaps the most chemically diverse and are explored further in the next section.

3.2.2 pH responsive Nanoparticles

pH responsive polymers can respond both reversibly and irreversibly to either acidic or basic stimuli. This wide range of behaviours is summarised in

Table 5 below.

Table 5: A list of literature examples of pH responsive monomers, their pH of change and their response.

Functionality	Monomer	Response pH ¹	Author <i>et al.</i>
Sulfonic acid	4-styrene sulfonic acid	<2 (-ve to 0)	Armes ²⁰
Phosphoric acid	Vinyl phosphoric acid	<2.5 (-ve to 0)	Wegner ²¹
Carboxylic acid	Acrylic acid	<4 (-ve to 0)	Leroux ²²
Ketal	Solketal methacrylate	<5 (hydrolysis)	Abetz ²³
Hydrozone	Acroyl hydrazide derivatives	<5.5 (hydrolysis)	Fernandez-Trillo ²⁴
Boronic ester	Vinyl phenyl boronic acid derivatives	>5 (hydrolysis)	Zhang ²⁵
Pyridine	4-Vinyl pyridine	>5 (+ve to 0)	Li ²⁶
Tertiary amine	2-(Diethylamino) ethyl methacrylate	>6.5 (+ve to 0)	Zhao ²⁷
Primary amine	N-(3-aminopropyl) methacrylamide	>9 (+ve to 0)	Stöver ²⁸
Guanidinium	Guanidinium ethyl acrylamide	>12 (+ve to 0)	Mahmoudi ²⁹

1: The pH at which the nanoparticles were observed to respond and the nature of the response.

As shown in

Table 5, pH responsive polymers can respond over a wide range of pH values. Copolymerisation of more than one responsive monomer, allows for the preparation of nanoparticles that respond at two distinct pH points. An example of this are the poorly termed “schizophrenic” polymers, featuring both an acidic and basic block, allowing them to respond to pH changes above and below pH 7³⁰. Copolymerisation of similarly responsive monomers, instead allows for the pH of response to be tuned somewhere between their values as demonstrated by Schubert *et al.*³¹. Whilst a seemingly facile way of tailoring the pH response, surprisingly little research has been carried out on such copolymer nanoparticles.

3.2.3 Objectives

The objectives of this chapter are to prepare nanoparticles from copolymers of pH responsive monomers and to investigate what factors affect their pH of response. It is hoped that this study will shed light on the parameters affecting responsiveness and allow for improved pH responsive nanoparticle design. Factors that will be investigated are; the ratio of responsive monomers to each other, the overall polymer hydrophobicity and molecular weight, as well as the solution temperature and salt concentration.

3.3 Experimental

3.3.1 Materials

Monomers; diisopropylaminoethyl methacrylate (DPAEMA), diethylaminoethyl methacrylate (DEAEMA), butyl methacrylate (BMA) and methyl methacrylate (MMA) were purchased from Sigma Aldrich and passed through a short aluminium oxide column to remove inhibitor prior to use. The initiator 2,2'-azobis[N-(2-carboxyethyl)-2-methylpropionamide] tetrahydrate (VA-057),

was purchased from Wako chemicals and used as provided. The distilled water was prepared on site.

3.3.2 Analytical Techniques

3.3.2.1 Size Exclusion Chromatography

SEC was performed on an Agilent Infinity II MDS instrument equipped with differential refractive index (DRI) and multiple wavelength UV detectors, one of which is set to 309 nm. The column used for separation is a PLgel Mixed C columns (300 x 7.5 mm) and a PLgel 5 μm guard column. The eluent is THF with 2 % triethylamine (TEA) and 0.01 % butylated hydroxytoluene (BHT) additives. Samples were run at 1ml/min at 30 °C. Poly(methyl methacrylate) (pMMA) (2000 – 1,500,000 g mol⁻¹) and polystyrene standards (Agilent EasyVials) were used for calibration, analysis was carried out compared to the pMMA standards. Analyte samples were filtered through a GVHP membrane with 0.22 μm pore size before injection. Experimental molar mass (M_n , SEC) and dispersity (\mathcal{D}) values of synthesized polymers were determined by conventional calibration using Agilent GPC/SEC software.

3.3.2.2 Dynamic Light Scattering

Samples were prepared by diluting nanoparticle latexes 1000-fold with DI water to a final concentration of 0.2 mg/mL. DLS measurements were performed on a MALVERN Zetasizer Nano ZS operating at 25 °C with a 4 mW He-Ne 633 nm laser module. Measurements were made in back scattering mode at an angle of 173°. Measurements were performed in triplicate with automatic attenuation selection and measurement position. The results were analysed using Malvern DTS 6.20 software.

3.3.2.3 Zeta Potential Measurements

Samples were prepared by diluting nanoparticle latexes 1000-fold with DI water to a final concentration of 0.2 mg/mL. Zeta potential measurements were performed on a MALVERN Zetasizer Nano ZS operating at 25 °C with a 4 mW

He-Ne 633 nm laser module. Measurements were made in a Malvern DTS-1070 zeta cuvette under back scattering mode at an angle of 173°. Measurements were performed in triplicate with automatic attenuation selection and measurement position. The results were analysed using Malvern DTS 6.20 software.

3.3.2.4 Ultraviolet-Visible Turbidity Measurements

UV-vis turbidity measurements were performed on a Beckman DU640 instrument at 25 °C using a laser set at a wavelength of 600 nm. A quartz cuvette with a path length of 1 cm was used for all measurements. The sample concentration was fixed at 100 mg/mL. Measurements were performed with automatic attenuation selection.

3.3.2.5 Transmission Electron Microscopy

Samples were prepared by diluting nanoparticle latexes 1000-fold with DI water. A droplet of this dilute nanoparticle solution was placed on a TEM cover slip. A TEM grid (graphene oxide) was then floated on the surface of this droplet for 1 minute before being removed and left to dry overnight. The sample was then imaged on a JEOL 2100FX electron microscope at an acceleration voltage of 200 kV.

3.3.2.6 Solution pH Measurements

100 µL of nanoparticle latex was diluted with 100 mL of DI water and a 1.5 mL aliquot removed for size measurement by DLS. The pH of the solution was measured using a Fisherbrand AE150 benchtop pH meter. The pH of the solution was then reduced by approximately 0.5 units by careful addition of dilute HCl (0.1 M), before a second 1.5 mL aliquot was taken for measuring. This process was repeated until samples had been collected at intervals over the range of pH 9 – 2.

3.3.3 Synthetic Procedures

3.3.3.1 PEG-CTA Synthesis

CTA-acid (1.37 g, 3 equiv, 3.76 mmol) was dissolved in 2.813 mL of an oxalyl chloride DCM solution (2 M) (4.5 equiv, 5.64 mmol) to yield a bright yellow solution. Three drops of anhydrous DMF were added to this solution, resulting in rapid gas generation and a change in colour to orange. After effervescence had stopped, the solution was sealed and gently stirred at room temperature for 1 h. Separately, 2.5 g of 2k MeO-PEG-OH (1 equiv, 1.25 mmol) was dissolved in 10 mL of DCM; this was then added to the reaction and left stirring overnight to yield a dark yellow solution. The product was then obtained by precipitating this solution into an 80:20 mix of hexane and diethyl ether, followed by drying overnight at 40 °C under vacuum to afford a pale yellow powder (yield = 2.63 g 89%). ¹H NMR (CHCl₃, 300 MHz) δ 4.27 2H COOCH₂CH₂O t 6 Hz, 3.89 2H COOCH₂CH₂O t 6 Hz, 3.66 176H (OCH₂CH₂)₄₄ m, 3.40 3H OCH₂CH₂OCH₃ s, 3.28 2H SCSSCH₂CH₂ t 5 Hz, 1.71 6H S(CH₃)₂CCOOCH₂ s J, 1.65 2H SCSSCH₂CH₂ tt 5.2 Hz, 1.27 18H SCSSCH₂CH₂(CH₂)₉CH₃ m, 0.90 3H CH₂CH₂CH₃ t 9 Hz. MS [M + Na⁺] calculated as 2369.2 found as 2368.9.

3.3.3.2 Nanoparticle Synthesis

A general procedure for the nanoparticles synthesised in this chapter is as follows; 102.2 mg PEG-CTA (1 eq, 0.046 mmol) was dissolved in 5 mL of deionised water in a 20 mL glass vial, 1.08 mL DPAEMA (973 mg, 100 eq, 4.57 mmol) and 0.253 mL of a VA-057 stock solution (0.01 g/mL H₂O) (2.53 mg 0.125 eq, 0.00610 mmol) were then added to the reaction. The vial was then sealed and briefly vortexed before purging with nitrogen gas for 15 min. The reaction was then heated to 70 °C and stirred at 500 RPM for 90 minutes to form a white latex. For all other polymerizations targeting a degree of polymerization (DP) of 100, the amount of PEG-ester CTA, water and VA-057

stock solution was kept constant and the amount of monomer varied to give the same molar ratios. When targeting polymers of various DP, the ratio of PEG-ester CTA to VA-057 was kept constant and the amount of monomer varied with respect to the CTA.

3.4 Results and Discussion

3.4.1 Responsive Particle Synthesis

Nanoparticles were prepared via RAFT emulsion polymerisation using PEG-CTA as the chain transfer agent, allowing for both excellent control over the methacrylate monomers used ($\mathcal{D} \geq 1.15$) and the overall nanoparticle size.

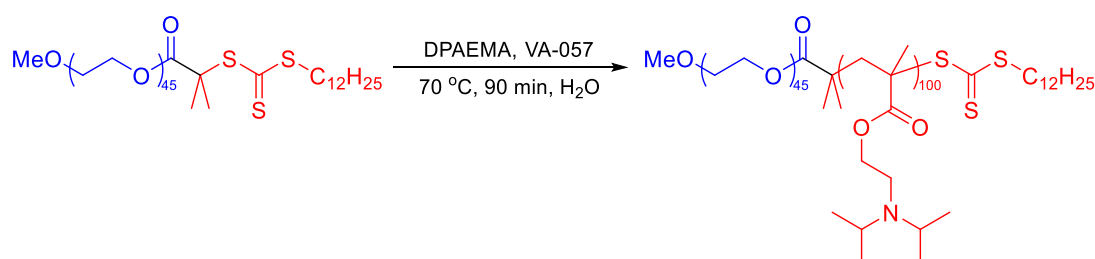


Figure 38: The reaction scheme for the polymerisation of DPAEMA with PEG-CTA, hydrophilic and hydrophobic groups are highlighted in blue and red respectively

A Library of 15 nanoparticles were prepared in order to assess the factors affecting pH responsiveness and the results summarised in the table below.

Table 6: A summary of all nanoparticles and their composite polymers prepared in this chapter along with their pH of disassembly.

Code	Polymer ¹	M_n SEC (Da) ² / \mathcal{D} ³	M_n theo (Da) ⁴	Diameter (nm) ⁵ / \mathcal{PDI} ⁶	pH of Disassembly ⁷
D1	pDPAEMA ₁₀₀	34,200 / 1.18	22,330	107 / 0.03	4.7 ± 0.08
D2	pDPAEMA ₇₅ – DEAEMA ₂₅	33,400 / 1.18	22,627	105 / 0.02	6.4 ± 0.03
D3	pDPAEMA ₅₀ – DEAEMA ₅₀	31,800 / 1.17	21,925	103 / 0.05	6.5 ± 0.06

D4	pDPAEMA ₂₅ – DEAEMA ₇₅	29,900 / 1.15	21,223	104 / 0.04	6.8 ± 0.05
D5	pDEAEMA ₁₀₀	28,400 / 1.14	20,520	102 / 0.02	7.3 ± 0.02
B1	pDPAEMA ₇₅ – BMA ₂₅	26,500 / 1.17	21,553	100 / 0.05	4.3 ± 0.07
B2	pDPAEMA ₅₀ – BMA ₅₀	20,800 / 1.16	19,765	96 / 0.09	3.9 ± 0.15
B3	pDPAEMA ₂₅ – BMA ₇₅	18,900 / 1.15	17,983	82 / 0.06	n/a
B4	pBMA ₁₀₀	16,400 / 1.13	16,200	74 / 0.05	n/a
M1	pDPAEMA ₇₅ – MMA ₂₅	23,400 / 1.15	20,500	98 / 0.04	4.6 ± 0.08
M2	pDPAEMA ₅₀ – MMA ₅₀	18,600 / 1.14	17,670	86 / 0.08	4.4 ± 0.13
M3	pDPAEMA ₂₅ – MMA ₇₅	15,100 / 1.12	14,840	73 / 0.07	4.1 ± 0.19
M4	pMMA ₁₀₀	12,100 / 1.10	12,010	60 / 0.04	n/a
L1	pDPAEMA ₅₀	17,900 / 1.15	12,665	93 / 0.05	5.1 ± 0.02
L2	pDPAEMA ₂₅ – BMA ₂₅	11,600 / 1.17	10,887	84 / 0.06	4.4 ± 0.06

1: Polymer composition of the particles core-forming block, excluding PEG₄₅ 2: Experimental number-average molar mass of the polymers determined by SEC-THF using a PMMA calibration system. 3: Dispersity of the polymer (M_w/M_n) as determined by SEC-THF. 4: M_n values calculated from the target DP assuming 100% conversion. 5: Intensity weighted average diameter as measured by dynamic light scattering. 6: Particle dispersity index calculated from dynamic light scattering. 7: Average value for pH between the last assembled and first

disassembled points as determined by DLS size, errors are half the difference between said points.

As can be seen in **Table 6**, the dispersity (\mathcal{D}) of all polymers remains below 1.2, indicating good control. However, it is noticeable that polymers with higher DPAEMA content do have broader dispersities than for BMA or MMA. In addition, there is a large disagreement between experimental and actual M_n values for these polymers; 34,200 Da versus 22,330 Da for pDPAEMA₁₀₀ (D1) for example. A part of this disagreement can be explained by the poor size agreement between pDPAEMA and the pMMA standards used. Examination of the SEC chromatograms for experiments D1 and B4, homopolymers of DPAEMA and BMA respectively, reveals a higher molecular weight shoulder for D1 not visible for B4 (Figure 39). This shoulder would be expected to broaden the polymer dispersity as well as also increasing molecular weight.

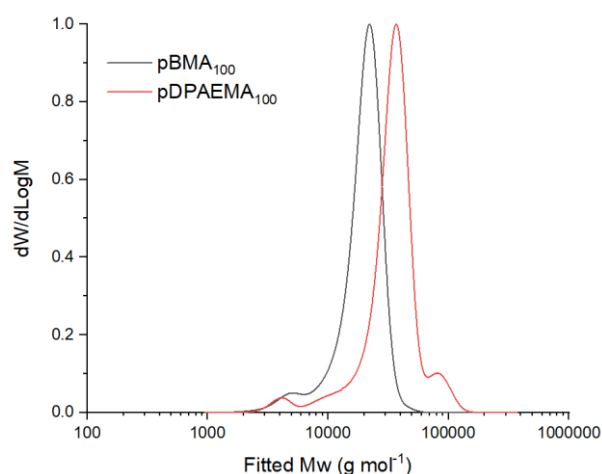


Figure 39: An overlay of the SEC chromatograms of pBMA₁₀₀ (grey) ($M_n = 14,500 \text{ g mol}^{-1}$), ($\mathcal{D} = 1.13$) and pDPAEMA₁₀₀ (red) ($M_n = 34,200 \text{ g mol}^{-1}$), ($\mathcal{D} = 1.18$), note the low molecular weight peak corresponds to the starting PEG-CTA. The origin of the high molecular weight shoulder observed for pDPAEMA₁₀₀ (red) is discussed below.

High molecular weight shoulders are usually attributed to one of two things, bimolecular termination³² and branching³³. Bimolecular termination involves two growing polymer chain ends reacting with each other, yielding a polymer of double the molecular weight. Steric hindrance around the growing chain end of methacrylate polymers usually disfavors bimolecular termination³⁴.

Furthermore, if it were to occur for growing DPAEMA chains then it would also be expected for growing BMA chains. The lack of any high molecular weight shoulder, as well as methacrylate polymers normal aversion to bimolecular weight termination, means that this theory can be discounted. Branching is well documented for acrylate polymerisations³⁵ and involves the abstraction of a proton from the polymer backbone; leaving behind a radical which then initiates a side polymer. For methacrylates however, there are no abstractable protons in the polymer backbone, which would seemingly disprove this theory as well. However, there may be protons that can be abstract from the side groups as shown below (Figure 40).

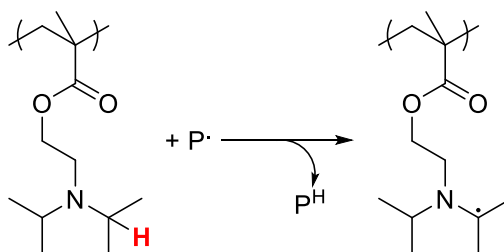


Figure 40: Chemical structure of pDPAEMA with the abstractable proton shown (bold red) as well as the radical product formed

Abstraction of the proton shown in Figure 40, would lead to the formation of a tertiary carbon centre radical stabilised by both hyperconjugation and interaction with the lone pair of the adjacent nitrogen atom. Whilst predicted to be less stable than a methacrylate-propagating radical, the difference may be sufficiently small for the abstraction still to occur. Importantly, no comparable hydrogen exists for BMA, so its abstraction and consequent polymer branching would occur for DPAEMA exclusively as is seen in (Figure 39). To test if the abstraction was possible, an experiment was conducted wherein MMA was polymerised by free radical polymerisation in the presence of DIPEA, which mimics the side chain of DPAEMA. By varying the concentration of DIPEA and measuring the molecular weight of MMA formed after a fixed time, a Mayo plot could be constructed (Figure 41).

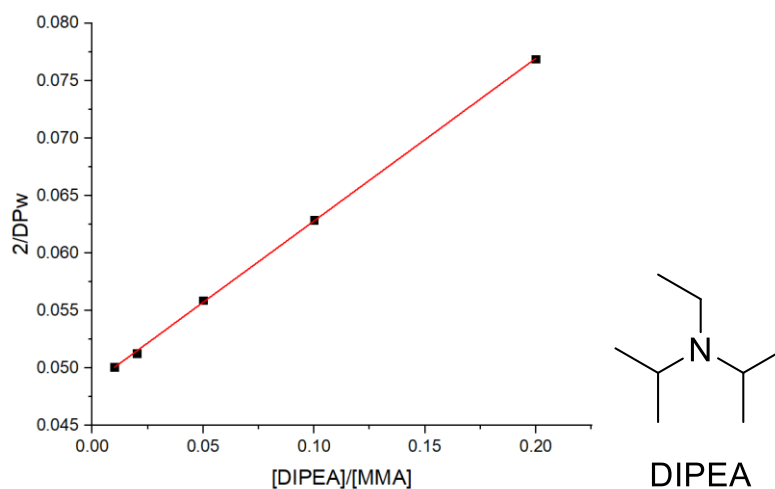


Figure 41: A Mayo plot constructed from the polymerisation of MMA in the presence of variable amounts of DIPEA, equation of the trendline (red) is $Y = 0.141X + 0.0486$ (left). The chemical structure of DIPEA used (right).

The Mayo plot constructed shows that there is a clear inverse relationship between DIPEA concentration and final molecular weight, as would be expected for an irreversible chain transfer agent. This relationship shows that the hydrogen on DIPEA and hence DPAEMA is abstractable and would allow branching to occur. However, it should be noted that the chain transfer constant (C_T) calculated from the slope of the trendline is 0.141, 2 orders of magnitude smaller than for PEG-CTA; explaining why only minimal branching and increases in polymer dispersity are observed.

The diameter of all nanoparticles prepared was measured using Dynamic Light Scattering (DLS). This technique utilises the scattered light from particles to calculate their diffusion coefficient in solution, this can then be used to infer their diameters (d) via the modified Stokes-Einstein equation below.

$$d = \frac{k_B T}{6\pi\mu D}$$

Where d is the particle diameter, D is the diffusion coefficient calculated and k_b , T and μ are the Boltzmann constant, temperature and solvent viscosity respectively. Importantly, as alluded to by the π term present, the equation

assumes that all particles are of a spherical morphology; transmission electron microscopy (TEM) was used to image the particles and confirm this.

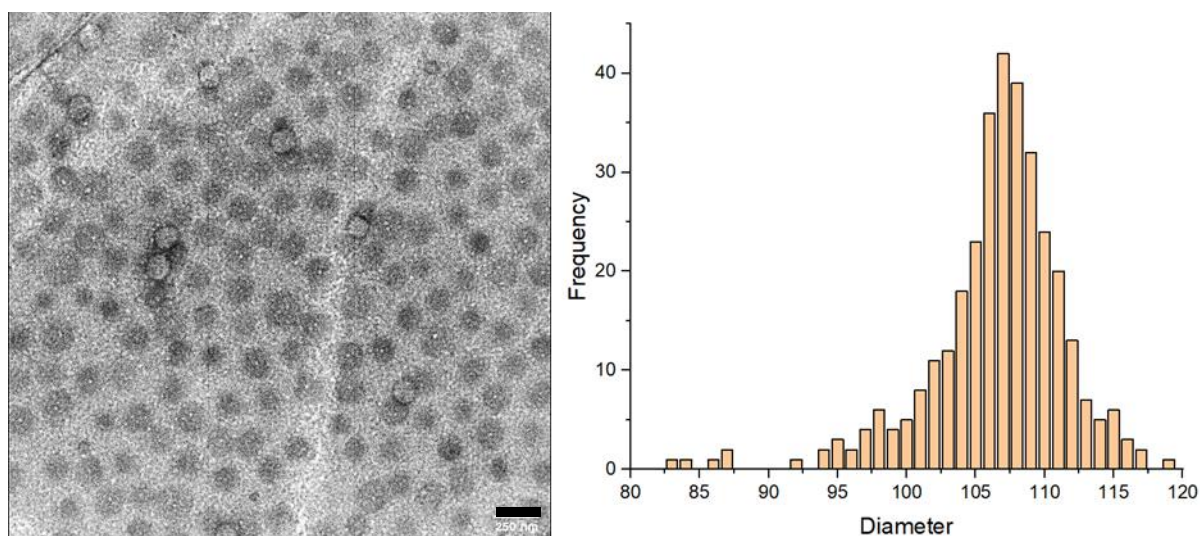


Figure 42 An example TEM image of pDPAEMA₁₀₀ nanoparticles (D1) stained with uranyl acetate, (scale bar = 250 nm) (left), the histogram of size distributions obtained by computer analysis of the TEM image with $N > 250$, mean size = 106 nm, PDi = 0.04 (right)

As well as size, DLS was also used to assess the particles pH responsiveness. This was achieved by first slowly acidifying diluted latex solutions in order to obtain samples of all particles at different pH values between 9 and 2. The diameter of the nanoparticles in each of these samples was then measured using DLS; an example plot is shown Figure 43.

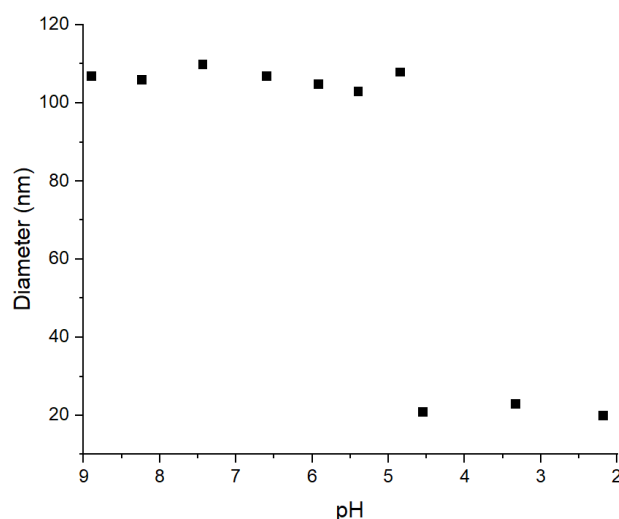


Figure 43 A plot of pDPAEMA₁₀₀ (D1) particle diameter as measured by DLS versus latex solution pH between 9 and 2, showing the dramatic decrease in diameter consistent with disassembly.

The diameter and dispersity of the particles remains roughly constant at pH values above 5; past this point there is a sharp decrease indicating that the particle has disassembled into its constituent polymers. To corroborate this disassembly, the derived scattering count for each DLS measurement was also plotted (Figure 44). As Figure 44 shows, the derived scattering count remains constant and high at pH values above 5, indicating the presence of stable and large nanoparticles, before a sharp decrease as the particles disassemble into smaller objects. To probe the mechanism behind disassembly, the Zeta potential (ZP) was also measured at each pH, showing a clear shift from neutral to positive as pH decreases; indicating the build-up of positive charges caused by the formation of cationic DPAEMA species within the nanoparticle.

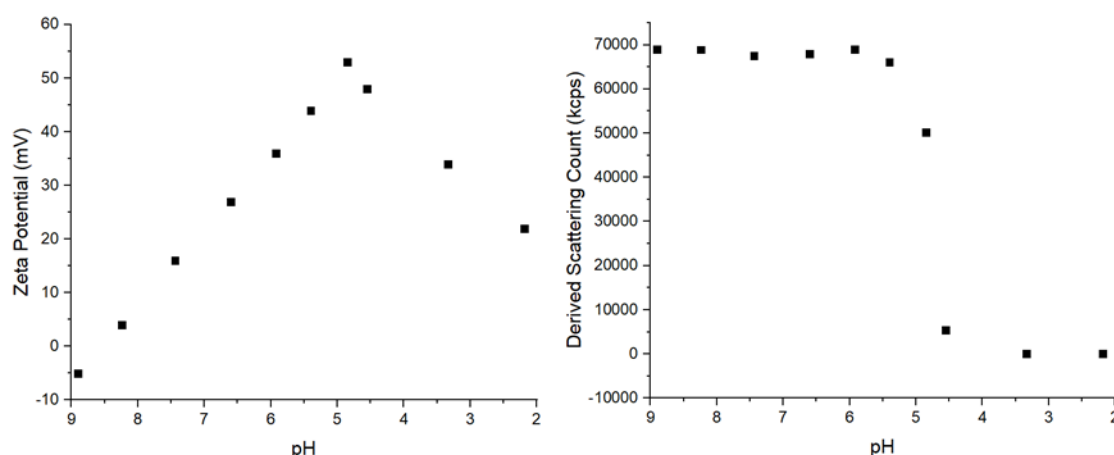


Figure 44 A plot of the zeta potential (left) derived scattering count (right) for pDPAEMA₁₀₀ particles (D1) versus latex solution pH

In order to investigate the time scale that disassembly is occurring on, a UV-Vis turbidity experiment was conducted. In this experiment, a cuvette containing an opaque suspension of particles was fitted with a cannula and placed inside a UV-Vis spectrometer. A known amount of dilute HCl was added to reduce the pH inside the cuvette below the point of disassembly whilst the turbidity of the solution was recorded repeatedly *in situ* at 600 nm. The aim of this experiment was to measure the gradual decrease in turbidity with time; however, even when using the fastest measurement settings (0.5 s), particle disassembly appears to occur instantly. In order to probe the kinetics fully, a measurement system with a shorter time step is required such as *in situ* small angle neutron scattering (SANS) or ultra-fast UV-Vis.

Together the measurements from UV-Vis, along with those from DLS, prove that the disassembly of the particles is highly sensitive to pH and rapid to the point of near instantaneousness. Many applications for such particles may be envisaged; however, in all cases the ability to tailor the pH of the disassembly would be desirable. In the following subsections, the effect on the pH of disassembly of co-polymerising DPAEMA with both inert and responsive monomers is investigated.

3.4.2 Copolymerisation of Two pH Responsive Monomers

First, DPAEMA was copolymerised with a second tertiary amine containing monomer, DEAEMA. Importantly, the reduced hydrophobic crowding around the protonation site of DEAEMA allows for better proton access and an increased pKa value of 7.15 compared with 6.26 for pDPAEMA^{36, 37}.

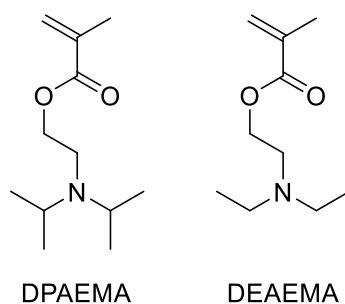


Figure 45 Structures of the responsive monomers, (diisopropylamino)ethyl methacrylate (DPAEMA) (left) and (diethylamino)ethyl methacrylate (DEAEMA) (right)

Five copolymer particles were produced, containing the same overall number of tertiary amines in the core but different ratios of DPAEMA to DEAEMA (D1 – D5 in table 1). As can be expected, particles comprised wholly of the more basic DEAEMA units disassemble at a higher pH (7.3) than those made entirely of DPAEMA (4.7). The pH values of disassembly closely match work by Such *et al.*³⁸ in which DPAEMA and DEAEMA nanoparticles were prepared by nanoprecipitation. However, it should be noted, that disassembly of the mentioned particles takes place over a broader range of pH than was observed for D1 and D5. The particles prepared by Such *et al.* were considerably less monodisperse than D1/D5 owing to their different synthesis methods; it is likely that the broadening of particle disassembly is a consequence of this lack of uniformity. For particles containing both monomers, it is interesting to note that the responsiveness does not appear to follow a linear trend with respect to DEAEMA content. Particles D2 – D4, instead appears to all disassemble at roughly the same pH (~6.5). It was hypothesised that this surprising behaviour shows that particle disassembly is wholly triggered by the protonation of

DEAEMA and that DPAEMA in this instance is acting as an inert hydrophobic monomer. In order to test this theory, a series of DPAEMA/BMA copolymer particles was next produced (B1 – B4).

3.4.3 Copolymerisation of DPAEMA with BMA

To attempt to deconvolute the properties of DPAEMA being both hydrophobic and pH responsive, a series of DPAEMA/BMA copolymer particles was produced. By copolymerising DPAEMA with a non pH-responsive monomer, it is possible to determine the minimum amount of DPAEMA needed to trigger disassembly. As can be seen in table 1, particles containing 75% (B1) and 50% (B2) DPAEMA are still capable of disassembly under acid conditions; however, particle B3, comprised of 25% DPAEMA/ 75% BMA, is no longer responsive. Intuitively, it can also be noted that increasingly acidic conditions were needed to trigger disassembly with decreasing DPAEMA content. Further experiments producing particles with between 25% and 50% DPAEMA narrowed this range to conclude that 35% DPAEMA was the minimum amount needed to drive disassembly. As DPAEMA and BMA are of similar hydrophobicities, it can be proposed that in particles comprised wholly of DPAEMA, that disassembly occurs after approximately 35% of the DPAEMA units have been protonated.

3.4.4 Copolymerisation of DPAEMA with MMA

To probe the effect of hydrophobic content on the responsiveness of particles further, a range of DPAEMA/MMA copolymer particles were also produced (M1 – M4). The inclusion of MMA did reduce the responsiveness of particles, requiring a lower pH to be reached before disassembly occurred. However, in line with its less hydrophobic nature, MMA particles disassembled at a higher pH than their BMA counterparts; 3.9 for B2 vs 4.4 for M2. As well as responding at a higher pH, particles remain capable of disassembly at lower DPAEMA content (25%) than was observed for BMA, e.g. M3 vs B3. Intriguingly, the DLS studies of diameter vs pH described in section 3.3.1, show an abrupt increase

in apparent particle size immediately prior to disassembly as shown in the figure below.

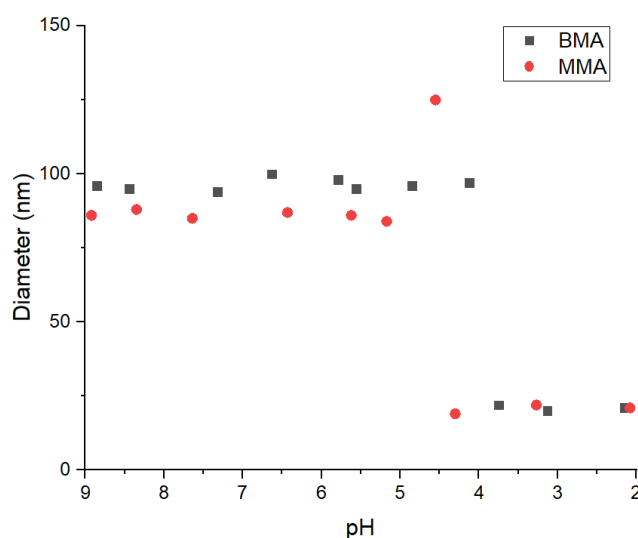


Figure 46 A plot of pDPAEMA₅₀-BMA₅₀ (B2) particle diameter (black) and pDPAEMA₅₀-MMA₅₀ (M2) particle diameter (red) versus latex solution pH

This sudden size increase seems to suggest that the particles swell before collapse, likely due to the increasing number positive charges present inside the particle. Whilst swelling behaviour is routinely observed in responsive nanoparticles³⁹⁻⁴¹, it is unexpected in this instance given the lack of physical crosslinking. One explanation as to how the polymer chains are able resist separation is that they are being held together by grains of crystalline pMMA, a polymer known for its high T_g . It should be highlighted that this swelling behaviour is transient and only observed in samples that were measured immediately after preparation.

3.4.5 Effect of Polymer Chain Length on Particle Responsivness

In order to assess to what extent the hydrophobic content of the nanoparticles resists disassembly, two further particles were prepared (L1 and L2). In these particles, the overall ratios of DPAEMA and BMA were kept the same as earlier experiments (D1 and B2 respectively) but the DP of the polymer was shortened

by half to 50. As before, these particle solutions were then acidified and the diameter measured by DLS (Figure 47).

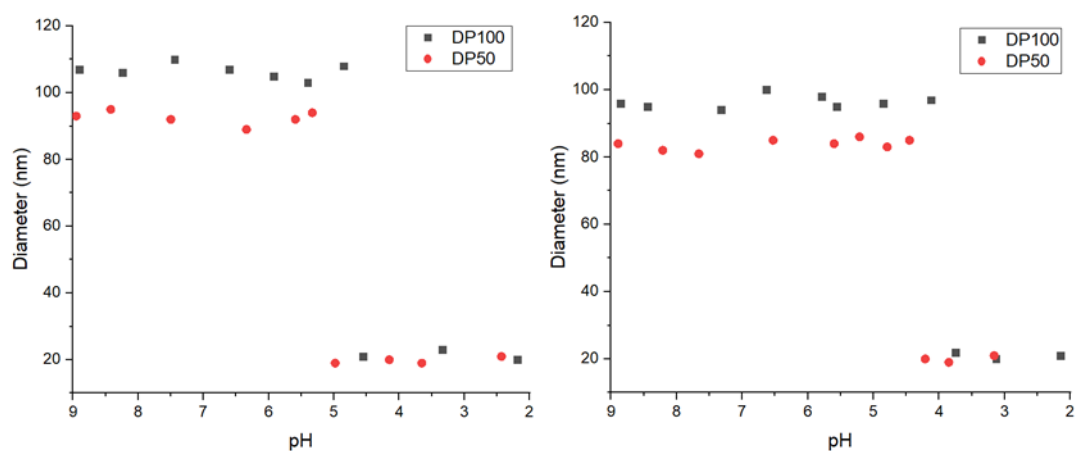


Figure 47 (Left) A plot of pDPAEMA₁₀₀ (D1) particle diameter (black) and pDPAEMA₅₀ (L1) particle diameter (red) versus latex solution pH, (right) a plot of pDPAEMA₅₀-BMA₅₀ (B2) particle diameter (black) and pDPAEMA₂₅-BMA₂₅ (L2) particle diameter (red) versus latex solution pH

In the case of both DPAEMA ratios, particles comprised of shorter polymer chains disassembled at a higher pH; 5.1 vs 4.7 for 100% DPAEMA and 4.4 vs 3.9 for 50% DPAEMA / 50% BMA. In order to explain this increase in responsiveness it is important to consider the thermodynamics of the system. In terms of enthalpy, particle disassembly is driven by the favourable reduction in electrostatic repulsion between cationic species as well as their exothermic solvation. Entropy is more balanced however; polymers transiting from a crowded to free state is clearly exogenic. Conversely, however, the exposure of nonprotonated, hydrophobic surfaces to the bulk solution and the consequential reordering of water molecules is an endogenic process disfavoured by entropy. For shorter DP polymers such as L1 and L2, the total amount of hydrophobic surface that is exposed to the solvent is less than in longer polymers (D1 and B2). Additionally, the PEG stabilizer block remains the same size for both DPs, effectively increasing the polymers hydrophilicity. This

decrease in hydrophobicity reduces the entropic penalty paid for disassembly and hence can occur with a reduced driving force i.e. at a higher pH.

3.4.6 Effect of Temperature on Particle Responsiveness

To explore further the role entropy plays in determining responsiveness, the effect of temperature on disassembly was next investigated. Three comparison experiments were set up (T1 – T3); in these experiments, solutions of pDPAEMA₁₀₀ particles were heated or cooled to 15 °C (T1), 25 °C (T2) and 35 °C (T3) and acidified to provide samples for measurement by DLS (Figure 48).

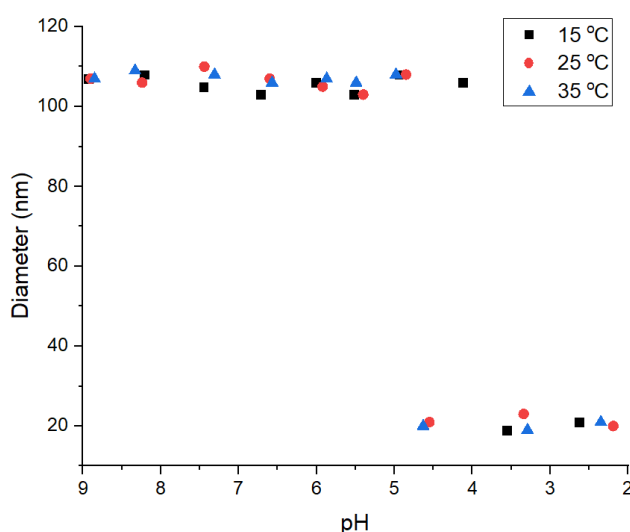


Figure 48 A plot of pDPAEMA₁₀₀ (D1) particle diameter as measured by DLS versus latex solution pH at three different temperatures

Particles at T3 appear to respond at slightly a higher pH than those at T2, however, this is within the error of the experiment. Perhaps it is unrealistic to expect such a small temperature change to have any significant effect on a largely enthalpy driven process, explaining the little difference between T2 and T3. Surprisingly then, particles at T1 are significantly less responsive than their higher temperature counterparts are. Due to the lack of difference between T2 and T3, this dramatic reduction in the disassembly pH cannot be ascribed to entropy and another explanation is required. One possibility is that the pDPAEMA chains are below their glass transition temperature (T_g) at T1 and

above it at T2 and T3. A literature value for the T_g of DPAEMA could not be found, however, one could be obtained for the closely related monomer DEAEMA ($T_g = 20\text{ }^{\circ}\text{C}$)⁴². If it were assumed that the T_g of DPAEMA is similar, then reduction in polymer chain movement at T1 would present a significant barrier to particle disassembly and reduce their overall responsiveness.

3.4.7 Effect of Salt Concentration on Particle Responsiveness

The disassembly of DPAEMA particles is driven by repulsive electrostatic forces between cationic sections of polymers. It was hypothesised that the addition of an inert salt (NaCl) would reduce this electrostatic repulsion by screening these charges; hence reducing the particles responsiveness. Surprisingly, addition of NaCl had little to effect on the pH of disassembly for D1 (100% DPAEMA), even at relatively high concentrations of 10 mM. To explain this, it is first important to understand that the cationic regions of DPAEMA are buried within the core of the particles. The permeability of ions and indeed even the ingress of water into this hydrophobic core is expected to be very low if not none at all. This lack of accessibility means the salt cannot screen the charges and hence there is no reduction in electrostatic repulsion or responsiveness.

3.5 Conclusion

In summary, a library of fifteen nanoparticles were prepared containing varying amounts of tertiary amine pH responsive monomers. The disassembly of these particles as a function of pH is measured and it is shown that their responsiveness is highly tuneable over a range between pH 7 and pH 4. This disassembly is shown to occur over very short time scales and at a precise pH. Additionally the effect of external factors such as temperature and salt on the responsiveness are also measured. The rapid, tuneable and specific disassembly, coupled with their tolerance of salts and increased temperature, leads to the possibility of using the nanoparticles for biological applications such as targeted drug delivery.

3.6 References

1. P. Theato, B. S. Sumerlin, R. K. O'Reilly and I. I. I. T. H. Epps, *Chemical Society Reviews*, 2013, **42**, 7055-7056.
2. Q. Jin, C. Luy, J. Ji and S. Agarwal, *Journal of Polymer Science Part A: Polymer Chemistry*, 2012, **50**, 451-457.
3. P. J. Roth and A. B. Lowe, *Polymer Chemistry*, 2017, **8**, 10-11.
4. X. Zhang, L. Zhou, X. Zhang and H. Dai, *Journal of Applied Polymer Science*, 2010, **116**, 1099-1105.
5. S. S. Shah, J. Wertheim, C. T. Wang and C. G. Pitt, *Journal of Controlled Release*, 1997, **45**, 95-101.
6. R. Francis, C. P. Jijil, C. A. Prabhu and C. H. Suresh, *Polymer*, 2007, **48**, 6707-6718.
7. K. Jain, R. Vedarajan, M. Watanabe, M. Ishikiriya and N. Matsumi, *Polymer Chemistry*, 2015, **6**, 6819-6825.
8. M. Karg and T. Hellweg, *Current Opinion in Colloid & Interface Science*, 2009, **14**, 438-450.
9. A. Blanz, R. Verber, O. O. Mykhaylyk, A. J. Ryan, J. Z. Heath, C. W. I. Douglas and S. P. Armes, *Journal of the American Chemical Society*, 2012, **134**, 9741-9748.
10. V. Marturano, V. Marturano, P. Cerruti, M. Giamberini, B. Tylkowski and V. Ambroggi, *Journal*, 2016, **9**.
11. H. Zhao, E. S. Sterner, E. B. Coughlin and P. Theato, *Macromolecules*, 2012, **45**, 1723-1736.
12. Y. V. Il'ichev, M. A. Schwörer and J. Wirz, *Journal of the American Chemical Society*, 2004, **126**, 4581-4595.
13. N. Fomina, C. McFearn, M. Sermsakdi, O. Edigin and A. Almutairi, *Journal of the American Chemical Society*, 2010, **132**, 9540-9542.
14. M. T. D. Cronin, N. Manga, J. R. Seward, G. D. Sinks and T. W. Schultz, *Chemical Research in Toxicology*, 2001, **14**, 1498-1505.
15. E. V. Sargent and M. O. Bradley, *Mutation Research Letters*, 1986, **175**, 133-137.
16. C. Guizard and H. Cheradame, *European Polymer Journal*, 1979, **15**, 689-693.
17. A. Napoli, M. Valentini, N. Tirelli, M. Müller and J. A. Hubbell, *Nature Materials*, 2004, **3**, 183-189.
18. G. Kocak, C. Tuncer and V. Bütün, *Polymer Chemistry*, 2017, **8**, 144-176.
19. F. Tu and D. Lee, *Journal of the American Chemical Society*, 2014, **136**, 9999-10006.
20. L. I. Gabaston, S. A. Furlong, R. A. Jackson and S. P. Armes, *Polymer*, 1999, **40**, 4505-4514.
21. B. Bingöl, C. Strandberg, A. Szabo and G. Wegner, *Macromolecules*, 2008, **41**, 2785-2790.

22. A. E. Felber, M.-H. Dufresne and J.-C. Leroux, *Advanced Drug Delivery Reviews*, 2012, **64**, 979-992.
23. S. Saleem, S. Rangou, C. Abetz, B. Lademann, V. Filiz and V. Abetz, *Polymers (Basel)*, 2017, **9**, 216.
24. D. N. Crisan, O. Creese, R. Ball, J. L. Brioso, B. Martyn, J. Montenegro and F. Fernandez-Trillo, *Polymer Chemistry*, 2017, **8**, 4576-4584.
25. Y. Guan and Y. Zhang, *Chemical Society Reviews*, 2013, **42**, 8106-8121.
26. D. Li, Q. He, Y. Yang, H. Möhwald and J. Li, *Macromolecules*, 2008, **41**, 7254-7256.
27. E. Tang, K. Du, X. Feng, M. Yuan, S. Liu and D. Zhao, *European Polymer Journal*, 2015, **66**, 228-235.
28. J. Zhao, N. A. D. Burke and H. D. H. Stöver, *RSC Advances*, 2016, **6**, 41522-41531.
29. S. Bazban-Shotorbani, M. M. Hasani-Sadrabadi, A. Karkhaneh, V. Serpooshan, K. I. Jacob, A. Moshaverinia and M. Mahmoudi, *Journal of Controlled Release*, 2017, **253**, 46-63.
30. P. Sar, S. Ghosh, Y. D. Gordievskaya, K. G. Goswami, E. Y. Kramarenko and P. De, *Macromolecules*, 2019, **52**, 8346-8358.
31. T. Yildirim, A. C. Rinkenauer, C. Weber, A. Traeger, S. Schubert and U. S. Schubert, *Journal of Polymer Science Part A: Polymer Chemistry*, 2015, **53**, 2711-2721.
32. O. F. Olaj, A. Kornherr and G. Zifferer, *Macromolecular Theory and Simulations*, 2001, **10**, 881-890.
33. G. Arzamendi, C. Plessis, J. R. Leiza and J. M. Asua, *Macromolecular Theory and Simulations*, 2003, **12**, 315-324.
34. O. F. Olaj and P. Vana, *Macromolecular Rapid Communications*, 1998, **19**, 533-538.
35. T. Junkers and C. Barner-Kowollik, *Journal of Polymer Science Part A: Polymer Chemistry*, 2008, **46**, 7585-7605.
36. A. Darabi, A. R. Shirin-Abadi, P. G. Jessop and M. F. Cunningham, *Macromolecules*, 2015, **48**, 72-80.
37. D. C. Forbes, M. Creixell, H. Frizzell and N. A. Peppas, *European Journal of Pharmaceutics and Biopharmaceutics*, 2013, **84**, 472-478.
38. N. Kongkatigumjorn, S. A. Smith, M. Chen, K. Fang, S. Yang, E. R. Gillies, A. P. R. Johnston and G. K. Such, *ACS Applied Nano Materials*, 2018, **1**, 3164-3173.
39. Y. Li, K. Xiao, W. Zhu, W. Deng and K. S. Lam, *Advanced Drug Delivery Reviews*, 2014, **66**, 58-73.
40. K. Na and Y. H. Bae, *Pharmaceutical Research*, 2002, **19**, 681-688.
41. Y. Zhang, W. Gu, J. Zhao and Z. Qin, *Colloids and Surfaces A: Physicochemical and Engineering Aspects*, 2017, **531**, 1-8.

42. L. Martín-Gomis, R. Cuervo-Rodriguez, M. C. Fernández-Monreal, E. L. Madruga and M. Fernández-García, *Journal of Polymer Science Part A: Polymer Chemistry*, 2003, **41**, 2659-2666.

4 *In Vivo* applications of pH Responsive Nanoparticles

4.1 Overview

In this chapter, pH responsive nanoparticles based around those designed in chapter 3, will be investigated as potential drug delivery vehicles for improved delivery of an experimental anti-cancer drug.

4.2 Introduction

4.2.1 Polymeric Nanoparticles for Drug Delivery

As reviewed extensively in the thesis introduction (Section 1.1.3) there are several advantages to encapsulating small molecule drugs within polymeric nanoparticles for delivery *in vivo*. One advantage is the ability to protect sensitive therapeutics such as RNA from metabolism in the body. Encapsulation within a nanoparticle also allows for the delivery of poorly water-soluble hydrophobic drug molecules. Whilst polymeric nanoparticles have the potential to improve drug delivery significantly, they have two problems that must first be addressed. Firstly, the release of drugs from the nanoparticle must be tightly controlled. Release by diffusion alone is often discussed in the literature; however, a careful balance must be struck. If diffusion is rapid, then premature drug release will occur; conversely, if diffusion is impeded, then the drug will never become available to the body. The second problem that must be addressed is the clearance of the polymer nanoparticle from the body¹. Depending on size and surface composition, nanoparticles may be rapidly phagocytosed and cleared from the body *via* the liver before they can deliver the drug. However, so-called "stealthy" nanoparticles that avoid rapid clearance may accumulate to potentially hazardous levels, even after drug release². A promising solution to these problems is to use stimuli responsive nanoparticles³, such that drug release

can be controlled and triggered. Furthermore, a response that degraded the nanoparticle into small units upon drug release, would allow for more efficient clearance after drug delivery had been achieved. A range of stimuli responsive polymers are discussed in the introduction of chapter 3 (section 1.1.2), however, pH responsive nanoparticles are perhaps the most widely investigated for drug delivery⁴; several literature examples are reviewed in the following section.

4.2.2 pH Responsive Polymeric Nanoparticles for Drug Delivery

The pH within the body varies widely, from near pH 8 in the small intestine down to pH 3.5 in the stomach⁵. The wide range of pH, coupled with its localisation within the body, makes it an attractive endogenous stimulus to utilise for responsive systems. Numerous pH responsive nanoparticles⁴ have been designed; however, they can broadly be divided into five groups based on their mechanism of action, each of which is discussed below.

4.2.2.1 Electrostatic Complexes

Perhaps the simplest design of pH responsive nanoparticles; electrostatic complexes are electrostatic complexes formed between oppositely charged polymer and therapeutic cargos including drugs and DNA. Chen et al. utilised this method to produce nanoparticles formed from positively charged chitosan polymers and the negatively charged prodrug, sulfasalazine for the treatment of peptic ulcers⁶. Administered orally, these nanoparticles retained their structural integrity within the stomach; the pH not being low enough to protonate the anionic sulfasalazine. However, upon reaching their target location of the duodenum, the surrounding pH increased significantly to pH 8. At this higher pH, the amino groups of the chitosan polymers begin to become deprotonated and lose their cationic nature. The loss of positive charge weakens the electrostatic complex and triggers the release of sulfasalazine. Such electrostatic complexes are useful for orally administered drugs; however,

they require a drug that is precisely ionized at specific pH values, limiting the scope of the system.

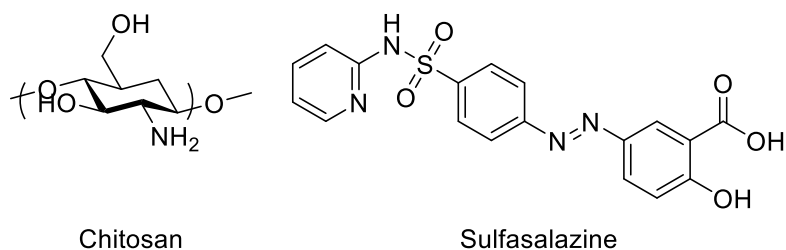


Figure 49: The chemical structures of chitosan and sulfasalazine, drawn in their neutral forms.

4.2.2.2 Swellable Nanoparticles

Cross-linked nanoparticles can easily be formed by emulsion polymerisation of hydrophobic monomers in the presence of multifunctional monomers⁷. By using hydrophobic monomers with ionisable pendent groups, it is possible to make the nanoparticle pH responsive. Protonation and deprotonation of this pendent group leads to a build-up of like charge along the polymers, resulting in the electrostatic repulsion from one another. The crosslinking points of the network prevent total dissolution of the nanoparticle and instead lead to one that can reversibly swell at certain pH values. An example of such a swellable nanoparticle for drug delivery is provided by Irvine and co-workers⁸. Their system comprised of 250 nm nanoparticles made from PEG cross-linked (PEG dimethacrylate) and 2-diethylaminoethyl methacrylate (DEAEMA). The tertiary amine pendent groups of DEAEMA become protonated under acidic condition causing the nanoparticles to swell considerably to 550 nm in diameter. The authors showed that under both laboratory conditions and in vitro, that this swelling could be used to trigger the release of a preloaded drug. One advantage of swellable systems is that the swelling is reversible. Irvine *et al.* utilized this reversible swelling to good effect by loading the drug under acidic conditions when the nanoparticle is more permeable, before increasing the pH and contracting the nanoparticle, effectively trapping the drug inside.

However, this structural resilience can prove a disadvantage by hindering clearance of the polymers from the body after drug delivery.

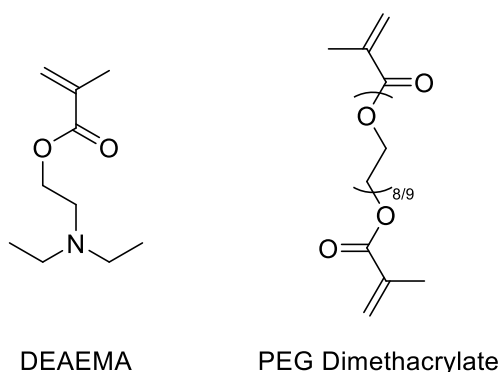


Figure 50: The chemical structures of DEAEMA and PEG dimethacrylate.

4.2.2.3 Hydrolysable Nanoparticles

Similar in design to swellable nanoparticles, hydrolysable ones are also cross-linked. However, in hydrolysable nanoparticles, these cross-linkers are subject to hydrolysis at specific pH values. Degradation of these cross-linking points reduces the structural integrity of the nanoparticle and increasing their permeability, allowing for drug release. Hydrolysis of the nanoparticle into its composite polymers allows for increased clearance from the body after drug release. However, the increase in permeability is not necessarily enough to trigger rapid drug release; Schubert *et al.* present an elegant solution to this problem in the form of their doubly hydrolysable nanoparticles⁹. In this work, a hydrolysable cross-linker, propane-2,2-diylbis(oxy))bis(ethane-2,1-diyl)diacrylate (KTDA) was used in conjunction with N-[(2,2-Dimethyl-1,3-dioxolane)methyl]acrylamide (DMDOMA), the structures of which are provided below (Figure 51).

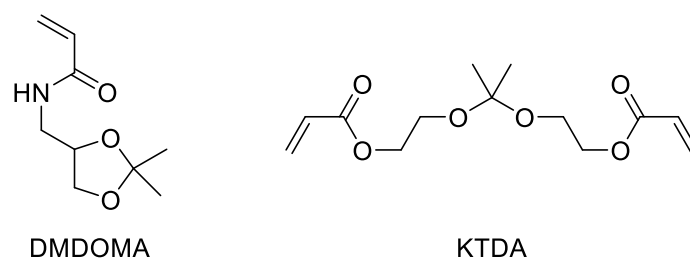


Figure 51: The chemical structures of DMDOMA and KTDA.

Under acidic conditions, the ketal group in the centre of cross-linker hydrolyses; weakening the structure of the nanoparticle. Concurrently, the ketal pendant groups of DMDOMA are also hydrolysed, yielding a diol and significantly increasing the polymers hydrophilicity. The simultaneous removal of cross-linking points and the increase in polymer solubility, leads to complete disassembly of the nanoparticle and release of the encapsulated drug. The lower molecular weight, hydrophilic polymers are then easily removed from the body.

4.2.2.4 Cleavable Linkers

Related to hydrolysable nanoparticles, Moscatelli *et al*/ used cleavable linkers between the drug and the nanoparticle⁴⁸. The most common of these is the hydrazone, formed reversibly by the reaction of a hydrazide and a ketone or aldehyde. Whilst stable at neutral pH, this dynamic bond is hydrolysed below pH 5, separating the drug from the nanoparticle. Hydrolysis of the drug linker does not necessarily lead to rapid drug release; however, this mechanism does have two major advantages. Firstly, with the drug molecule covalently attached to the nanoparticle, it is not possible for it to diffuse out prematurely; especially important for potentially toxic drugs. Secondly, the drug is often attached to the monomer prior to polymerisation into a nanoparticle. Whilst seemingly trivial, this attachment before nanoparticle formation (Figure 52), allows for much higher drug loading contents than are otherwise achievable. Moscatelli *et al.* exploited this in the preparation of p(lactic acid) nanoparticles, loaded with an impressive 27% w/w of doxorubicin¹⁰. Whilst very useful at loading

high concentrations of drug molecules, cleavable linkers, along with hydrolysable nanoparticles both suffer from relatively slow drug release profiles, 30% Dox released in 4 days for the Moscatelli example.

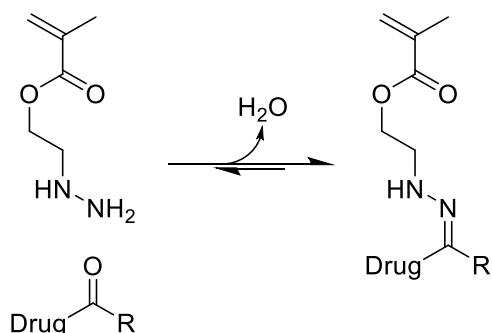


Figure 52: The formation of a hydrazone linked drug monomer, note the equilibrium can be forced forwards by removal of water.

4.2.2.5 Disassembly

The final group of pH responsive nanoparticles are those that fully disassemble with changes in pH. Similar in design to swellable systems mentioned earlier, but lacking the crucial cross-linker, changes in pH leads to a build-up of charge on the composite polymer chains followed by electrostatically driven disassembly. Discussed extensively in chapter 3, this group of pH responsive nanoparticles are gaining increased attention as drug delivery vehicles¹¹. One example of such a nanoparticle that disassembles with pH is provided by Armes and co-workers¹². In their paper, an amphiphilic block copolymer was prepared using 2-diethylaminoethyl methacrylate (DEAEMA) and methacrylic acid (MAA). At basic pH, these copolymers assemble into nanoparticles with the DEAEMA as the core. As the pH is decreased, protonation of the tertiary amine groups of DEAEMA leads to a build-up of positive charge and electrostatic repulsion between chains. At low enough pH (pH ~6), this repulsion drives the rapid disassembly of the nanoparticles into their unimeric polymers. The main advantage of disassembling pH responsive nanoparticles over the other groups is the speed with which an encapsulated drug can be released. Disassembly is sufficiently rapid as to allow for intracellular drug

release; not possible for slower responding nanoparticles which would be expected to be cleared from the cell by transcytosis before delivery could occur.

4.2.3 Objectives

The main objective of this chapter is to investigate pH responsive nanoparticles as potential drug delivery vehicles for improved drug delivery. The nanoparticles will be designed to disassemble rapidly within the lysosome of cells, allowing direct release of drugs intracellularly. For disassembly to occur within the lysosome, the nanoparticle must respond at pH values no lower than 4.5. Based on the findings of chapter 3, nanoparticles comprised of copolymers of DEAEMA and DPAEMA will therefore be investigated.

4.3 Experimental

4.3.1 Materials

Monomers; diisopropylaminoethyl methacrylate (DPAEMA) and diethylaminoethyl methacrylate (DEAEMA) were purchased from Sigma Aldrich and passed through a short aluminium oxide column to remove inhibitor prior to use. The initiator, 2,2'-azobis[N-(2-carboxyethyl)-2-methylpropionamidine]-tetrahydrate (VA-057), was purchased from Wako chemicals and used as provided. 3T3, Caco-2 and Hepa1-6 cells were regenerated from frozen stocks available at the University of Warwick, originally sourced from ATCC, and grown in Dulbecco's modified Eagle's medium (DMEM) supplemented with 10% (v/v) fetal bovine serum (FBS) and 2 mM of L-glutamine and penicillin at 37 C. FY26 was provided by the Sadler group at the University of Warwick.

4.3.2 Animals

Male C57BL/6J mice were provided by the University of Warwick Animal Husbandry Unit. Animals were acclimatized for 1 week prior to the *in vivo* study beginning.

4.3.3 Analytical Techniques

4.3.3.1 Size Exclusion Chromatography (SEC)

SEC was performed on an Agilent Infinity II MDS instrument equipped with differential refractive index (DRI) and multiple wavelength UV detectors, one of which is set to 309 nm. The column used for separation is a PLgel Mixed C columns (300 x 7.5 mm) and a PLgel 5 μ m guard column. The eluent is THF with 2 % triethylamine (TEA) and 0.01 % butylated hydroxytoluene (BHT) additives. Samples were run at 1ml/min at 30 °C. Poly(methyl methacrylate) (pMMA) (2000 to 1,500,000 g mol⁻¹) and polystyrene standards (Agilent EasyVials) were used for calibration, analysis was carried out compared to the pMMA standards. Analyte samples were filtered through a GVHP membrane with 0.22 μ m pore size before injection. Experimental molar mass (M_n , SEC) and dispersity (\mathcal{D}) values of synthesized polymers were determined by conventional calibration using Agilent GPC/SEC software.

4.3.3.2 Dynamic Light Scattering (DLS)

Samples were prepared by diluting nanoparticle latexes 1000-fold with DI water to a final concentration 0.2 mg/mL. DLS measurements were performed on a MALVERN Zetasizer Nano ZS operating at 25 °C with a 4 mW He-Ne 633 nm laser module. Measurements were made in back scattering mode at an angle of 173°. Measurements were performed in triplicate with automatic attenuation selection and measurement position. The results were analysed using Malvern DTS 6.20 software.

4.3.3.3 Ultra Violet-Visible Light Spectroscopy (UV-Vis)

UV-vis measurements were performed on a Beckman DU640 instrument at 25 °C using a laser set at a wavelength of 581 nm. A quartz cuvette with a path length of 1 cm was used for all measurements. Measurements were performed with automatic attenuation selection. Samples measured were prepared by diluting them 100 fold into DI water or by a further 10 fold if measured absorbance values were greater than 1.

4.3.3.4 Determination of Encapsulation Efficiency

A 10 μL aliquot of previously purified drug encapsulated nanoparticles were diluted with 900 μL DI water and 90 μL of 0.1M HCl added. The UV-vis absorbance of this sample at 581 nm was measured as described above (Section 4.3.3.3). This absorbance value was then converted to a molar concentration by use the Beer-Lambert law and previously determined molar extinction coefficient ($\epsilon_{581} = 19,400 \text{ mol}^{-1} \text{ cm}^{-1}$). The molar concentration was then converted to a mass of FY26. The encapsulation efficiency was then determined as the mass of encapsulated FY26 divided by the mass of FY26 added (1 mg). For clarity, an example calculation is provided below. (149 μM 68%)

Measured absorbance and 581 nm = 0.289 abs

Molar concentration of UV-vis sample = 0.0149 μM

Molar concentration of starting aliquot = 1.49 μM

Mass of FY26 in starting aliquot = 0.0677 mg

Mass of FY26 encapsulated in total solution = 0.677 mg

Mass of FY26 added to initial solution = 1 mg

Encapsulation efficiency = $0.677 / 1 \times 100 = 67.7\%$

4.3.3.5 Inductively Coupled Plasma Mass Spectrometry (ICP-MS)

ICP-MS samples were prepared from homogenised organs (collection details Section 4.3.4.5) by first diluting 0.1 g of organ into 1 mL DI water. This solution was then acidified with 0.1 mL nitric acid and heated to 70 °C for 1 hour. Separately, a standard solution of DI water, 0.5% v/v butanol, 0.5% v/v nitric acid, 0.01% v/v triton surfactant was prepared and rhodium (0.1 ppb) and lead (0.1 ppb) added as internal standards. 0.1 mL of the acidified organ solution was then diluted with 4.9 mL of the standard solution yielding the final sample solution. Samples were then measured on an Agilent LC-ICP-MS (7900) at 25 °C.

4.3.4 Biological Techniques

4.3.4.1 Sulforhodamine B cell viability assay

Murine fibroblast (3T3) cells were seeded at a density of 10,000 cells per well and incubated for 24 h. Nanoparticles were diluted with cell culture medium (DMEM + 1% PenStrep + 1% L-Glu + 10% FCS) to make solutions of 1 µg/mL, 10 µg/mL, 100 µg/mL, 1 mg/mL, and 2 mg/mL. Additionally N,N,N',N'-Tetrakis(2-pyridylmethyl)ethylenediamine was used as a positive control to ensure the assay was functioning. The cells were incubated in the presence of the nanoparticle suspensions for 72 h. To determine the cell viability the sulforhodamine B colourimetric assay was used. 50 µL of cold 50% trifluoroacetic acid were added to each well of the plate and left to incubate for 1 h at 4°C, the plate was subsequently washed 10 times with slow running tap water to remove excess trifluoroacetic acid and the plate was heated gently with warm air to remove moisture. 50 µL of 0.4% sulforhodamine B (prepared in 1% acetic acid) were added to each well of the plate and the plate was allowed to stand for 30 min at ambient temperature. Excess dye was removed by washing the plate 5 times with 1% acetic acid. 200 µL of 10 mM Tris base solution (pH 10.5) were added to each well of the plate and was left to stand

at ambient temperature for 1 h. The absorbance of each well was measured at 570 nm on a BioRad iMark 96-well microplate reader. The experiments were carried out as duplicates of triplicates in independent experiments.

4.3.4.2 Cell Uptake Study

Human colorectal adenocarcinoma (Caco-2) cells were seeded at a density of 10,000 cells per well and incubated for 24 h. Cy-3 labelled versions of nanoparticle (D1) was diluted with cell culture medium (DMEM + 1% PenStrep + 1% L-Glu + 10% FCS) to make solutions of concentration 0.01 mg/mL, 0.025 mg/mL, 0.05 mg/mL, 0.1 mg/mL and 0.2 mg/mL. The incubated Caco-2 cells were then rinsed with PBS and solutions of nanoparticles added directly. Cells were either then incubated for 24 hrs with all five concentrations of nanoparticles, or incubated with only 0.2 mg/mL solution of nanoparticles for varying times 0.5 hrs, 1 hrs, 2 hrs, 3 hrs and 4 hrs. Cells were then washed with FBS twice to remove free nanoparticles. Flow cytometry was then used to determine the percentage of fluorescent cells with a laser and detector set at a wavelength of 525 nm and 560 nm respectively. The measurement was gated with Caco-2 cells that been incubated without nanoparticles (negative control).

4.3.4.3 Tumour Model Synthesis

Hepa1-6 cells were incubated in a nutrigel matrix for 72 hrs before being injected subcutaneously into the flanks of each mouse, previously anaesthetised by isoflurane inhalation (2-5% v/v). The cells were left to grow *in situ* for a further 216 hrs (9 days), yielding tumours with an approximate starting size of 50 mm³.

4.3.4.4 Particle Injections

Mice were anaesthetised by isoflurane inhalation (2-5% v/v) before being injected directly into the lower right quadrant of the abdomen. Total drug concentration injected was fixed at 5 milligrams per kilogram of body weight (25-30 g).

4.3.4.5 Organ and Tumour Collection

Mice were anaesthetised by isoflurane inhalation (2-5% v/v) and exsanguinated before being immediately killed humanely by a lethal injection of sodium pentobarbital. The liver and both tumours were then removed and rinsed with PBS. The organs were then homogenised in 5 mL of DI water ready for ICP-MS analysis.

4.3.5 Synthetic Procedures

4.3.5.1 Nanoparticle synthesis

In a typical nanoparticle synthesis; 102.2 mg PEG-CTA (1 eq, 0.046 mmol) was dissolved in 5 mL of deionised water in a 20 mL glass vial, 0.973 mL DPAEMA (875 mg, 90 eq, 4.10 mmol) and 0.253 mL of a VA-057 stock solution (0.01 g/mL H₂O) (2.53 mg 0.125 eq, 0.00610 mmol) were then added to the reaction. The vial was then sealed and briefly vortexed before purging with nitrogen gas for 15 min. The reaction was then heated to 70 °C and stirred at 500 RPM for 90 minutes to form a white latex. When targeting polymers of various DP, the ratio of PEG-ester CTA to VA-057 was kept constant and the amount of monomer varied with respect to the CTA. For fluorescently labelled nanoparticles, 1 mg of Cy3-Am was added to the reaction mixture prior to degassing.

4.3.5.2 Cyanine – 3 Acrylamide Synthesis

5 mg cyanine – 3 amine.hydrochloride salt (1 eq, 0.00079 mmol) was dissolved in 0.5 mL dichloromethane and 3.30 µL triethyl amine added (3 eq, 0.0024 mmol). The vial was sealed and the solution degassed for no longer than 5 minutes to avoid excess solvent evaporation. 530 µL of a 1.5 mM solution of acryloyl chloride in dichloromethane was then injected slowly into the vial and left to stir at room temperature overnight. The final product was purified via preparative HPLC using 90% MeOH / 10% DCM and its presence confirmed by ESI-MS [$M^+ + Cl^-$] at 644.38 and 646.39.

4.3.5.3 Drug Loading Procedure

100 μ L of a 10 mg/mL solution of FY26 in either; dioxane, tetrahydrofuran, methanol, dimethylformamide or water, was added to 900 μ L of 10 mg/mL nanoparticle solution. The solutions were then briefly vortexed to mix before being left to shake overnight on a roller. In later experiments, longer shaking time was found to be beneficial to drug loading; described in text (Section 4.4.4).

4.3.5.4 Particle Purification – Column Chromatography

Shaken nanoparticle solutions were passed through a Sephadex packed PD-10 de-salting column to remove any free FY26, following manufactures instructions. Briefly, the shaken solution was pipetted onto the top of the column and allowed to soak in; DI water was added in 5x1 mL to wet the column continually. FY26 loaded nanoparticles were observed to elute as a turbid bright blue solution. Free FY26 formed a distinct band at the top of the column that did not elute within the time scale of the purification.

4.3.5.5 Particle Purification – Centrifugal Dialysis

Shaken nanoparticle solutions were loaded into centrifugal dialysis membranes with a 10 kDa size cut off range, provided by Thermo Fisher. The dialysis membrane was fitted into 50 mL falcon tube and centrifuged at 13,000 RPM for 10 minutes. Approximately 1 mL of free FY26 collected in the bottom of the falcon tube as a blue solution, which was subsequently discarded. 1mL of DI water was added to the nanoparticle solution before centrifuging for a further 10 minutes. This procedure was repeated until the discarded solution was no longer visibly blue.

4.4 Results and Discussion

4.4.1 Design and Synthesis of Nanoparticles

pH responsive nanoparticles were synthesised based on the work discussed in Chapter 3. Briefly, an amphiphilic PEG – based RAFT agent was used as the

surfactant in the emulsion polymerisation of two pH responsive monomers; DPAEMA and DEAEMA (structures below) into both homo and copolymers.

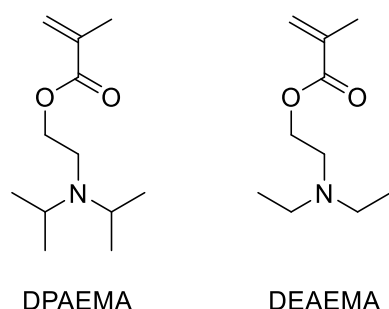


Figure 53: Chemical Structures of DPAEMA (left) and DEAEMA (right)

In order to yield identically sized 100 nm particles, a slightly shorter degree of polymerisation was targeted for DPAEMA than DEAEMA (DP90 vs DP100 respectively). As described in detail in chapter 3, dynamic light scattering (DLS) was used on samples at different pH values to determine the pH point of disassembly (table 1).

Table 7 A summary of nanoparticles and their composite polymers prepared and studied in this chapter.

Experiment	Composition	M_n (Da) ¹ / \bar{D}^2	Diameter (nm) ³ /PDI ⁴	pH of Disassembly ⁵
D1	pDPAEMA ₉₀	30,800 / 1.18	101 / 0.02	4.8
D2	pDPAEMA ₇₀ – DEAEMA ₂₅	30,900 / 1.17	102 / 0.03	6.4
D3	pDPAEMA ₅₀ – DEAEMA ₅₀	31,800 / 1.17	103 / 0.05	6.5
D4	pDPAEMA ₂₅ – DEAEMA ₇₅	29,900 / 1.15	104 / 0.04	6.8
D5	pDEAEMA ₁₀₀	28,400 / 1.14	102 / 0.02	7.3

1 experimental number-average molar mass of the polymers determined by SEC-THF using a PMMA calibration system. 2 Dispersity of the polymer (M_w/M_n) as determined by SEC-THF. 3 intensity weighted average diameter as measured by dynamic light scattering. 4 particle

dispersity index calculated from dynamic light scattering. 5 average value for pH between the last assembled and first disassembled points as determined by DLS size.

The nanoparticles disassemble at a broad range of pH values, all of which are greater than the pH of the lysosome but less than physiological pH, with the possible exception of D5. The nanoparticles are therefore expected to remain intact during transport through the body and only disassemble once internalised into a cell. In this way, encapsulated drugs may be rapidly released selectively within cells; eliminating the problems discussed in the introduction (Section 1.1.3).

4.4.2 *In vitro* cell toxicity assay

Once prepared, the toxicity of the nanoparticles was next assessed *in vitro* via a Sulforhodamine B (SRB) cell viability assay. This assay utilizes a chromophore, SRB, which is capable of electrostatically binding with negatively charged amino acids present in cell membrane proteins. This binding is stoichiometric and can then be used to determine overall cell biomass present quantitatively. Murine fibroblast cells (3T3), were used as the model for healthy cells due to their similar metabolic activity and well-regulated growth rates. In addition to this living 3T3 cells are also known to be extremely adherent, allowing easy separation of living and dead cells by simple washing. The 3T3 cells were incubated in the presence of each DPAEMA/DEAEMA nanoparticle (D1 – D5) at five different concentrations up to 2 mg/mL for a total of 72 hrs. After incubation, SRB was added to the cells and left to stain for 0.5 hrs, before both the dead cells and excess SRB were removed by thorough washing. The absorbance of each sample was then measured at 570 nm and compared to a negative control to determine overall cell viability (Figure 54)

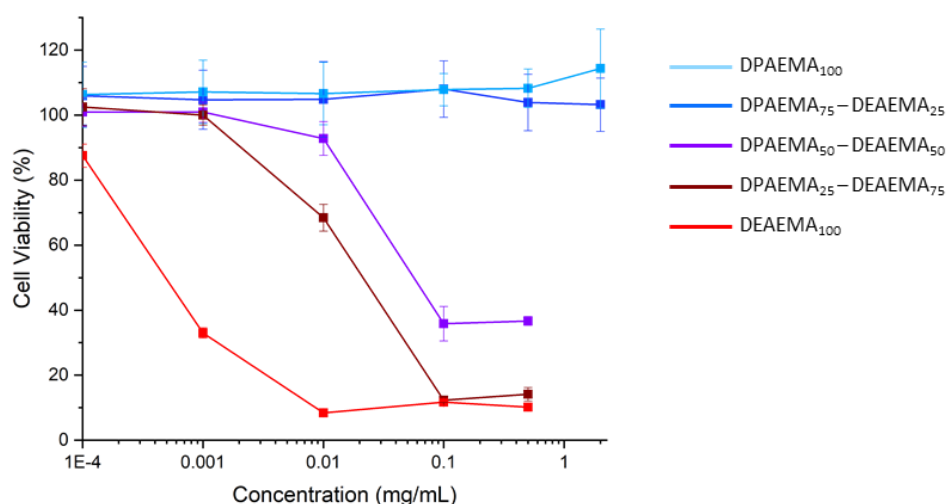


Figure 54: The cell viability of 3T3 cells exposed to 5 different nanoparticles; DPAEMA₁₀₀ (light blue), DPAEMA₇₅-DEAEMA₂₅ (dark blue), DPAEMA₅₀-DEAEMA₅₀ (purple), DPAEMA₂₅-DEAEMA₇₅ (dark red) and DEAEMA₁₀₀ (red), at a range of concentrations

Nanoparticles made entirely of DPAEMA (light blue) or 75% DPAEMA – 25% DEAEMA (dark blue) had no effect on cell viability at any concentration measured indicating that they are non-toxic. In stark comparison, nanoparticles comprised entirely of DEAEMA (red), reduced cell viability at all but the very lowest concentrations. The dramatic reduction in cell viability strongly suggests that the DEAEMA nanoparticles are toxic. Furthermore, inclusion of 50% or more DEAEMA within the nanoparticle also reduces cell viability at higher concentrations as seen for 50% DPAEMA – 50% DEAEMA (purple) and 25% DPAEMA – 75% DEAEMA (dark red). Nanoparticle toxicity therefore seems strongly linked to the DEAEMA present, however, it is unclear why given its similar chemical nature to the nontoxic DPEAMA. The PEG outside of all particles assayed is the same and it is therefore reasonable to assume that the toxic qualities of DEAEMA do not become present until after particle disassembly. One important difference between DEAEMA and DPAEMA that may explain their differing toxicity is their pKa values. As discussed *vide supra* (section 4.4.1), DEAEMA has a lower pKa value than DPAEMA; pDEAEMA would therefore be expected to be more protonated than pDPAEMA at the same pH. This increase in ease of protonation, leads to the

formation of increasingly cationic free polymers with DEAEMA content. Strongly cationic polymers have been shown repeatedly to be toxic due to their membrane disrupting abilities¹³. This would provide a possible explanation as to why otherwise identical nanoparticles exhibit increased cell toxicity with DEAEMA content. Due to the toxicity associated with DEAEMA, 100% DPAEMA particles (D1) were the only ones taken forward to the next stage.

4.4.3 Cell Uptake Study

The cell uptake of 100% DPAEMA nanoparticles (D1) was next assessed using cyanine-3 acrylamide (0.2 mg/mL) labelled nanoparticles. DLS of these fluorescent nanoparticles could not be obtained due to the interference between Cy3 and the laser set-up within the DLS. However, it is assumed that at such low concentration, the presence of Cy3Am does not interfere with the nanoparticles size. A range of different concentrations of the fluorescent nanoparticles was then incubated with Caco-2 cells (human colorectal adenocarcinoma) for 24 hrs. The uptake of nanoparticles was then measured by flow cytometry gated against negative control cells and plotted below (Figure 55).

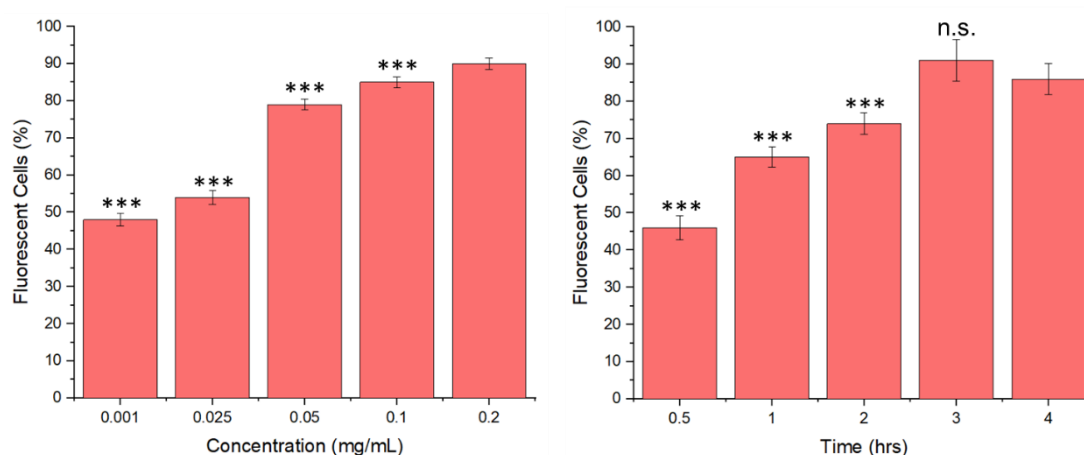


Figure 55: Fluorescent cell data for CY3-labeled DPEAMA nanoparticles versus concentration (left) and time (right). Statistical significance was assessed by one-way ANOVA followed by Tukey's multiple comparison test, *** = $p \leq 0.01$ when compared to the final value (0.2 mg/mL and 4 hrs).

Figure 55 (left) shows that increasing the concentration of nanoparticles incubated, leads to a proportionate increase in the number of fluorescent cells; up to $90 \pm 0.54\%$ for the highest concentration measured. The proportionate increase suggests that the nanoparticles are being uniformly uptaken by all cells rather than biasing some in what is termed the sergeant-soldier effect. As well as assessing cell uptake at different concentrations, nanoparticle internalisation was also measured at varying time points. For this experiment, 0.2 mg/mL of nanoparticles were incubated with cells for various amounts of time (0.5 – 4 hrs) before the fluorescence cell data was collected and plotted (Figure 55-right). Nanoparticles showed very rapid internalisation, generating almost 50% fluorescent cell within 0.5 hrs. The percentage of fluorescent cells continues to increase before reaching a maximum of $91 \pm 4.3\%$ after 3 hrs; consistent with the maximum value for this concentration recorded earlier.

These *in vitro* cell uptake results suggest that the nanoparticles would be rapidly and uniformly uptaken if inside of a tumour *in vivo*; a very favourable behaviour for a drug delivery nanoparticle.

4.4.4 Drug loading and Purification

Having shown that the 100 nm DPAEMA particles were non-toxic and capable of rapid cell internalization, the next stage was to load them with an anticancer drug for *in vivo* testing. An experimental osmium based drug, coded as FY26, was selected for drug loading. This drug had previously been shown to be highly effective; on average 49 times more active than cisplatin against 809 cancer cell lines¹⁴. However, FY26 also suffers from high toxicity/lethality *in vivo*¹⁵ as well as relatively poor solubility. As discussed in the introduction, encapsulation within a nanoparticle could help to decrease the drugs toxicity as well as increasing its solubility. Additionally the osmium centre as well as the drugs very strong UV-vis absorbance provide useful analytical handles for tracking the drug.

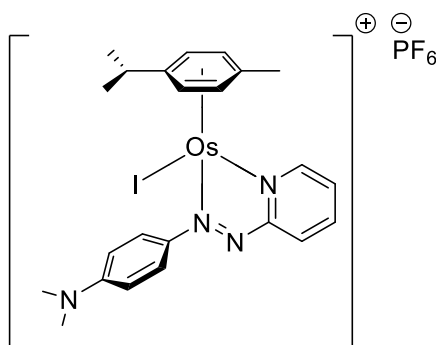


Figure 56: The chemical structure of the anti-cancer drug used, coded as FY26

Initially, drug loading was trialled by first dissolving FY26 in the DPAEMA monomer before addition to a solution of PEG-CTA and VA-057 initiator in water. This mixture was then polymerised as discussed *vide supra* (section 4.4.1), before any remaining free drug was removed. DLS and SEC were used to confirm that the presence of the drug, did not affect the polymer or nanoparticles formed (Figure 57).

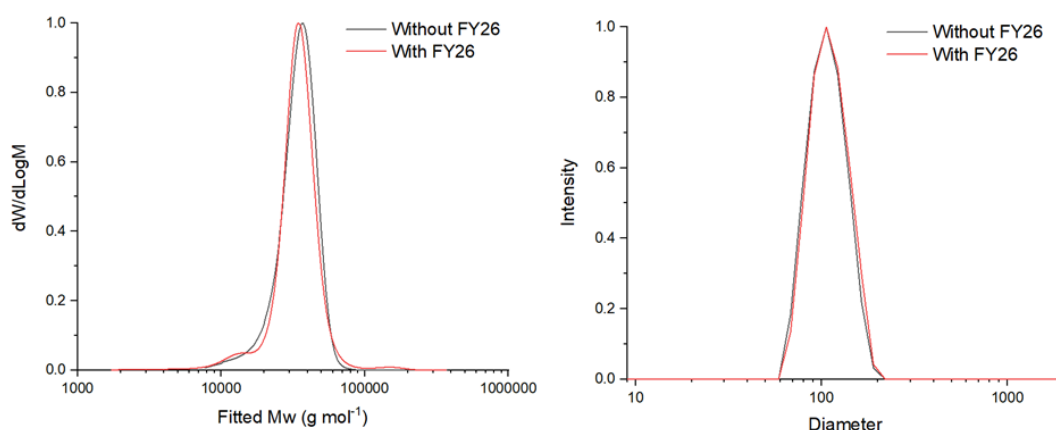


Figure 57: SEC (left) and DLS (right) chromatogram of a pDPAEMA₉₀ emulsion polymerisation in the presence (red) and absence (grey) of FY26

Once the nanoparticles were formed, any remaining free FY26 needed to be removed. To achieve this, the nanoparticle solutions were run through a PD-10 desalting columns with pores large enough to allow nanoparticle elution. Both the nanoparticles and free drug progress through the column was followed by their intense blue colour and eluted as distinct separate fractions. DLS was again used to ensure that column had not affected particle size or distribution (Figure 58).

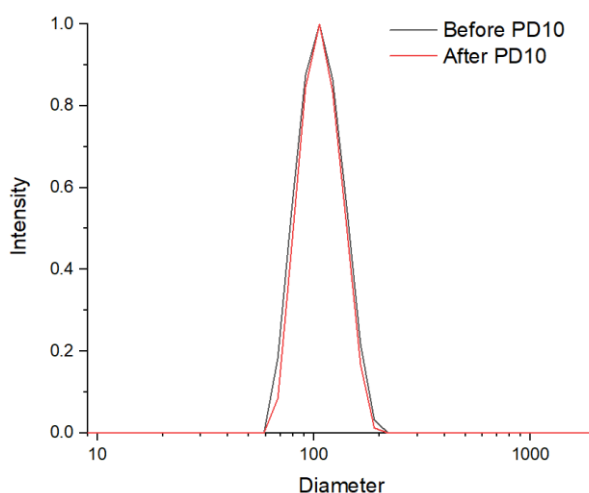


Figure 58: DLS chromatogram of FY26 loaded nanoparticles before (grey) and after (red) being filtered through a PD10 column

In order to calculate the final encapsulation efficiency, an aliquot of the nanoparticles was disassembled by addition of dilute HCl acid and the UV-vis absorption at 581 nm of the now transparent sample measured. This absorption value (0.62) was then converted to concentration using the molar extinction coefficient previously determined ($\epsilon = 19,400 \text{ M}^{-1}\text{cm}^{-1}$). This calculation gave a FY26 concentration value of $32 \text{ }\mu\text{M}$ corresponding to a high encapsulation efficiency of 76%. Whilst overall encapsulation efficiency was high, poor solubility of the drug in the starting DPAEMA monomer, limits the total amount of drug loading achievable. Furthermore, it was not possible to assess whether FY26 had remained intact by the high temperatures, basic environment and radical exposure throughout the polymerisation. For these two reasons, drug loading after polymerisation was next trialled as an alternative. For this, preformed DPAEMA nanoparticles were loaded with FY26. To achieve this loading, FY26 was first dissolved in a small amount of water miscible organic solvent before direct addition to the nanoparticle solution. Dioxane, THF, DMF and MeOH were tested as the water miscible organic solvent, with DMF and MeOH proving to be the best at solubilizing FY26. The purpose of the organic solvent is not only to solubilize FY26, but also to loosen the polymeric nanoparticles, allowing for increased drug permeation. Whilst

soluble in DMF, pDPAEMA proved only sparingly soluble in MeOH; DMF was therefore selected for the drug loading procedure. Once dissolved in DMF, the FY26 solution was added directly to the nanoparticle solution, followed by gentle shaking for 24 hrs. After drug loading, any free FY26 needs to be removed, as before, PD-10 desalting columns were used for this. However, unlike the fast and distinct elutions described earlier, the nanoparticles appeared to become trapped within the column. It was reasoned that the presence of DMF, although small, might be degrading the packing of the column leading to blockages. In addition to this problem, the lingering presence of any organic solvent is likely to prove hazardous *in vivo*. To avoid the use of organic solvents, encapsulation was attempted by direct addition of FY26 to the nanoparticle solution. Due to the poor solubility of FY26 in water, the solution was vortexed extensively to disperse the drug before being left to shake gently for 24 hrs. PD-10 desalting columns were then used successfully to purify away any excess FY26, confirming that the presence of organic solvents was detrimental to the columns. As before, the encapsulation efficiency was calculated by acidifying the solution and calculating the concentration of FY26 from the measured absorption at 581 nm. The encapsulation efficiency for nanoparticles loaded this way was disappointingly low (14 μ M, 39%); far lower than had been achieved earlier. In an attempt to increase the encapsulation efficiency, a longer period of 48 hrs shaking was used before purification. This encapsulation efficiency was then re-estimated and found to be significantly higher (23 μ M, 64%). An even longer shaking period of 72 hrs was also trialled and showed a small increase in encapsulation efficiency (26 μ M, 73%), comparable to what was achieved by drug loading before polymerisation. Whilst the encapsulation efficiency was high, the actual drug concentration was still fairly low, largely owing to a large increase in volume resulting from the PD10 de-salting columns. The elution volume can be decreased by optimizing the column conditions, however, with prepacked columns and

using only water as the eluent, there was a limit to what improvement could be gained. As the PD10 de-salting columns could not be significantly improved, an alternative method of separation, centrifugal dialysis, was investigated. In centrifugal dialysis, the nanoparticle solution is held within a low molecular weight cut-off membrane; allowing the diffusion of free drug but not nanoparticles. This membrane is then placed within a falcon tube and centrifuged at high rates. Water and free drug are pushed through the membrane by centrifugal force, leaving behind the nanoparticles in a decreased volume of solution. Fresh water can then be added to this solution followed by more centrifugation. In this way, free drug is washed away without increasing the nanoparticles solutions overall volume; increasing the final encapsulated drug concentration. DLS was used to confirm that the nanoparticles had not aggregated during centrifugation (Figure 59)

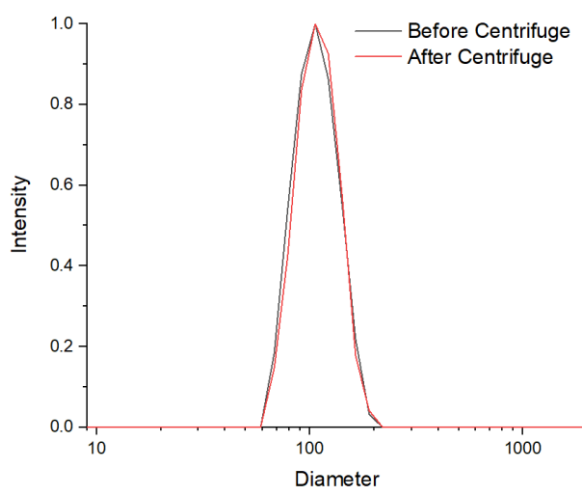


Figure 59: DLS chromatogram of FY26 loaded nanoparticles before (grey) and after (red) being centrifugal dialysis.

Once it had been confirmed that the nanoparticles were still dispersed, UV-vis was again used to determine overall FY26 concentration (149 μM) and encapsulation efficiency (68%). The slight decrease in encapsulation efficiency likely comes from a small amount of FY26 being extruded from the nanoparticles by centrifugal forces; however, it is more than compensated by the substantial increase in final concentration. Due to its higher final

concentration, centrifugal dialysis was chosen as the purification method for the final FY26 loaded nanoparticle preparation. Once the drug-loaded nanoparticles have been purified, the presence of pure water outside the particle leads to the gradual diffusion of FY26 out of the nanoparticles. To monitor this leakage, an experiment was set up whereby centrifugal dialysis was used to remove any leaked drug from a previously purified sample stored at 4 °C at different time points across a 3-week period. The concentration of leaked drug passing through the dialysis membrane was then calculated using UV-vis as described *supra vide*, and the concentration remaining was plotted against time (Figure 60).

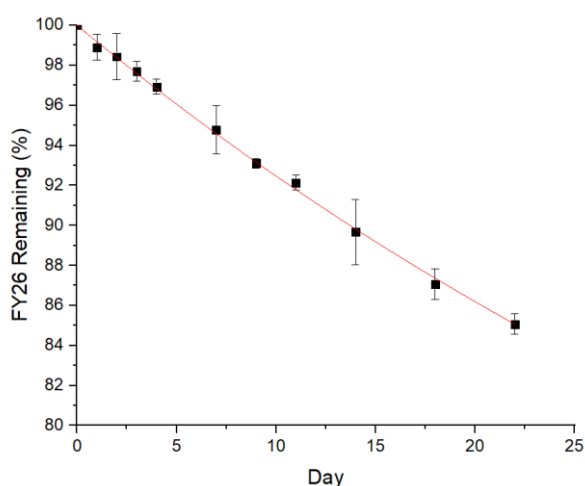


Figure 60: A plot of the percentage of FY26 remaining within previously purified nanoparticles against time, error bars are 95% confidence intervals and the red trend line is an exponential decay. Note the y-axis is scaled between 80 and 100% for clarity.

The results of this experiment show that previously purified samples will leak FY26 into solution, but slowly, in accordance with the poor water solubility of FY26. Greater than 95% of the starting FY26 remains within the nanoparticles after one week stored at 4 °C. Whilst minimal, this small amount of free FY26, may prove detrimental during the *in vivo* experiment; samples were therefore purified no longer than 3 days before injection (>98% FY26 remaining).

4.4.5 In vivo Results

4.4.5.1 Experimental design

In order to assess the effect encapsulation had on drug properties, an *in vivo* experiment was designed. The principal aims of this experiment are summarised below.

- To determine how encapsulation affects drug biodistribution and tumour uptake
- To review what effect, if any, encapsulating the drug has on its efficacy
- To investigate whether encapsulation can reduce the drugs overall toxicity

To complete these aims, tumours were first grown in a mouse model. Careful consideration was taken in the selection and preparation of these tumours in order to maximise the clinical relevance of the study. Firstly, a mouse liver cancer cell (Hepa1-6) was chosen for tumour growth; allowing for the use of immuno-competent mice; this decision was made based on literature from Couvreur et al. showing that macrophages were highly important in transporting nanoparticles to the liver and spleen and therefore consequential to the final biodistribution results¹⁶. To prepare realistic tumours Hepa1-6 cells were incubated in a nutrigel matrix for 72 hrs before being injected subcutaneously into the flanks of each mouse. The cells were left to grow *in situ* for a further 216 hrs (9 days), yielding tumours with an approximate starting size of 50 mm³. Once the tumour models had been prepared, the mice were then divided into two groups (n = 15) and injected with either; free FY26 or FY26 encapsulated within DPAEMA NPs. For both groups, the total concentration of drug injected was fixed at 5 mg per kg of animal mass (15.1 µM); chosen as previous studies in-house reported good survivability rates at this concentration. In both instances, the injections were made

intraperitoneally (IP); this method was chosen to match how chemotherapy agents are routinely administered clinically. IP injection also allows for higher injection volumes and has been shown to improve efficacy of chemotherapy agents¹⁷. After injection the mice were culled in smaller groups (n = 5) at time points of 6, 24 and 48 hrs. The tumours and liver were collected at each point to provide insight into the movement of FY26 within the body (section 4.4.5.2). Additionally, the body weights and tumour size of the final group were monitored at all time points (section 4.4.5.3 and 4.4.5.4). Finally, the survival data for both groups will be discussed with reference to the other measured results (section 4.4.5.5).

4.4.5.2 Organ distribution

FY26 content within the liver and tumours was assessed using Inductively Coupled Plasma Mass Spectrometry (ICP-MS). This technique allows quantitative determination of an elements concentration within a sample, in this instance osmium, within a working range of 1 – 1000 ppt. ICP-MS was chosen as the method of detection over other techniques such as UV-Vis spectroscopy and High Performance Liquid Chromatography largely due to its high compatibility with impurities and low detection limits down to 1 ppt¹⁸.

The measured concentrations of osmium within the liver and tumours at the three time points are shown below (Figure 61).

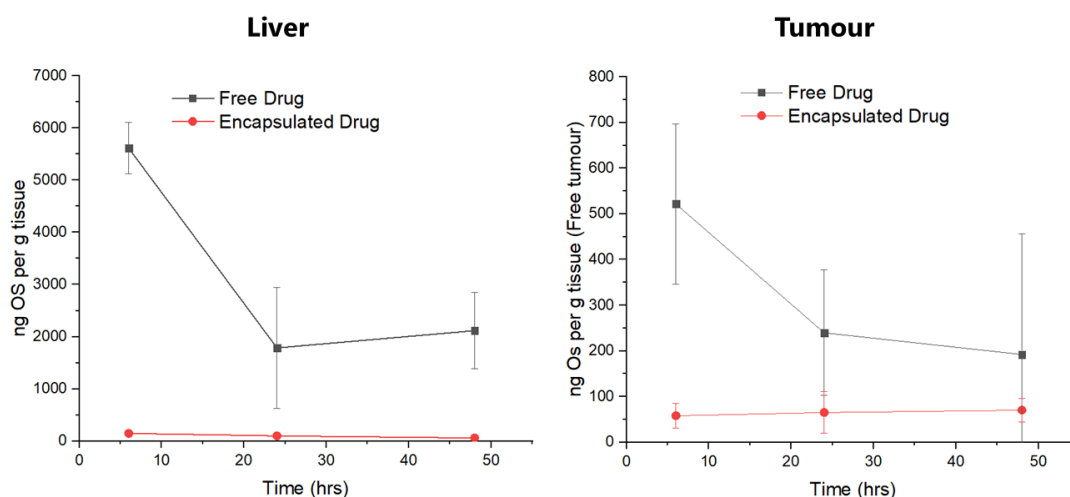


Figure 61: Concentrations of osmium as determined by ICP-MS within liver (left) and tumour (right) samples excised at three time points for mice injected with free FY26 (grey) and those injected with encapsulated FY26 (red); error bars are 95% confidence intervals.

Free FY26 (grey) showed both very rapid and large uptake into the liver (left) within the first 6 hours of the experiment; totalling almost 60% of the overall dose given. After the first 6 hours, the levels of free FY26 within the liver drop considerably before plateauing. This drop is consistent with clearance of FY26 from the body *via* the liver followed by excretion. However, the lack of change in osmium concentration between 24 and 48 hours cannot be explained as simply. As ICP-MS only follows the osmium concentrations not its state, one explanation is that FY26 is converted to several metabolites within the liver, which are then excreted at different rates. A second explanation is that small amounts of FY26 are continuing to be taken up by the liver whilst the bulk is being excreted; leading to a plateau. It should also be noted that unfortunately one mouse in the 48 hr free drug group had to be put down at 24 hrs due to poor health; leaving a group size of 4. The loss of this unhealthy animal from the group may also be speculated to have skewed the final results.

In comparison, encapsulated FY26 (red) showed very low uptake into the liver across all time points of the experiment. A zoomed in version of Figure 61 is provided below for just encapsulated FY26 uptake into the liver (Figure 62).

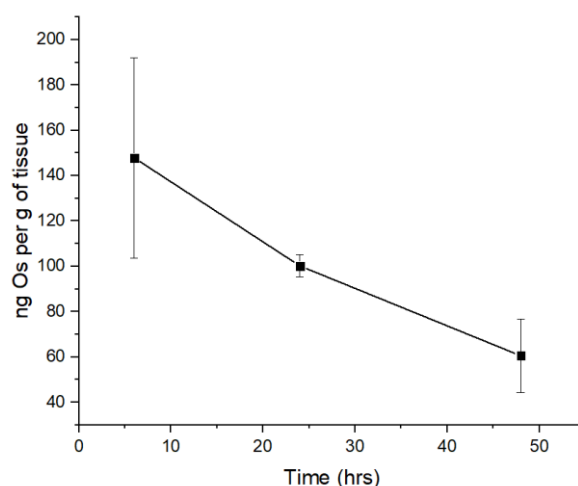


Figure 62: A close up of Figure 61 showing the concentrations of osmium as determined by ICP-MS within liver samples excised at three time points for mice injected with encapsulated FY26; error bars are 95% confidence intervals.

It is now visible, that whilst overall uptake is very low, it does show a downward trend with time. This decrease of osmium concentration within the liver over time is again consistent with it being excreted from the body. Unlike the free drug, there was no plateau observed for osmium levels in the liver between 24 and 48 hrs. The lack of a plateau for the encapsulated drug group weakens the hypothesis that the plateau in osmium concentration is for the free drug group is caused by FY26 being broken down into several osmium metabolites with different clearance times. To investigate the differing liver uptake pattern as well as the vastly different uptake amounts, it is necessary to explore the drug injection method further.

Intraperitoneal injections (IP) administer the drug directly into peritoneum cavity in the chest. This fluid and fat filled cavity serves to both support and protect the internal organs and is entirely contained within a serous membrane. Movement of materials across this membrane and into the wider body as a whole is tightly controlled; with the only direct exit being through the iliac and inguinal lymph nodes¹⁹. These lymph nodes act as a nexus for the body's immune system, where circulating dendritic cells present foreign materials to T-cells for recognition, followed by activation of b-cells and

antibody production. Due to the high concentration of immune system cells within lymph nodes, materials exiting the peritoneal cavity this way, rapidly interact and activate dendritic cells. These newly mature dendritic cells then exit the lymph node via the endothelial venules, into the circulating blood; before directly transporting the foreign material to the liver for processing. In this way, large quantities of the IP injected materials are directly transported to the liver. Importantly, however, it has been shown by Dinglasan, Mao and co-workers that this initial uptake into the lymph nodes is heavily size dependent²⁰. In their paper, the authors show that 100 nm PEG-PLGA nanoparticles have negligible to no uptake into the lymph nodes following IP injection. The similar composition of the nanoparticle outer surface, means that it is reasonable to assume that the 100 nm PEG-DPAEMA particles used in this study will behave in the same way. With exit via the lymph nodes effectively blocked for the NPs, they must exit the peritoneal cavity by alternative means. The membrane surrounding the peritoneal cavity is comprised of a single layer of flattened (squamous) epithelial cells, while movement of small molecules across this membrane is restricted, Baeza-Squiban et al. demonstrated that 50 and 200 nm silica nanoparticles could effectively cross a similar squamous membrane acellularly²¹. It therefore seems reasonable to assume that the 100 nm PEG-DPAEMA particles can, and are, exiting the peritoneal cavity this way. This route takes the NPs into the circulating blood directly, bypassing the lymph nodes, avoiding dendritic cell activation and direct transportation to the liver. Uptake into the liver from the blood without dendritic cell mediation is of course still possible, albeit at a reduced rate. This key difference in the two routes taken out of the peritoneal cavity explains why the free FY26 has significantly higher liver uptake than the encapsulated equivalent (summarised in Figure 63).

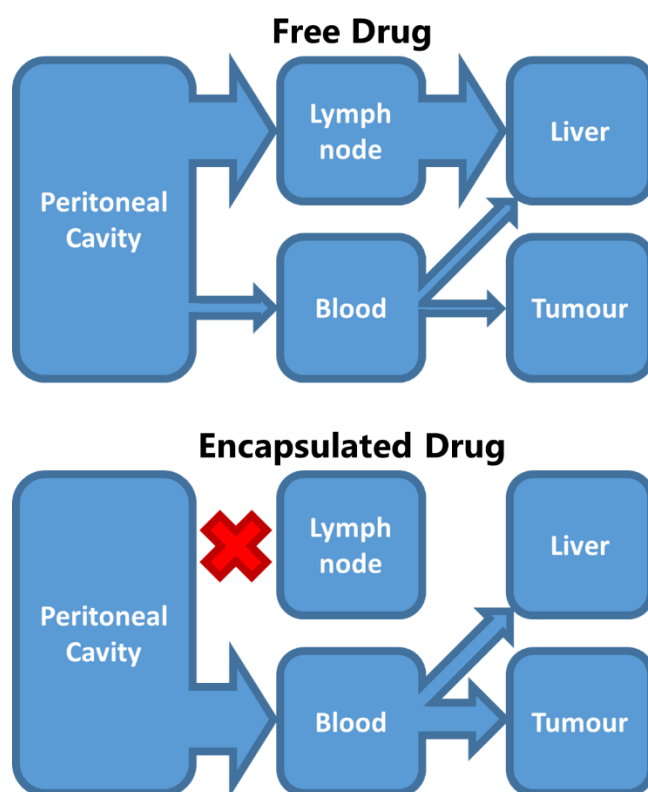


Figure 63: A graphical summary of the proposed differing routes taken by free FY26 (top) and encapsulated FY26 (bottom) from the peritoneal cavity to the liver and tumour sites. The width of the arrows are qualitative representations of the amount of material following that path.

As well as explaining the difference in overall liver uptake, the different routes taken can also be used to explain the pattern of liver uptake with time, particularly why the free drug showed a plateau not present for the encapsulated drug. As discussed *vide supra*, one hypothesis for the origin of this plateau was that small amounts of free drug was still arriving at the liver even as the bulk was cleared. Examination of Figure 63 shows that there are two separate routes a free drug could take to reach the liver; the major and faster route directly through the lymph nodes or the minor and slower pathway passing through the membrane and onwards into the blood. The different magnitudes and speeds of these pathways provide a possible mechanism for drug to be still arriving at the liver whilst the bulk is cleared. Furthermore, in the case of the encapsulated drug, there is only one major pathway from the peritoneal cavity to the liver and no plateau is observed (Figure 63). Whilst compelling, a more detailed pharmacokinetic experiment would be required

to confirm this theory as well as examination of the chemical nature of the osmium detected in the liver. A full biodistribution study is also ongoing to validate this theory further.

The concentrations of osmium within the two tumours was also measured and average per animal (Figure 61 – right). The free drug shows initial uptake into the tumour within 6 hours followed by a steady decrease. This decrease is due to the clearance of the drug from the tumour likely by tumour-associated macrophages²². Importantly, no plateau is observed in osmium levels between 24 and 48 hrs as was seen for uptake of the free drug into the liver. This lack of a plateau is consistent with the peritoneal escape model layout *vide supra* and in Figure 63 in which there is only one route between the peritoneal cavity and the tumour as opposed to two routes to the liver. By comparison, the uptake of osmium into the tumour for the encapsulated drug is completely different, a zoomed in version of Figure 61 is provided below to aid discussion.

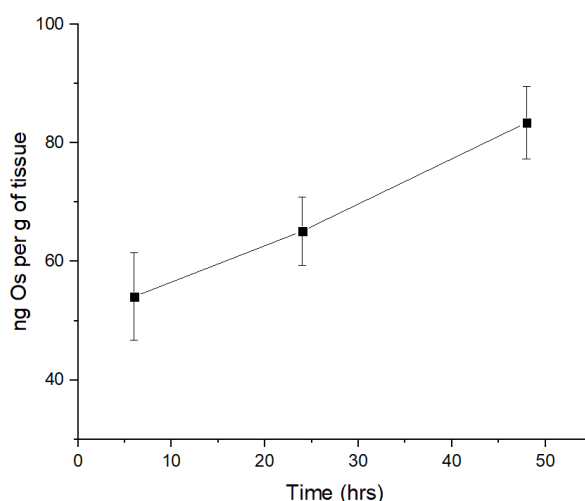


Figure 64: A close up of Figure 61 showing the concentrations of osmium as determined by ICP-MS within liver samples excised at three time points for mice injected with encapsulated FY26; error bars are 95% confidence intervals.

The first observation that should be noted from Figure 64 is that the osmium concentration within the tumour is increasing throughout the experiment. One explanation for this is that the acellular escape mechanism across the peritoneal membrane is significantly slower than for the free drug through the

lymph nodes. This decreased escape would lead to an increased residence time of the nanoparticles within the peritoneal cavity, delaying uptake into other tissues. This hypothesis is lent weight by Baeza-Squiban *et al.* who observed that only 35% and 14% of their 50 nm and 200 nm silica nanoparticles respectively crossed a model squamous cell membrane in 24 hrs²¹. This delayed escape of the nanoparticles can also be used to explain why, on the time scale of this experiment, the free drug shows higher total tumour uptake than the encapsulated drug. In order to understand this system more fully, a longer *in vivo* experiment would have to be conducted. Whilst lower than the free drug, the uptake of the encapsulated drug into the tumour is higher than into the liver; to better show this, a plot of uptake into tumour divided by uptake into the liver is provided below (Figure 65).

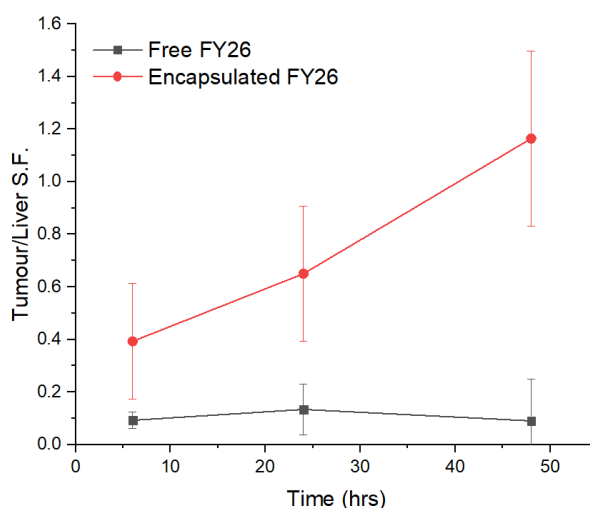


Figure 65: Ratios of the concentrations of osmium as determined by ICP-MS within the tumour and liver samples excised at three time points for mice injected with free FY26 (grey) and those injected with encapsulated FY26 (red); error bars are propagated from 95% confidence intervals.

It is desirable that the selectivity factor (SF) for uptake of the drug into the tumour versus the liver, be as high as possible. A low SF value indicates that not only is a large amount of the drug being effectively wasted by not reaching the tumour site, but also that healthy tissue is being exposed to it. As can be seen in Figure 65, the free drug has a very low SF value (<0.1), correspondent

with high liver over tumour uptake. This negative result can be rationalised by recalling that the principal exit for the free drug is via the lymph nodes followed by dendritic cell mediated directing straight to the liver (Figure 63). This direct pathway to the liver, coupled with a lack of routes to the tumour, results in a strong liver uptake preference. By comparison, the encapsulated drug SF value is relatively high, reaching values greater than 1, indicating a bias towards tumour uptake. This positive result is largely caused by the vastly reduced liver uptake described and discussed above; however, this cannot explain everything. As shown in Figure 63, the encapsulated drug escapes the peritoneal cavity via acellular translocation across the serous membrane, directly into the blood. Whilst this avoids dendritic cell activation and direct transport to the liver, it does not explain why the nanoparticles, when freely moving within the circulatory system, exhibit a bias towards tumour uptake. To answer this, the structural nature of tumours needs to be considered.

Tumour growth is facilitated and accompanied by an increase in local vascular endothelial growth factor (VEGF) concentration²³. This increase allows the tumour to develop a larger number of blood vessels (hypervascularity) than the healthy tissue equivalent, in order to sustain its increased metabolic demands. It has been repeatedly shown that, not only do tumours contain a larger number of blood vessels, but also that their architecture and structure are significantly different to the norm. Importantly for this discussion, the blood vessels have been shown to feature large pores, between 100 – 780 nm in diameter, increasing their permeability to larger structures such as nanoparticles^{24, 25}. By comparison, the lining of healthy blood vessels lack these larger pores and are impermeable to nanoparticles. This difference in permeability leads to the so-called enhanced permeation and retention (EPR) effect, wherein nanoparticles are theorized to accumulate selectively within tumours^{26, 27}. Whilst nearing fifty years old, the theory is still proving controversial and has a number of distinct caveats, being dependent on both

the specific tumour type and the nanoparticles morphology, and is best discussed on a case-by-case basis²⁸. In our instance, EPR theory would support and explain the increased selectivity for uptake of encapsulated drug from the blood into the tumour versus the liver. However, it should be noted that main increase in selectivity is as a result of the encapsulated drug having avoided initial passage through the lymph nodes. As discussed *vide supra*, this avoidance of the lymph nodes is heavily dependent upon nanoparticle size; this is, therefore, a key consideration for any future work.

4.4.5.3 Body weight

Changes to overall body weight are often used as a general indicator of mouse health, with sudden decreases interpreted negatively. Dose dependent weight loss in mice injected (IP) with a known toxic agent has been shown²⁹, and it is therefore a useful metric to assess. The change in body weight of the mice injected with free FY26 and encapsulated FY26 was measured at 24 and 48hrs and the results plotted below (Figure 66).

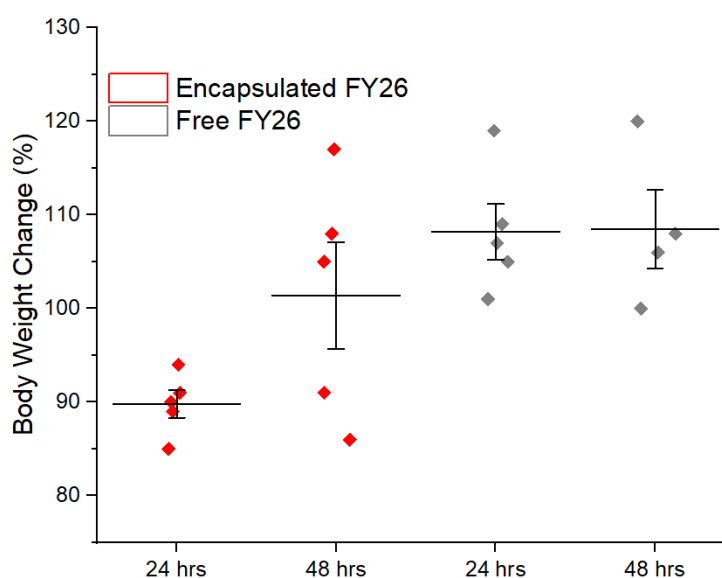


Figure 66: A scatter plot showing the percentage body weight change as measure from day 0 for mice injected with either encapsulated FY26 (red) or free FY26 (grey) at 24 and 48 hrs. Black horizontal lines indicate the mean of each data set whilst black vertical lines indicate the spread (± 1 standard deviation).

Mice injected with encapsulated FY26 showed consistent weight loss averaging -10% after 24 hrs. Partial to full recovery was observed after 48 hrs although the spread of weights became markedly broader. By comparison, mice injected with free FY26, suffered no weight loss and remained consistently around 108% starting mass. As briefly mentioned in section 4.4.5.2, there was one mouse fatality between 24 and 48 hrs, however, contrary to what may be expected, the fatality occurred in a mouse that had been injected with free FY26. The death of a mouse with a healthy body weight, suggests this may not be the best metric for toxicity, especially given that no mouse fatalities occurred within the encapsulated drug group despite considerable weight loss. Though there were no fatalities, it is still important to understand the origin of the sudden weight loss observed for mice injected with encapsulated FY26. One explanation for this weight loss is physiological stress caused by the large volume of injection. Despite thorough optimisation of drug loading described in section 4.4.4, a large injection volume of 1 mL was still required in order to provide sufficient FY26 content. The large quantity of water moves via osmosis from the peritoneal cavity into surrounding tissues before absorption into small and large intestine. Excess water within the ileum and jejunum specifically, has been shown to impair the body's ability to absorb sugars and other nutrients from food³⁰, leading to sudden weight loss. This hypothesis as to the origin of weight loss is supported further, by the partial recovery in body mass between 24 and 48 hrs corresponding with the excretion of excess water. It was also observed that mice injected with encapsulated FY26, produced an excess quantity of watery stool; lending more weight to this theory. These unpleasant side effects could be mitigated in a clinical setting by use of multiple smaller injections spread over time.

4.4.5.4 Tumour size

Tumour size was monitored throughout the experiment in order to assess what effect encapsulation had on the efficacy of the drug. Tumour size was

calculated via external measurements of the tumour diameter and converted to volume assuming spherical geometry. A more accurate alternative is to excise and weigh the tumour; however, this method requires the use of different animals for each time point. External measurement, by comparison, can be performed on the same set of live mice; providing more comparable results between points. The calculated tumour volumes of mice injected with both free and encapsulated FY26 are provided below (Figure 67) along with a negative control (PBS) for comparison.

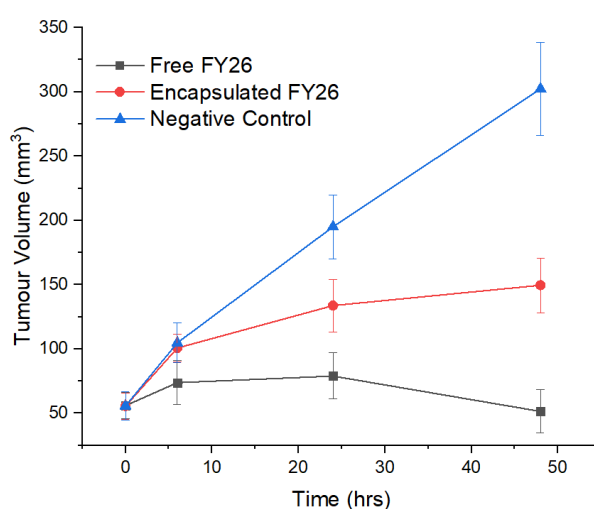


Figure 67: A plot of average tumour volume (N=5, n=2) versus time for mice injected (IP) with either free FY26 (grey), encapsulated FY26 (red) or a PBS control (blue); error bars are a 95% confidence interval.

In all cases, the starting tumour volume was approximately 50 mm³, in untreated mice (blue), this rapidly increased up to a final volume of 300 mm³ within 48 hrs. This rapid growth is consistent with the aggressive nature of the Hepa1-6 cells used to create the tumours³¹. In stark contrast to this, the tumour volume for mice treated with free FY26, shows very little increase for 24 hrs before actually decreasing below the starting size. A retardation of tumour growth can also be seen mice injected with encapsulated FY26, although to a less extent than the free drug. This reduction in anti-tumour activity proliferation is concurrent with there being decreased overall uptake of FY26 into the tumours of mice injected with the encapsulated drug (Figure 61). It is

also noticeable, that tumour growth appears identical for mice injected with the encapsulated drug and those in the negative control group during the first 6 hrs. This result again matches with tumour uptake data (Figure 64), which shows that the concentration of FY26 within the tumour was negligible within the first 6 hours; explained by the increased residency time of nanoparticles within the peritoneal cavity. By combining the tumour uptake data and the tumour volume sizes, it is possible to calculate the activity of the free and encapsulated drug (Equation 1).

$$Activity = \frac{V_c - V_{IP}}{[FY26]_{tumour}} \quad (1)$$

Where V_c and V_{IP} are the tumour volumes for mice in the negative control group and treated group respectively and $[FY26]_{tumour}$ is the concentration of $[FY26]$ within the tumour. A plot of activity versus time for both the free and encapsulated drug is provided below (Figure 68).

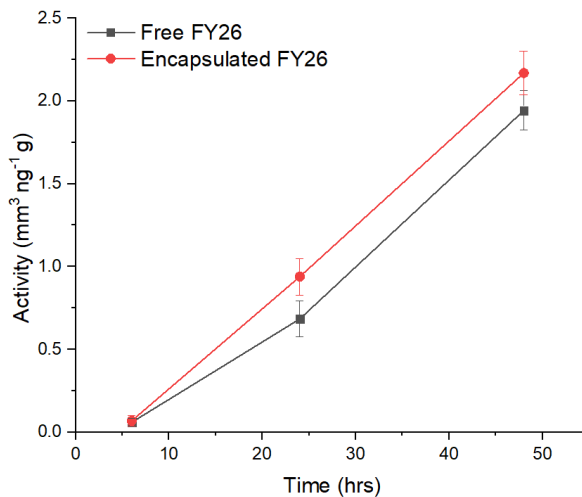


Figure 68: A plot of anti-tumour activity of free (grey) and encapsulated (red) FY26 at different time points as calculated from equation 1. Error bars are propagated 95% confidence intervals.

Figure 68 shows that the activity of FY26 increases with time consistent with earlier studies. Importantly the data shows that there is a statistically insignificant difference in activity between free and encapsulated FY26. This result indicates that encapsulation of FY26 does not retard its anti-tumour

properties. The DPAEMA nanoparticles used for encapsulation can therefore be assumed effective at releasing FY26 within cells, consistent with their pH responsive design.

4.4.5.5 Survival Data

The fraction of mice surviving was monitored throughout the experiment and is recorded in Figure 69

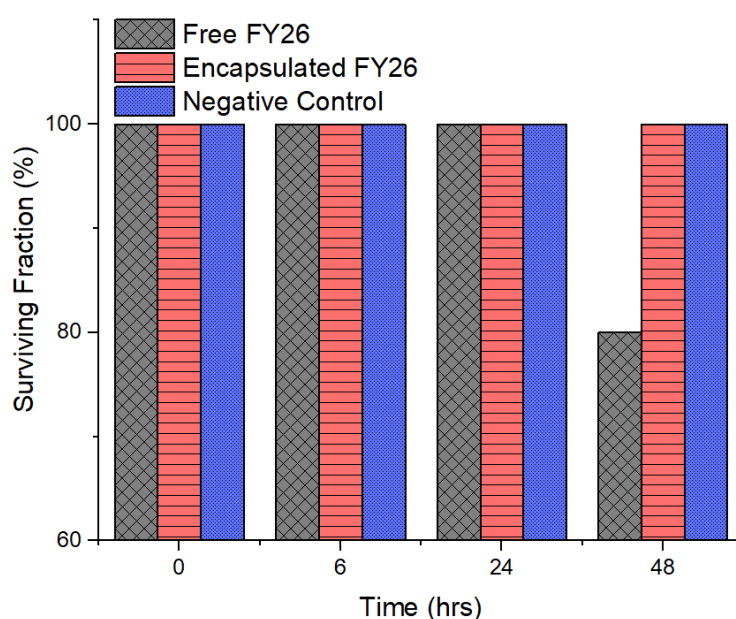


Figure 69: A bar graph showing the surviving fraction of mice injected with free (grey) and encapsulated (red) FY26, as well as an untreated control group at different times; starting group size $N = 5$.

All mice injected with encapsulated FY26 survived for the 48 hrs of the experiment; however, one of the five mice injected with free FY26, did die. This death cannot be attributed to the presence of the tumours as all mice in the untreated control group also survived. Instead, lethality would appear a potential side effect of the drug itself. The origin of this side effect is likely to be the large and non-selective uptake of FY26 into the healthy tissue such as the liver (Figure 61). No deaths were observed in mice injected with the encapsulated drug, despite the same concentration of FY26 being administered, correspondent with its more selective tumour delivery. The death of a mouse from injection of free FY26, highlights the high toxicity of

anticancer drugs and the need to improve their selectivity; with nanoparticle encapsulation proving a promising alternative.

4.4.5.6 Future Work and Perspective

Whilst the *in vivo* experiment described *vide supra* has provided a large amount of valuable information, there are a number of potential problems that need addressing by future experiments. Firstly, whilst drug leakage from the nanoparticles was shown to be minimal under laboratory conditions (Section 4.4.4), there is no guarantee that this is the same post-injection. Secondly, nothing is presently proven about the clearance of the polymers from the body after drug delivery. Literature sources would suggest that the lower molecular weight nature of the polymers, coupled with their hydrophilicity and cationic nature, would lead to rapid clearance via the kidneys³²⁻³⁴. To monitor this, the polymer would have to be labelled; either fluorescently or with a non-native element such as bromine for quantitative detection by ICP-MS. Independent monitoring of both the polymer and the drug concentration within tissue would also allow for any drug leakage to be detected. Finally, owing to the lengthy residence time within the peritoneal cavity, the time scale of future *in vivo* experiments should be extended beyond 48 hrs. This would allow enough time to assess the total amount of FY26 reaching the tumour, a metric which was still increasing throughout the experiment.

The *in vivo* experiment has shown that encapsulation of anti-cancer drugs can increase their selectivity towards tumours and reduce their overall toxicity/lethality. However, these advantages come at the detriment of delivery speed as well as overall delivery quantity. In the future, there are two parameters recommend for further investigation. The first is the nanoparticles size; a large diameter is pivotal to preventing escape from the peritoneal cavity into the lymph nodes and direct transport to the liver. However, a diameter that is too large would be expected to decrease acellular escape; worsening

the time delay in reaching the tumour already seen. It would therefore be recommended investigating particles ranging in diameter from 50 to 150 nm in order to find the optimal size. The second parameter that should be investigated is the nanoparticles surface coating. In this experiment, nanoparticles with an inert PEG coating displayed a modest sized-based bias towards tumour over liver uptake from the circulating blood. To improve this selectivity further, targeting moieties (sugars, biotin, RGD peptides etc.) displayed on the surface of nanoparticles³⁵, should be investigated.

4.5 Conclusion

In this chapter, pH responsive particles were investigated as potential anti-cancer drug delivery vectors. The final chosen particles, PEG₄₅-*b*-pDPAEMA₉₀ (diameter = 101 nm) were first shown to be non-toxic *in vitro* at therapeutically relevant concentrations. The loading and purification of an experimental anti-cancer drug into these particles was then attempted and optimised to allow for high encapsulation efficiency and overall drug concentration. The *in vivo* properties of these encapsulated drug nanoparticles was then directly compared with the free drug at the same concentration. The uptake of the drug into liver and tumours was monitored and thoroughly discussed with reference to the differing escape pathways from the peritoneal cavity. It was shown that encapsulation of the drug improved its tumour selectivity by an order of magnitude. Other metrics for mouse health, including body weight and overall survival were also measured and discussed. The anti-tumour efficacy of the encapsulated and free drugs was assessed and their overall activities compared. In all, encapsulation of the anti-cancer drug was shown to dramatically improve its tumour selectivity, decrease its toxicity/lethality and demonstrated no decrease in activity relative to the free drug.

4.6 References

1. F. Alexis, E. Pridgen, L. K. Molnar and O. C. Farokhzad, *Molecular Pharmaceutics*, 2008, **5**, 505-515.
2. A. Schädlich, C. Rose, J. Kuntsche, H. Caysa, T. Mueller, A. Göpferich and K. Mäder, *Pharmaceutical research*, 2011, **28**, 1995-2007.
3. W. B. Liechty and N. A. Peppas, *European Journal of Pharmaceutics and Biopharmaceutics*, 2012, **80**, 241-246.
4. N. Deirram, C. Zhang, S. S. Kermaniyan, A. P. R. Johnston and G. K. Such, *Macromolecular Rapid Communications*, 2019, **40**, 1800917.
5. G. H. Ball, *American Journal of Physiology-Legacy Content*, 1939, **128**, 175-178.
6. Y.-H. Lin, C.-H. Chang, Y.-S. Wu, Y.-M. Hsu, S.-F. Chiou and Y.-J. Chen, *Biomaterials*, 2009, **30**, 3332-3342.
7. G. Liu and P. Liu, *Colloids and Surfaces A: Physicochemical and Engineering Aspects*, 2010, **354**, 377-381.
8. Y. Hu, T. Litwin, A. R. Nagaraja, B. Kwong, J. Katz, N. Watson and D. J. Irvine, *Nano Letters*, 2007, **7**, 3056-3064.
9. P. Wei, G. Gangapurwala, D. Pretzel, M. N. Leiske, L. Wang, S. Hoepfner, S. Schubert, J. C. Brendel and U. S. Schubert, *Biomacromolecules*, 2019, **20**, 130-140.
10. S. Gatti, A. Agostini, U. C. Palmiero, C. Colombo, M. Peviani, A. Biffi and D. Moscatelli, *Nanotechnology*, 2018, **29**, 305602.
11. W. Gao, J. M. Chan and O. C. Farokhzad, *Molecular Pharmaceutics*, 2010, **7**, 1913-1920.
12. S. L. Canning, T. J. Neal and S. P. Armes, *Macromolecules*, 2017, **50**, 6108-6116.
13. J. Chen, J. A. Hessler, K. Putschakayala, B. K. Panama, D. P. Khan, S. Hong, D. G. Mullen, S. C. DiMaggio, A. Som, G. N. Tew, A. N. Lopatin, J. R. Baker, M. M. B. Holl and B. G. Orr, *The Journal of Physical Chemistry B*, 2009, **113**, 11179-11185.
14. J. M. Hearn, I. Romero-Canelón, A. F. Munro, Y. Fu, A. M. Pizarro, M. J. Garnett, U. McDermott, N. O. Carragher and P. J. Sadler, *Proc Natl Acad Sci U S A*, 2015, **112**, E3800-3805.
15. S. D. Shnyder, Y. Fu, A. Habtemariam, S. H. van Rijt, P. A. Cooper, P. M. Loadman and P. J. Sadler, *MedChemComm*, 2011, **2**, 666-668.
16. R. Fernández-Urrusuno, E. Fattal, J. M. Rodrigues Jr., J. Féger, P. Bedossa and P. Couvreur, *Journal of Biomedical Materials Research*, 1996, **31**, 401-408.
17. Y. Miyagi, K. Fujiwara, J. Kigawa, H. Itamochi, S. Nagao, E. Aotani, N. Terakawa and I. Kohno, *Gynecologic Oncology*, 2005, **99**, 591-596.

18. E. D. Prudnikov and R. M. Barnes, *Fresenius' Journal of Analytical Chemistry*, 1998, **362**, 465-468.
19. T. Olin and T. Saldeen, *Cancer Res*, 1964, **24**, 1700-1711.
20. G. P. Howard, G. Verma, X. Ke, W. M. Thayer, T. Hamerly, V. K. Baxter, J. E. Lee, R. R. Dinglasan and H.-Q. Mao, *Nano Research*, 2019, **12**, 837-844.
21. I. George, S. Vranic, S. Boland, A. Courtois and A. Baeza-Squiban, *Toxicology in Vitro*, 2015, **29**, 51-58.
22. M. P. Kai, H. E. Brighton, C. A. Fromen, T. W. Shen, J. C. Luft, Y. E. Luft, A. W. Keeler, G. R. Robbins, J. P. Y. Ting, W. C. Zamboni, J. E. Bear and J. M. DeSimone, *ACS Nano*, 2016, **10**, 861-870.
23. T. Minko, P. Kopečková, V. Pozharov, K. D. Jensen and J. Kopeček, *Pharmaceutical Research*, 2000, **17**, 505-514.
24. J. Wang, Z. Lu, Y. Gao, M. G. Wientjes and J. L. Au, *Nanomedicine (Lond)*, 2011, **6**, 1605-1620.
25. H. F. Dvorak, J. A. Nagy and A. M. Dvorak, *Cancer Cells*, 1991, **3**, 77-85.
26. K. J. Harrington, S. Mohammadtaghi, P. S. Uster, D. Glass, A. M. Peters, R. G. Vile and J. S. W. Stewart, *Clinical Cancer Research*, 2001, **7**, 243-254.
27. D. W. Northfelt, B. J. Dezube, J. A. Thommes, B. J. Miller, M. A. Fischl, A. Friedman-Kien, L. D. Kaplan, C. D. Mond, R. D. Mamelok and D. H. Henry, *Journal of Clinical Oncology*, 1998, **16**, 2445-2451.
28. J. W. Nichols and Y. H. Bae, *Journal of Controlled Release*, 2014, **190**, 451-464.
29. Q. Zhang, S. X. Zeng and H. Lu, *Toxicology Reports*, 2015, **2**, 546-554.
30. K. M. Seiler, E. L. Schenhals, R. J. von Furstenberg, B. K. Allena, B. J. Smith, D. Scaria, M. N. Bresler, C. M. Dekaney and S. J. Henning, *Cell Tissue Res*, 2015, **361**, 427-438.
31. T. Kimura, Y. Kato, Y. Ozawa, K. Kodama, J. Ito, K. Ichikawa, K. Yamada, Y. Hori, K. Tabata, K. Takase, J. Matsui, Y. Funahashi and K. Nomoto, *Cancer Science*, 2018, **109**, 3993-4002.
32. H. K. de Wolf, C. J. Snel, F. J. Verbaan, R. M. Schiffelers, W. E. Hennink and G. Storm, *International Journal of Pharmaceutics*, 2007, **331**, 167-175.
33. S. Lee, W. Lim, J. S. Jung, D. Jo, G. Jo, M. H. Park and H. Hyun, *Macromolecular Research*, 2018, **26**, 1251-1256.
34. J. E. Zuckerman, C. H. J. Choi, H. Han and M. E. Davis, *Proc Natl Acad Sci U S A*, 2012, **109**, 3137-3142.
35. L. Brannon-Peppas and J. O. Blanchette, *Advanced Drug Delivery Reviews*, 2004, **56**, 1649-1659.

5 Conclusion and Outlook

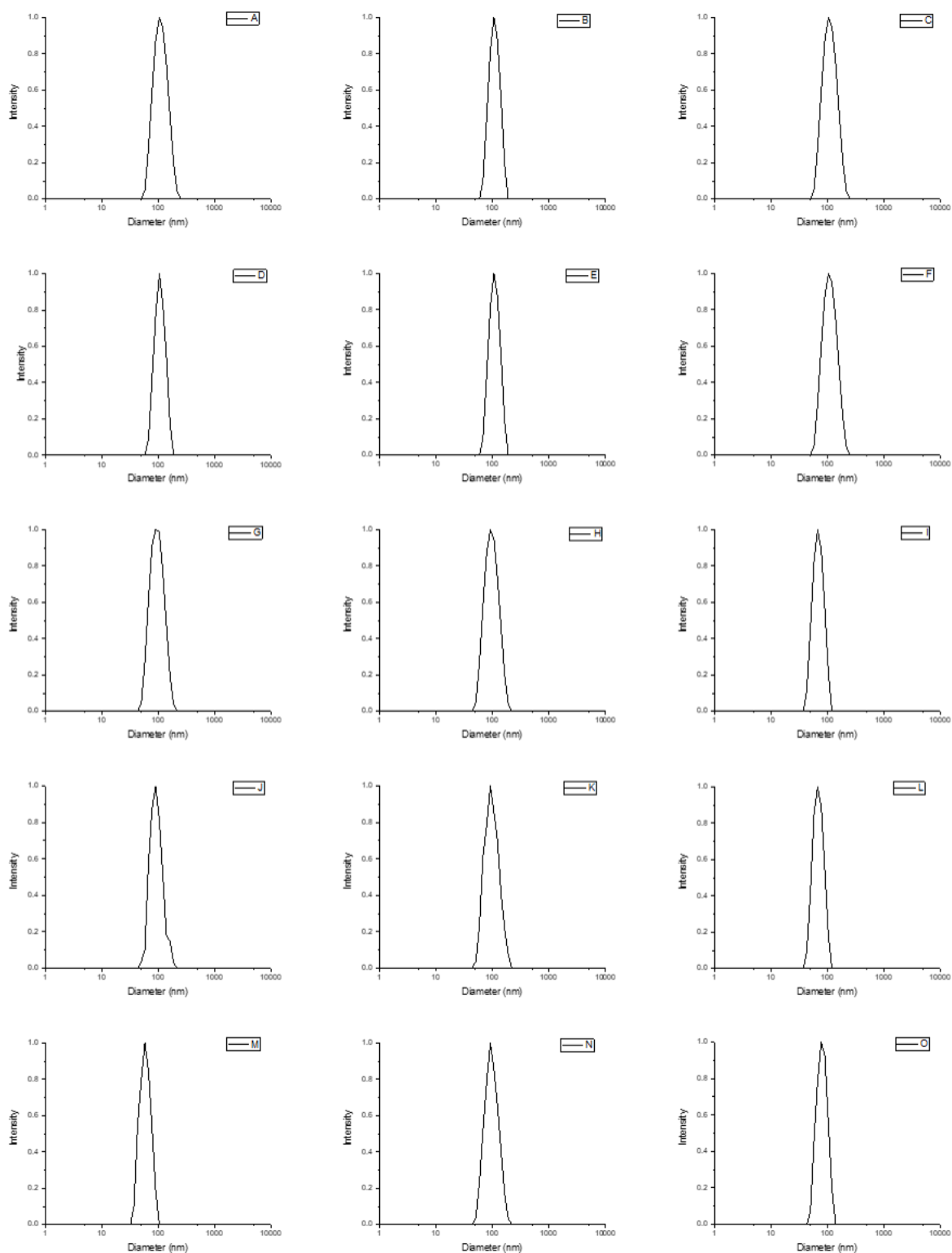
The aim of this work was to rationally design and synthesise polymeric nanoparticles for use as drug delivery vectors. Emulsion polymerisation was combined with Reversible Addition Fragmentation chain-Transfer (RAFT) control to produce uniform polymeric nanoparticles. The use of RAFT polymerisation allowed for the molecular weights of the composite polymers to be well controlled, a feature strongly enhanced by performing the polymerisation under emulsion conditions. Additionally RAFT emulsion allowed for the surface of the nanoparticles to be predefined, in this instance to bare a covering a polyethylene glycol (PEG) and have a neutral surface charge. The absence of a negative surface charge allowed for rapid and efficient cell internalisation reaching near 50% uptake within just 30 minutes and quantitative uptake within 3 hours. As well as the surface, the core of the nanoparticles could be designed to trigger disassembly under acidic conditions. This pH responsive behaviour was assessed for a library of fifteen nanoparticles based around DPAEMA and DEAEMA and shown to be tailorable over a range of pH values from 7.3 – 4.7. The rate of disassembly was also shown to be extremely rapid, occurring within 0.5 seconds; in stark contrast to literature systems that depend on slower hydrolysis mechanisms. The rapid rate of disassembly combined with a responsive pH value similar to that of a cell lysosome (pH ~4.5) means that pDPAEMA₉₀ nanoparticles are ideal for intracellular drug delivery. Additionally the knowledge of which design parameters affect the pH of disassembly will prove valuable to future projects aimed at targeting different acidic regions of the body such as sites of inflammation and infection. It was also demonstrated that pDPAEMA₉₀ nanoparticles were non-toxic *in vitro* against Murine fibroblast cells (3T3) cells.

A number of different strategies for the loading of an anti-cancer drug into the polymeric nanoparticle and subsequent purification were investigated and

reviewed in terms of encapsulation efficiency, overall final concentration and general practicality. Many readers may find this information insightful when planning their own drug loading experiments. *In vivo*, it was shown that encapsulation within pDPAEMA₉₀ nanoparticles significantly improved the selectivity of uptake of the drug into tumours versus healthy tissue. Unlike other non or slowly responsive nanoparticles in the literature, there was no reduction in drug activity caused by encapsulation, demonstrating efficient drug release intracellularly; concurrent with the disassembly of the nanoparticles. This result demonstrates that future drug-delivery vehicles should be based around rapidly responding nanoparticles. Despite significant improvements in selectivity, encapsulation within a nanoparticle did reduce overall drug uptake within the 48 hours monitored. This reduction was attributed as being a consequence of the slow movement of nanoparticles across the peritoneal membrane and into circulating blood. To improve on this, nanoparticles of slightly reduced size (80 – 90 nm) should be investigated along with those bearing an overall positive surface size.

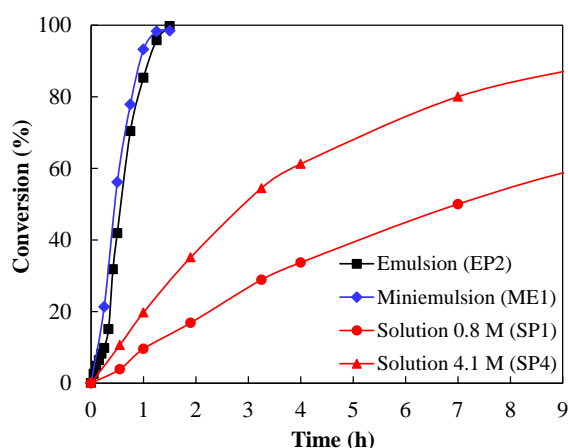
Overall, this thesis has demonstrated that RAFT emulsion can be used to produce both uniform polymers and nanoparticles. This method was utilised in the production of pH responsive nanoparticles to understand better the design parameters affecting their disassembly. These pH responsive nanoparticles were then investigated as potential drug delivery vectors; displaying impressive enhancements of selectivity *in vivo*.

6 Appendix



DLS Spectra of the nanoparticles produced in this thesis and not otherwise provided *supra vide*. A PEG₄₅-*co*-pDPAEMA₁₀₀, B PEG₄₅-*co*-(pDPAEMA₇₅-*stat*-

pDEAEMA₂₅), C PEG₄₅-*co*-(pDPAEMA₅₀-*stat*-pDEAEMA₅₀), D PEG₄₅-*co*-(pDPAEMA₂₅-*stat*-pDEAEMA₇₅), E PEG₄₅-*co*-pDEAEMA₁₀₀, F PEG₄₅-*co*-(pDPAEMA₇₅-*stat*-pBMA₂₅), G PEG₄₅-*co*-(pDPAEMA₅₀-*stat*-pBMA₅₀), H PEG₄₅-*co*-(pDPAEMA₂₅-*stat*-pBMA₇₅), I PEG₄₅-*co*-pBMA₁₀₀, J PEG₄₅-*co*-(pDPAEMA₇₅-*stat*-pMMA₂₅), K PEG₄₅-*co*-(pDPAEMA₅₀-*stat*-pMMA₅₀), L PEG₄₅-*co*-(pDPAEMA₂₅-*stat*-pMMA₇₅), M PEG₄₅-*co*-pMMA₁₀₀, N PEG₄₅-*co*-pDPAEMA₅₀, O PEG₄₅-*co*-(pDPAEMA₂₅-*stat*-pBMA₂₅).



Kinetic plots of monomer conversion for emulsion, solution and miniemulsion polymerisations of BMA (DP100) using PEG-CTA. Note that whilst very similar rates were observed for emulsion and miniemulsion conditions, only emulsion polymerisation yielded low dispersity polymers ($\bar{M}_w/\bar{M}_n = 1.13$ for emulsion vs 1.84 for miniemulsion). The significant improvement in polymer control observed under emulsion versus solution and miniemulsion conditions, therefore, cannot be attributed to the rate acceleration provided by compartmentalisation and is instead solely due to the inbuilt monomer feeding mechanism discussed in chapter 2. Full kinetic information for the emulsion experiment is tabulated overleaf.

Time (min)	Conversion (%)	Particle size (nm)	Pdi	Mn (g/mol)	\bar{D}
0	0	21 *	0.341*	2453	1.09
3	2.6	21 *	0.341*	3527	1.11
6	4.8	21 *	0.341*	4683	1.10
9	6.4	21 *	0.341*	5079	1.11
12	8.2	21 *	0.341*	6403	1.15
15	9.8	21 *	0.341*	6982	1.19
20	15.1	22.1	0.330	7998	1.24
25	31.8	29.7	0.318	10632	1.39
30	41.9	42.6	0.275	11448	1.50
45	70.4	61.5	0.142	12791	1.34
60	85.3	73.6	0.133	15646	1.22
75	95.8	78.2	0.126	17819	1.15
90	99.7	79.8	0.087	19044	1.13

*This is the size of the starting micelles measured separately as DLS of the kinetic sample was below the CMC but above the CMC in the actual reaction.